

NL 470916

NASA TN D-332

1N-02
331726



TECHNICAL NOTE

D-332

AXIAL-FORCE REDUCTION BY INTERFERENCE BETWEEN
JET AND NEIGHBORING AFTERBODY

By William C. Pitts and Lyle E. Wiggins

Ames Research Center
Moffett Field, Calif.

NATIONAL AERONAUTICS AND SPACE ADMINISTRATION
WASHINGTON

September 1960

NASA TN D-332

NATIONAL AERONAUTICS AND SPACE ADMINISTRATION

TECHNICAL NOTE D-332

AXIAL-FORCE REDUCTION BY INTERFERENCE BETWEEN

JET AND NEIGHBORING AFTERBODY

By William C. Pitts and Lyle E. Wiggins

SUMMARY

Experimental results are presented for an exploratory investigation of the effectiveness of interference between jet and afterbody in reducing the axial force on an afterbody with a neighboring jet. In addition to the interference axial force, measurements are presented of the interference normal force and the center of pressure of the interference normal force. The free-stream Mach number was 2.94, the jet-exit Mach number was 2.71, and the Reynolds number was 0.25×10^6 , based on body diameter. The variables investigated include static-pressure ratio of the jet (up to 9), nacelle position relative to afterbody, angle of attack (-5° to 10°), and afterbody shape. Two families of afterbody shapes were tested. One family consisted of tangent-ogive bodies of revolution with varying length and base areas. The other family was formed by taking a planar slice off a circular cylinder with varying angle between the plane and cylinder. The trends with these variables are shown for conditions near maximum jet-afterbody interference. The interference axial forces are large and favorable. For several configurations the total afterbody axial force is reduced to zero by the interference.

INTRODUCTION

It has been shown in references 1 and 2 that large positive pressures can act on surfaces located in the flow field surrounding a jet. With proper design these interference pressures can be utilized to reduce the afterbody drag of a missile or airplane configuration that has the nacelle neighboring the afterbody. To reduce the drag as much as possible (within limits prescribed by other design factors), it is necessary to know the effect of important variables such as jet-exit pressure ratio, nacelle position relative to the afterbody, afterbody shape, and angle of attack. At present little information of this nature is available for the jet-afterbody interference problem. It is the purpose of this report to present some exploratory results that show trends in the axial-force variation with the above variables near the conditions for maximum jet-afterbody interference. The symbols used in this report are defined in appendix A.

APPARATUS

Wind Tunnel

This investigation was conducted in the Ames 1- by 3-Foot Supersonic Wind Tunnels No. 1 and No. 2. Tunnel No. 1 is a continuous-operation, variable-pressure wind tunnel with a flexible-plate nozzle which provides a Mach number range from 1.4 to 4.0. Tunnel No. 2 is an intermittent-type wind tunnel with a Mach number range from 1.4 to 3.8.

Models

The geometry of the models used in this investigation is shown in figure 1. The body consisted of a cone-cylinder combination with interchangeable afterbodies. Afterbodies A through E were formed by taking planar slices off circular cylinders. Afterbodies F through I were tangent-ogive bodies of revolution. The nacelle was a cone-cylinder combination with a slightly flared afterbody (1.2° half angle). A cross-sectional view of the nacelle is shown in figure 2. The exit to throat area ratio was 3.37 which corresponds to a theoretical exit Mach number of 2.76. The divergent portion of the nozzle was conical and made an 11.2° angle with the axis.

A
2
4
9

Model Supports

The body and the nacelle were supported separately by struts that projected from the side of the tunnel as shown in figures 3 and 4. The body support strut was shielded from the flow by a hollow shroud. The nacelle support strut was hollow and was used to supply high-pressure air to the jet nozzle. The nacelle was positioned by a series of interchangeable plates shown as item 1 in figure 4. The nacelle positions used in this investigation and the coordinate system used to designate these nacelle positions are shown in figure 5; the reference point on the nacelle is indicated in the figure.

Balance and Auxiliary Equipment

Forces and moments were measured only on the body using the six-component, side-support, strain-gage-type balance described in reference 3. For the present investigation only three components (axial force, normal force, and pitching moment) were measured. The linkage between the body and the balance is indicated in figure 4.

The jet total pressure was measured by the total-pressure tube indicated in figure 2 and the free-stream static pressure was measured by an orifice in the tunnel wall. These pressures were measured with a manometer and recorded with a camera, except the upper range of total pressures ($p_j/p_\infty \geq 7$) for which the range of the manometer board was exceeded and a Bourdon type gage was used.

A simple shadowgraph was used for flow visualization. A beam of parallel light was directed onto the model assembly from one side. The details of the jet structure were then visible on a white background painted on the opposite side of the tunnel. These details were photographically recorded.

TESTS, PROCEDURES, AND DATA REDUCTION

Force and Moment Measurements

Several precautions were taken to insure consistency and reliability of the data. Boundary-layer transition was fixed by a trip wire located 0.3 diameter aft of the apex of the body nose cone. Sublimation tests indicated that the boundary layer was then turbulent over the entire body. Strut interference was minimized by placing the afterbodies more than 3.5 body diameters downstream of the trailing edge of the body-support shroud. Reference 4 shows that the effect of strut interference on body pressures attenuates to a negligible amount in this distance. The afterbodies were forward of the shock waves from the horizontal struts for the angle range of the tests ($-5^\circ \leq \alpha \leq 10^\circ$).

In the discussion of the results of this investigation two types of measured quantities are considered. One is the incremental interference effects of the jet on the axial force, normal force, and pitching-moment coefficients of the entire body. The other is the total axial-force coefficient on the afterbody alone with the jet on (see fig. 1 for definition of afterbody). The procedures for obtaining the incremental and total afterbody coefficients will be discussed separately.

Jet-interference forces.— The interference forces are defined as those acting on the body with the jet on minus those acting on the body with the jet off (nacelle present); these forces were measured in a straightforward fashion. The sequence of operation for each model configuration was to set the angle of attack and then to vary the pressure ratio from jet off to the maximum of about 9 in rapid succession. The forces on the body with the jet off were then subtracted from those with the jet on to obtain the interference quantities directly. This procedure minimized errors in the incremental force measurements due to strain-gage temperature drifts and weight tares due to angle of attack. The quantities obtained in this fashion are designated herein as ΔC_A , ΔC_N , and ΔC_m .

The interference forces were measured in Tunnel No. 1 at a Mach number of 2.94 and a Reynolds number of 0.25×10^6 , based on body diameter. Some data were taken at $R = 0.5 \times 10^6$. The test section total pressures corresponding to the above Reynolds numbers were 14.7 and 30.0 pounds per square inch absolute, respectively.

Total axial force on afterbodies.— The total afterbody axial-force coefficient with jet on C_A is $(C_{A_0} + \Delta C_A)$ where C_{A_0} is the afterbody axial-force coefficient at zero angle of attack with the nacelle and strut removed. This neglects the interference effects of the nacelle and strut. However, measurements of axial force with and without the nacelle showed the interference effects of the nacelle and strut to be sufficiently small, compared to the interference forces of the jet, that neglect of this term did not alter trends. The magnitude of the nacelle and strut interference term $F_n/q_\infty A$ is given in table I.

The quantity C_{A_0} was obtained indirectly. The axial force for the entire body was measured for each afterbody with the nacelle and strut removed. Then the forebody axial force was estimated and subtracted from the total axial force to obtain the afterbody axial force. The forebody axial force was estimated by subtracting the theoretical base plus skin-friction axial force of cylindrical afterbody J^1 from the measured total axial force for the body with afterbody J.

The data used to obtain C_{A_0} were taken in Tunnel No. 2 at a test Mach number of 2.96 and Reynolds number of 0.95×10^6 . To maintain supersonic flow² it was necessary to operate Tunnel No. 2 at a higher Reynolds number than Tunnel No. 1.

Jet Calibration

Two total pressure tubes were used to calibrate the nozzle. One was fixed inside the nacelle (see fig. 2) and the other was mounted on a sting so that the end of the tube was at the center of the jet exit. A jet Mach number of $M_j = 2.71$ was then obtained from the measured pressures by using a one-dimensional flow analysis and assuming no total pressure loss between the nozzle chamber and the exit. The pressure ratio, p_j/p_∞ , was obtained from the calibrated jet-exit Mach number, the chamber pressure, and known tunnel conditions. To avoid the possibility of condensation shocks the air was dried so that the water content was less than 0.00005 pound of water per pound of air. No hysteresis was observed in the nozzle calibration.

¹The base drag was estimated from charts of reference 5 and the skin friction was estimated by the T' method used in reference 6.

²A correction of 0.008 was added to C_{A_0} from Tunnel No. 2 data to allow for Reynolds number effect on skin friction between the two tunnels.

Equivalence of Hot and Cold Jets

Since a cold jet was used in the present investigation, the usefulness of the results depends on relating them to a hot-gas jet. In this investigation the afterbodies are always placed well outside the jet boundary. Therefore, it is necessary for the cold-air jet to provide simulation of only the flow external to the jet boundary. This is equivalent to simulating the jet-boundary shape since the jet boundary is a streamline. A brief summary of the results of reference 7 regarding the equivalence of jet boundaries is given in appendix B.

Accuracy of Data

Uncertainties are summarized in the following table.

| $R \times 10^{-6}$ | α range | ΔC_A | ΔC_N | \bar{x}/d | C_{A_0} | p_j/p_∞ | α |
|--------------------|--|--------------|--------------|-------------|-------------|----------------|-----------------|
| 0.25 | 0° to 2° | ± 0.002 | ± 0.02 | ± 0.25 | ± 0.002 | ± 0.1 | $\pm 0.1^\circ$ |
| | -5° to 0° 2° to 10° | ± 0.005 | | | | | |
| .50 | -5° to 10° | ± 0.005 | | | | | |

The repeatability of the data was found to be consistent with the above table. The accuracy of \bar{x}/d depends strongly on ΔC_N . In the presentation of the data, \bar{x}/d is arbitrarily discarded when the estimated uncertainty is greater than 0.25.

RESULTS AND DISCUSSION

The basic jet-interference data are presented in figures 6 and 7 as a function of the ratio of jet-exit static pressure to free-stream static pressure. Table II shows the organization of these data. The shock waves shown as dotted curves in the inserted sketches on the figures are reproduced from shadowgraph pictures for $p_j/p_\infty \approx 9$ to the extent of visibility of the shock waves in the pictures. The afterbody designation is given in figure 1 and the nacelle-position designation is summarized in figure 5. As pointed out in the Accuracy of Data section, the accuracy of the center-of-pressure measurements decreases rapidly as ΔC_N becomes

small. When the uncertainty in \bar{x}/d exceeds ± 0.25 the center-of-pressure data are not presented. Some free-jet characteristics which might be useful in interpreting the interference effects are presented in appendix B.

Effect of Shock-Wave Boundary-Layer Interaction

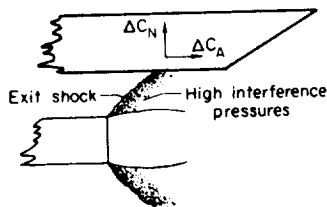
One of the principal and most complex jet interference effects is that caused by the interaction of the shock wave from the jet and the body boundary layer, especially if the boundary layer has appreciable thickness. Unpublished data obtained in the Ames 1- by 3-Foot Supersonic Wind Tunnel by Donald M. Kuehn indicate that the boundary-layer thickness at the afterbody is of the order of $0.2d$ for the model of this investigation when turbulent flow is induced at the nose. This thick boundary layer causes considerable bending of the shock wave near the body. In view of the complex flow phenomena, a reasonably simple theoretical method for estimating the results of this investigation does not appear likely.

A
2
4
9

Effect of Nacelle Position Relative to Afterbody

The interference forces are strongly dependent upon the nacelle position or more correctly on the position of the exit shock wave relative to the afterbody. This is shown by figures 8 and 9. Figure 8 shows the effect of moving the nacelle in an axial direction for fixed values of r/d and p_j/p_∞ . The parameter s is the distance from the shoulder of the afterbody to the point of intersection of the shock wave with the cylindrical body or its imaginary extension. For the slab-sided afterbodies there is a rather sharp peak in ΔC_A when the shock wave is near the shoulder ($s/d = 0$). For afterbody H the slope of the curves of ΔC_A is not as great as for the slab-sided afterbodies. Generally, the data points are not spaced sufficiently close to determine the location and magnitude of the peaks precisely, and for this reason most of the peaks are shown dashed.

The variation of ΔC_A with s/d can be explained qualitatively for the slab-sided afterbodies in figure 8 by use of the idealized, inviscid, two-dimensional model in sketch (a). When the shock wave is well forward of the shoulder (as shown) the axial-force increment is small. As the shock wave is moved aft, ΔC_A begins to increase when the high pressure region reaches the shoulder. The quantity ΔC_A continues to increase as more of the high pressure region impinges on the slab portion of the afterbody until the shock wave crosses the shoulder. Then as the shock wave is moved farther aft, ΔC_A rapidly decreases from its maximum value because the slope of the slab effectively increases the distance between the nacelle and the point of shock-wave impingement on the afterbody.



Sketch (a)

Figure 9 shows the effect of radial position of the nacelle. The curves are cross plots of figure 8 for two fixed values of s/d . As might be expected, the interference forces fall off rapidly as the nacelle is moved away from the body.

Effect of Pressure Ratio

In general, the data of figures 6 and 7 show a large increase in the magnitude of ΔC_A and ΔC_N with increasing pressure ratio. The effect on \bar{x}/d is generally small. The maximum interference axial force for $\alpha = 0$ was obtained for afterbody A with $p_j/p_\infty = 9$ (figs. 6(a) and 6(c)). For these conditions ΔC_A is just equal in magnitude (0.12) to the drag on afterbody A without the nacelle present so that the total afterbody drag with interference is zero. The corresponding normal-force increment is about 0.4 which is the maximum observed.

On the basis of axial-force reduction a highly underexpanded nozzle flow ($p_j/p_\infty \gg 1$) is desirable. An underexpanded nozzle also has less external drag than a fully expanded nozzle. However, an underexpanded nozzle gives less thrust than a fully expanded one, so that the final choice in design for maximum thrust minus axial force must depend on some optimization procedure involving these several variables.

Effect of angle of attack.— In some cases the effects of angle of attack on the interference forces were significant, but in general they were not as great as the effects of nacelle position and jet pressure ratio. (The body and nacelle are always at the same angle of attack.) Typical angle-of-attack effects are summarized in figure 10.

Effect of Afterbody Shape

The intent of preceding sections was to examine the effects of particular variables on jet-afterbody interference. For that purpose it was adequate to consider the incremental quantities ΔC_A and ΔC_N . To compare the various afterbody shapes, however, it is more meaningful to examine the total afterbody axial-force coefficient for $\alpha = 0$ ($C_A = C_{A_0} + \Delta C_A$) since the afterbody with the greatest favorable interference force may have a relatively large axial force without interference.

The afterbody axial-force coefficients without interference, C_{A_0} , are presented in figure 11. The curve for the family of ogival afterbodies is at a lower level and is smoother than that for the slab-sided afterbodies. The shape of the latter curve is probably a result of complex vortex patterns and separation in the afterbody region. The vortices, due to flow separation at the sides of the afterbody, are

indicated for bodies E, B, and C in the pictures of sublimation patterns shown in figure 12. (The dark blotches near the center of the slab surfaces are due to model imperfections.) Shadowgraph pictures (not published) indicate that the flow near the top of the body remained attached aft of the shoulder for afterbodies A, B, and C but was separated at the shoulder for afterbody D.

Figure 13 shows the minimum value of C_A for each afterbody as a function of pressure ratio for the conditions specified in the figure. The ordinate $C_{A_{min}}$ is the sum of C_{A_0} and the maximum negative value of ΔC_A as determined from curves similar to those of figure 8. Because of insufficient data to determine such curves for afterbody A, the data of figures 6(a) and 6(c) were used directly to compute $C_{A_{min}}$ for afterbody A in figures 13(a) and 13(b), respectively. Since the maximum negative values of ΔC_A are not precisely determined, differences less than 0.01 in $C_{A_{min}}$ should not be considered significant in figure 13. Note that $C_{A_{min}} = C_{A_0}$ for jet off. For low jet static-pressure ratios the ogival-afterbody family (dashed curves) offers a lower axial force than the slab-sided afterbody family. However, the slab-sided afterbody family is more effectively influenced by the jet shock wave so that as p_j/p_∞ is increased the slab-sided afterbodies offer the lower axial force.

Ames Research Center
National Aeronautics and Space Administration
Moffett Field, Calif., June 6, 1960

A
2
4
9

NATIONAL AERONAUTICS AND SPACE ADMINISTRATION

TECHNICAL NOTE D-332

AXIAL-FORCE REDUCTION BY INTERFERENCE BETWEEN
JET AND NEIGHBORING AFTERBODY

By William C. Pitts and Lyle E. Wiggins

SUMMARY

Experimental results are presented for an exploratory investigation of the effectiveness of interference between jet and afterbody in reducing the axial force on an afterbody with a neighboring jet. In addition to the interference axial force, measurements are presented of the interference normal force and the center of pressure of the interference normal force. The free-stream Mach number was 2.94, the jet-exit Mach number was 2.71, and the Reynolds number was 0.25×10^6 , based on body diameter. The variables investigated include static-pressure ratio of the jet (up to 9), nacelle position relative to afterbody, angle of attack (-5° to 10°), and afterbody shape. Two families of afterbody shapes were tested. One family consisted of tangent-ogive bodies of revolution with varying length and base areas. The other family was formed by taking a planar slice off a circular cylinder with varying angle between the plane and cylinder. The trends with these variables are shown for conditions near maximum jet-afterbody interference. The interference axial forces are large and favorable. For several configurations the total afterbody axial force is reduced to zero by the interference.

INTRODUCTION

It has been shown in references 1 and 2 that large positive pressures can act on surfaces located in the flow field surrounding a jet. With proper design these interference pressures can be utilized to reduce the afterbody drag of a missile or airplane configuration that has the nacelle neighboring the afterbody. To reduce the drag as much as possible (within limits prescribed by other design factors), it is necessary to know the effect of important variables such as jet-exit pressure ratio, nacelle position relative to the afterbody, afterbody shape, and angle of attack. At present little information of this nature is available for the jet-afterbody interference problem. It is the purpose of this report to present some exploratory results that show trends in the axial-force variation with the above variables near the conditions for maximum jet-afterbody interference. The symbols used in this report are defined in appendix A.

APPARATUS

Wind Tunnel

This investigation was conducted in the Ames 1- by 3-Foot Supersonic Wind Tunnels No. 1 and No. 2. Tunnel No. 1 is a continuous-operation, variable-pressure wind tunnel with a flexible-plate nozzle which provides a Mach number range from 1.4 to 4.0. Tunnel No. 2 is an intermittent-type wind tunnel with a Mach number range from 1.4 to 3.8.

Models

The geometry of the models used in this investigation is shown in figure 1. The body consisted of a cone-cylinder combination with interchangeable afterbodies. Afterbodies A through E were formed by taking planar slices off circular cylinders. Afterbodies F through I were tangent-ogive bodies of revolution. The nacelle was a cone-cylinder combination with a slightly flared afterbody (1.2° half angle). A cross-sectional view of the nacelle is shown in figure 2. The exit to throat area ratio was 3.37 which corresponds to a theoretical exit Mach number of 2.76. The divergent portion of the nozzle was conical and made an 11.2° angle with the axis.

A
2
4
9

Model Supports

The body and the nacelle were supported separately by struts that projected from the side of the tunnel as shown in figures 3 and 4. The body support strut was shielded from the flow by a hollow shroud. The nacelle support strut was hollow and was used to supply high-pressure air to the jet nozzle. The nacelle was positioned by a series of interchangeable plates shown as item 1 in figure 4. The nacelle positions used in this investigation and the coordinate system used to designate these nacelle positions are shown in figure 5; the reference point on the nacelle is indicated in the figure.

Balance and Auxiliary Equipment

Forces and moments were measured only on the body using the six-component, side-support, strain-gage-type balance described in reference 3. For the present investigation only three components (axial force, normal force, and pitching moment) were measured. The linkage between the body and the balance is indicated in figure 4.

The jet total pressure was measured by the total-pressure tube indicated in figure 2 and the free-stream static pressure was measured by an orifice in the tunnel wall. These pressures were measured with a manometer and recorded with a camera, except the upper range of total pressures ($p_j/p_\infty \geq 7$) for which the range of the manometer board was exceeded and a Bourdon type gage was used.

A simple shadowgraph was used for flow visualization. A beam of parallel light was directed onto the model assembly from one side. The details of the jet structure were then visible on a white background painted on the opposite side of the tunnel. These details were photographically recorded.

TESTS, PROCEDURES, AND DATA REDUCTION

Force and Moment Measurements

Several precautions were taken to insure consistency and reliability of the data. Boundary-layer transition was fixed by a trip wire located 0.3 diameter aft of the apex of the body nose cone. Sublimation tests indicated that the boundary layer was then turbulent over the entire body. Strut interference was minimized by placing the afterbodies more than 3.5 body diameters downstream of the trailing edge of the body-support shroud. Reference 4 shows that the effect of strut interference on body pressures attenuates to a negligible amount in this distance. The afterbodies were forward of the shock waves from the horizontal struts for the angle range of the tests ($-5^\circ \leq \alpha \leq 10^\circ$).

In the discussion of the results of this investigation two types of measured quantities are considered. One is the incremental interference effects of the jet on the axial force, normal force, and pitching-moment coefficients of the entire body. The other is the total axial-force coefficient on the afterbody alone with the jet on (see fig. 1 for definition of afterbody). The procedures for obtaining the incremental and total afterbody coefficients will be discussed separately.

Jet-interference forces.- The interference forces are defined as those acting on the body with the jet on minus those acting on the body with the jet off (nacelle present); these forces were measured in a straightforward fashion. The sequence of operation for each model configuration was to set the angle of attack and then to vary the pressure ratio from jet off to the maximum of about 9 in rapid succession. The forces on the body with the jet off were then subtracted from those with the jet on to obtain the interference quantities directly. This procedure minimized errors in the incremental force measurements due to strain-gage temperature drifts and weight tares due to angle of attack. The quantities obtained in this fashion are designated herein as ΔC_A , ΔC_N , and ΔC_m .

The interference forces were measured in Tunnel No. 1 at a Mach number of 2.94 and a Reynolds number of 0.25×10^6 , based on body diameter. Some data were taken at $R = 0.5 \times 10^6$. The test section total pressures corresponding to the above Reynolds numbers were 14.7 and 30.0 pounds per square inch absolute, respectively.

Total axial force on afterbodies.— The total afterbody axial-force coefficient with jet on C_A is $(C_{A_0} + \Delta C_A)$ where C_{A_0} is the afterbody axial-force coefficient at zero angle of attack with the nacelle and strut removed. This neglects the interference effects of the nacelle and strut. However, measurements of axial force with and without the nacelle showed the interference effects of the nacelle and strut to be sufficiently small, compared to the interference forces of the jet, that neglect of this term did not alter trends. The magnitude of the nacelle and strut interference term $F_n/q_\infty A$ is given in table I.

The quantity C_{A_0} was obtained indirectly. The axial force for the entire body was measured for each afterbody with the nacelle and strut removed. Then the forebody axial force was estimated and subtracted from the total axial force to obtain the afterbody axial force. The forebody axial force was estimated by subtracting the theoretical base plus skin-friction axial force of cylindrical afterbody J^1 from the measured total axial force for the body with afterbody J .

The data used to obtain C_{A_0} were taken in Tunnel No. 2 at a test Mach number of 2.96 and Reynolds number of 0.95×10^6 . To maintain supersonic flow² it was necessary to operate Tunnel No. 2 at a higher Reynolds number than Tunnel No. 1.

Jet Calibration

Two total pressure tubes were used to calibrate the nozzle. One was fixed inside the nacelle (see fig. 2) and the other was mounted on a sting so that the end of the tube was at the center of the jet exit. A jet Mach number of $M_j = 2.71$ was then obtained from the measured pressures by using a one-dimensional flow analysis and assuming no total pressure loss between the nozzle chamber and the exit. The pressure ratio, p_j/p_∞ , was obtained from the calibrated jet-exit Mach number, the chamber pressure, and known tunnel conditions. To avoid the possibility of condensation shocks the air was dried so that the water content was less than 0.00005 pound of water per pound of air. No hysteresis was observed in the nozzle calibration.

¹The base drag was estimated from charts of reference 5 and the skin friction was estimated by the T' method used in reference 6.

²A correction of 0.008 was added to C_{A_0} from Tunnel No. 2 data to allow for Reynolds number effect on skin friction between the two tunnels.

Equivalence of Hot and Cold Jets

Since a cold jet was used in the present investigation, the usefulness of the results depends on relating them to a hot-gas jet. In this investigation the afterbodies are always placed well outside the jet boundary. Therefore, it is necessary for the cold-air jet to provide simulation of only the flow external to the jet boundary. This is equivalent to simulating the jet-boundary shape since the jet boundary is a streamline. A brief summary of the results of reference 7 regarding the equivalence of jet boundaries is given in appendix B.

Accuracy of Data

Uncertainties are summarized in the following table.

| $R \times 10^{-6}$ | α range | ΔC_A | ΔC_N | \bar{x}/d | C_{A_0} | p_j/p_∞ | α |
|--------------------|--|--------------|--------------|-------------|-------------|----------------|-----------------|
| 0.25 | 0° to 2° | ± 0.002 | ± 0.02 | ± 0.25 | ± 0.002 | ± 0.1 | $\pm 0.1^\circ$ |
| | -5° to 0° 2° to 10° | ± 0.005 | | | | | |
| .50 | -5° to 10° | ± 0.005 | | | | | |

The repeatability of the data was found to be consistent with the above table. The accuracy of \bar{x}/d depends strongly on ΔC_N . In the presentation of the data, \bar{x}/d is arbitrarily discarded when the estimated uncertainty is greater than 0.25.

RESULTS AND DISCUSSION

The basic jet-interference data are presented in figures 6 and 7 as a function of the ratio of jet-exit static pressure to free-stream static pressure. Table II shows the organization of these data. The shock waves shown as dotted curves in the inserted sketches on the figures are reproduced from shadowgraph pictures for $p_j/p_\infty \approx 9$ to the extent of visibility of the shock waves in the pictures. The afterbody designation is given in figure 1 and the nacelle-position designation is summarized in figure 5. As pointed out in the Accuracy of Data section, the accuracy of the center-of-pressure measurements decreases rapidly as ΔC_N becomes

small. When the uncertainty in \bar{x}/d exceeds ± 0.25 the center-of-pressure data are not presented. Some free-jet characteristics which might be useful in interpreting the interference effects are presented in appendix B.

Effect of Shock-Wave Boundary-Layer Interaction

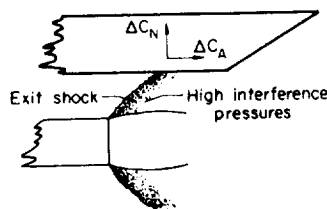
One of the principal and most complex jet interference effects is that caused by the interaction of the shock wave from the jet and the body boundary layer, especially if the boundary layer has appreciable thickness. Unpublished data obtained in the Ames 1- by 3-Foot Supersonic Wind Tunnel by Donald M. Kuehn indicate that the boundary-layer thickness at the afterbody is of the order of $0.2d$ for the model of this investigation when turbulent flow is induced at the nose. This thick boundary layer causes considerable bending of the shock wave near the body. In view of the complex flow phenomena, a reasonably simple theoretical method for estimating the results of this investigation does not appear likely.

A
2
4
9

Effect of Nacelle Position Relative to Afterbody

The interference forces are strongly dependent upon the nacelle position or more correctly on the position of the exit shock wave relative to the afterbody. This is shown by figures 8 and 9. Figure 8 shows the effect of moving the nacelle in an axial direction for fixed values of r/d and p_j/p_∞ . The parameter s is the distance from the shoulder of the afterbody to the point of intersection of the shock wave with the cylindrical body or its imaginary extension. For the slab-sided afterbodies there is a rather sharp peak in ΔC_A when the shock wave is near the shoulder ($s/d = 0$). For afterbody H the slope of the curves of ΔC_A is not as great as for the slab-sided afterbodies. Generally, the data points are not spaced sufficiently close to determine the location and magnitude of the peaks precisely, and for this reason most of the peaks are shown dashed.

The variation of ΔC_A with s/d can be explained qualitatively for the slab-sided afterbodies in figure 8 by use of the idealized, inviscid, two-dimensional model in sketch (a). When the shock wave is well forward of the shoulder (as shown) the axial-force increment is small. As the shock wave is moved aft, ΔC_A begins to increase when the high pressure region reaches the shoulder. The quantity ΔC_A continues to increase as more of the high pressure region impinges on the slab portion of the afterbody until the shock wave crosses the shoulder. Then as the shock wave is moved farther aft, ΔC_A rapidly decreases from its maximum value because the slope of the slab effectively increases the distance between the nacelle and the point of shock-wave impingement on the afterbody.



Sketch (a)

Figure 9 shows the effect of radial position of the nacelle. The curves are cross plots of figure 8 for two fixed values of s/d . As might be expected, the interference forces fall off rapidly as the nacelle is moved away from the body.

Effect of Pressure Ratio

In general, the data of figures 6 and 7 show a large increase in the magnitude of ΔC_A and ΔC_N with increasing pressure ratio. The effect on \bar{x}/d is generally small. The maximum interference axial force for $\alpha = 0$ was obtained for afterbody A with $p_j/p_\infty = 9$ (figs. 6(a) and 6(c)). For these conditions ΔC_A is just equal in magnitude (0.12) to the drag on afterbody A without the nacelle present so that the total afterbody drag with interference is zero. The corresponding normal-force increment is about 0.4 which is the maximum observed.

On the basis of axial-force reduction a highly underexpanded nozzle flow ($p_j/p_\infty \gg 1$) is desirable. An underexpanded nozzle also has less external drag than a fully expanded nozzle. However, an underexpanded nozzle gives less thrust than a fully expanded one, so that the final choice in design for maximum thrust minus axial force must depend on some optimization procedure involving these several variables.

Effect of angle of attack.— In some cases the effects of angle of attack on the interference forces were significant, but in general they were not as great as the effects of nacelle position and jet pressure ratio. (The body and nacelle are always at the same angle of attack.) Typical angle-of-attack effects are summarized in figure 10.

Effect of Afterbody Shape

The intent of preceding sections was to examine the effects of particular variables on jet-afterbody interference. For that purpose it was adequate to consider the incremental quantities ΔC_A and ΔC_N . To compare the various afterbody shapes, however, it is more meaningful to examine the total afterbody axial-force coefficient for $\alpha = 0$ ($C_A = C_{A_0} + \Delta C_A$) since the afterbody with the greatest favorable interference force may have a relatively large axial force without interference.

The afterbody axial-force coefficients without interference, C_{A_0} , are presented in figure 11. The curve for the family of ogival afterbodies is at a lower level and is smoother than that for the slab-sided afterbodies. The shape of the latter curve is probably a result of complex vortex patterns and separation in the afterbody region. The vortices, due to flow separation at the sides of the afterbody, are

indicated for bodies E, B, and C in the pictures of sublimation patterns shown in figure 12. (The dark blotches near the center of the slab surfaces are due to model imperfections.) Shadowgraph pictures (not published) indicate that the flow near the top of the body remained attached aft of the shoulder for afterbodies A, B, and C but was separated at the shoulder for afterbody D.

Figure 13 shows the minimum value of C_A for each afterbody as a function of pressure ratio for the conditions specified in the figure. The ordinate $C_{A_{min}}$ is the sum of C_{A_0} and the maximum negative value of ΔC_A as determined from curves similar to those of figure 8. Because of insufficient data to determine such curves for afterbody A, the data of figures 6(a) and 6(c) were used directly to compute $C_{A_{min}}$ for afterbody A in figures 13(a) and 13(b), respectively. Since the maximum negative values of ΔC_A are not precisely determined, differences less than 0.01 in $C_{A_{min}}$ should not be considered significant in figure 13. Note that $C_{A_{min}} = C_{A_0}$ for jet off. For low jet static-pressure ratios the ogival-afterbody family (dashed curves) offers a lower axial force than the slab-sided afterbody family. However, the slab-sided afterbody family is more effectively influenced by the jet shock wave so that as p_j/p_∞ is increased the slab-sided afterbodies offer the lower axial force.

Ames Research Center

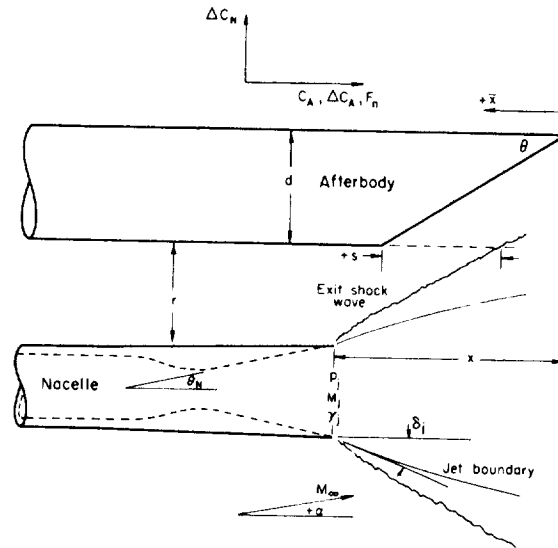
National Aeronautics and Space Administration
Moffett Field, Calif., June 6, 1960

A
2
4
9

APPENDIX A

SYMBOLS

Symbols and sign conventions are shown in sketch (b)



Sketch (b)

- A body cylinder cross-sectional area, sq in.
- C_A total afterbody axial-force coefficient with jet on,
 $C_{A_0} + \Delta C_A$
- C_{A_0} afterbody axial-force coefficient with nacelle and strut removed
and $\alpha = 0$, based on $q_\infty A$
- $C_{A_{min}}$ minimum value of C_A
- ΔC_A interference axial-force coefficient,

$$\frac{(\text{jet-on axial force}) - (\text{jet-off axial force})}{q_\infty A}$$
- ΔC_N interference normal-force coefficient,

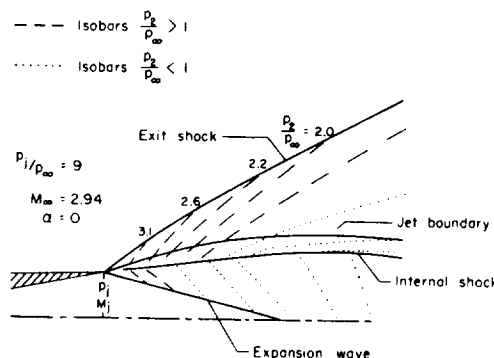
$$\frac{(\text{jet-on normal force}) - (\text{jet-off normal force})}{q_\infty A}$$

| | | |
|--------------|--|---|
| ΔC_m | interference pitching-moment coefficient referred to the rearmost point of the afterbody, $\frac{(\text{jet-on pitching moment}) - (\text{jet-off pitching moment})}{q_\infty A d}$ | |
| d | body cylinder diameter, in. | |
| F_n | interference axial force acting on the body due to the presence of the nacelle and strut, lb | |
| h | base diameter of ogival afterbodies, in. | |
| M_j | jet-exit Mach number | A |
| M_∞ | free-stream Mach number | 2 |
| p_j | jet-exit static pressure, lb/sq in. | 4 |
| p_2 | static pressure immediately aft of exit shock wave, lb/sq in. | 9 |
| p_∞ | free-stream static pressure, lb/sq in. | |
| q_∞ | free-stream dynamic pressure, lb/sq in. | |
| R | Reynolds number based on body diameter | |
| r | radial position of nacelle base, in. | |
| x | axial position of nacelle base, in. | |
| \bar{x} | center of interference pressure, $\frac{\Delta C_{T1}}{\Delta C_{T1}} d$, in. | |
| s | intersection point of jet shock with extended body cylinder, in. | |
| α | angle of attack of nacelle and body configuration, deg | |
| γ_j | ratio of specific heats in jet | |
| δ_j | initial angle between jet boundary and jet center line, deg | |
| θ_N | angle between divergent portion of nozzle and center line, deg | |
| θ | angle between slab portion of afterbody and body center line in vertical plane, deg | |

APPENDIX B

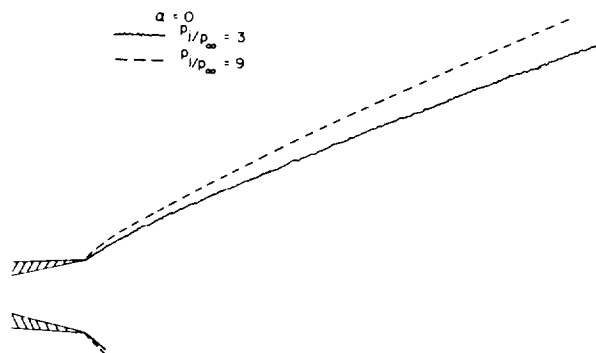
EXPERIMENTAL OBSERVATIONS AND ESTIMATION
OF FREE-JET CHARACTERISTICS

Some experimental observations of free-jet characteristics are presented in this paragraph. Sketch (c) shows the structure of the jet for the model of the present investigation. The shock shapes and the jet-boundary shape were determined from a shadowgraph picture. The pressure rise across the exit shock was computed by assuming local two-dimensional flow. Schäfer's theoretical model (ref. 8) was used as a guide to fill in the qualitative isobar detail. It might be expected from examination of the isobar structure that interference effects on a neighboring surface depend strongly on the relative positions of the surface and jet. Sketch (d) (reproduced from shadowgraph pictures) shows the effect on the shock-wave shape of increasing the static-pressure ratio from 3 to 9 for $\alpha = 0^\circ$. Sketch (e) shows the effect on the shock-wave shape of increasing the angle of attack from 0° to 8° for $p_j/p_\infty = 9$. The primary effect of angle of attack is on the lee side of the nacelle where shadowgraph pictures indicate flow separation. The flow separation causes the exit shock-wave system to move forward progressively with increasing angle of attack. The separation appeared to start when the nacelle angle of attack exceeded about 2° .

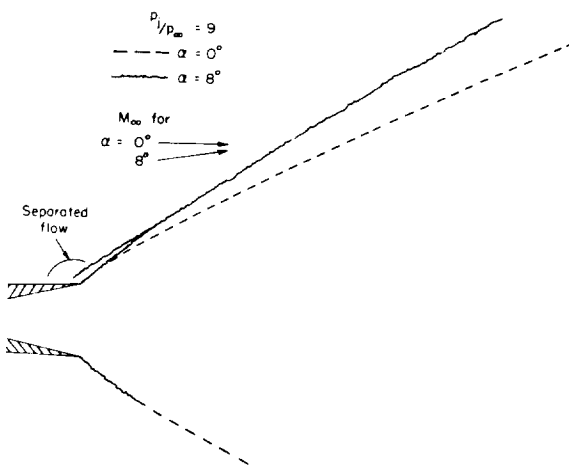


Sketch (c)

$\alpha = 0$
 $p_1/p_\infty = 3$
 $p_1/p_\infty = 9$



Sketch (d)



Sketch (e)

Charts are presented in reference 7 for estimating the shape of a jet boundary when it exhausts into still air. An equivalence rule is presented which states that two jet-boundary shapes are equivalent to a practical degree of accuracy if the initial slope of the jet boundary is the same for both and if γ_j is not too greatly different. This rule was demonstrated to be true for the jet exhausting into still air and was suggested to be true for a jet exhausting into a supersonic flow. It is demonstrated in figure 14 that the charts and equivalence rule of reference 7 are adequate for estimating the jet-boundary shapes for the supersonic flow conditions of this investigation. The estimated shapes are compared with boundary shapes recorded on shadowgraph pictures when $\alpha = 0^\circ$ and the external flow over the nacelle was not separated. Since an infinite number of combinations of M_j , θ_N , γ_j , and p_j/p_∞ will duplicate the initial slope of the jet boundary, several combinations were chosen for each comparison to show that considerable latitude is available in the choice of parameters. The poor agreement between the experimental jet-boundary shape and the theoretical jet-boundary shape for $\theta_N = 20^\circ$ (bottom table, fig. 14) indicates that θ_N should be chosen to simulate as nearly as possible the actual geometry. From the above discussion the boundary shape of a cold-air jet is equivalent to that of a hot-gas jet, provided they both have the same value of δ_j . On this basis, figure 15 was constructed for the nozzle of this investigation. For small pressure ratios the effect of γ_j is quite small.

The exit-shock shape can also be predicted to good engineering accuracy when $\alpha = 0^\circ$ and the flow over the afterbody of the nacelle is not separated (see fig. 16). The shaded regions represent the range of shock-wave shapes obtained for the estimated jet-boundary shapes in figure 14 with corresponding pressure ratio. (The shock wave for the smallest diameter jet-boundary shape at the bottom of figure 14 was excluded from figure 16.) The method of estimation is essentially that of reference 9 for axisymmetric bodies. For the present estimation the initial inclination of the exit shock was determined by assuming local two-dimensional flow at the nozzle exit.

REFERENCES

1. Bressette, Walter E., and Leiss, Abraham: Investigation of Jet Effects on a Flat Surface Downstream of the Exit of a Simulated Turbojet Nacelle at a Free-Stream Mach Number of 1.39. NACA RM L55L13, 1956.
2. Wasserbauer, Joseph F., and Englert, Gerald W.: Interaction of an Exhaust Jet and Elementary Contoured Surfaces Located in a Supersonic Air Stream. NACA RM E56A16, 1956.
3. Katzen, Elliott D., Kuehn, Donald M., and Hill, William A., Jr.: Investigation of the Effects of Profile Shape on the Aerodynamic and Structural Characteristics of Thin, Two-Dimensional Airfoils at Supersonic Speeds. NACA TN 4039, 1957.
4. Klann, John L., and Huff, Ronald G.: Experimental Investigation of Interference Effects of Lateral-Support Struts on Afterbody Pressures at Mach 1.9. NACA RM E56C16, 1956.
5. Love, Eugene S.: The Base Pressure at Supersonic Speeds on Two-Dimensional Airfoils and Bodies of Revolution (With and Without Fins) Having Turbulent Boundary Layers. NACA RM L53C02, 1953.
6. Sommer, Simon C., and Short, Barbara J.: Free-Flight Measurements of Turbulent-Boundary-Layer Skin Friction in the Presence of Severe Aerodynamic Heating at Mach Numbers From 2.8 to 7.0. NACA TN 3391, 1955.
7. Love, Eugene S., Woodling, Mildred J., and Lee, Louise P.: Boundaries of Supersonic Axisymmetric Free Jets. NACA RM L56G18, 1956.
8. Schäfer, M.: Steady Supersonic Flows. British M.A.P. Volkenrode Reps. and Translations No. 995, April 15, 1948. Reps. and Translations No. 996, May 1, 1948.
9. Love, Eugene S., and Long, Ronald H.: A Rapid Method for Predicting Attached-Shock Shape. NACA TN 4167, 1957.

TABLE I.- EFFECT OF NACELLE ON AFTERBODY AXIAL FORCE WITH JET OFF, $F_n/q_\infty A$, $\alpha = 0^\circ$

| Afterbody | x/d r/d | | 0.8 | 1.2 | 1.6 | 2.0 | 2.4 | 2.8 | 3.2 | 3.6 | 4.0 |
|-----------|----------------|-------|-------|-------|-------|-------|-------|-------|-------|-------|-------|
| A | 0.1 | --- | --- | --- | --- | --- | --- | --- | 0.015 | --- | --- |
| | .5 | --- | --- | --- | --- | --- | 0.003 | --- | --- | 0.009 | --- |
| B | .1 | --- | 0.006 | 0.013 | 0.013 | 0.013 | .015 | --- | --- | --- | --- |
| | .5 | --- | --- | --- | -.003 | .001 | .007 | 0.007 | --- | --- | --- |
| | .9 | --- | --- | --- | --- | -.006 | .004 | -.003 | --- | --- | --- |
| C | .1 | --- | --- | .012 | .006 | -.005 | .006 | --- | --- | --- | --- |
| | .5 | --- | --- | --- | .003 | .008 | .013 | .009 | --- | -.003 | 0.008 |
| | .9 | --- | --- | --- | --- | .006 | .001 | .007 | .004 | .014 | --- |
| D | .1 | 0.013 | --- | --- | .009 | --- | --- | --- | --- | --- | --- |
| E | .1 | --- | --- | .007 | --- | --- | --- | --- | --- | --- | --- |
| | .5 | --- | --- | .000 | .005 | .017 | .016 | .016 | .016 | --- | --- |
| | .9 | --- | --- | --- | --- | -.006 | -.004 | .004 | -.003 | --- | --- |
| F | .5 | --- | --- | --- | --- | --- | .006 | --- | --- | --- | --- |
| G | .1 | .011 | --- | --- | --- | --- | --- | --- | --- | --- | --- |
| | .5 | --- | --- | .002 | --- | .006 | --- | --- | --- | --- | --- |
| H | .1 | .017 | --- | .018 | --- | --- | --- | --- | --- | --- | --- |
| | .5 | --- | --- | --- | .003 | .008 | .010 | --- | .012 | --- | --- |
| I | .5 | --- | --- | --- | --- | --- | .011 | --- | --- | --- | --- |
| J | .1 | .011 | --- | --- | --- | --- | --- | --- | --- | --- | --- |

TABLE II.- INDEX TO BASIC DATA IN FIGURES 6 AND 7

| Nacelle position | | Figure 6 slabbed afterbodies | | | | | Figure 7 ogival afterbodies | | | | |
|------------------|-----|---------------------------------|-----|------|------|------|--------------------------------|-----|-----|-----|-----|
| r/d | x/d | A | B | C | D | E | F | G | H | I | J |
| 0.1 ↓ | 0.8 | - | - | - | (ff) | - | - | (b) | (e) | - | (p) |
| | 1.2 | - | (d) | (p) | - | (hh) | - | - | (f) | - | - |
| | 1.6 | - | (e) | (q) | (gg) | - | - | - | - | - | - |
| | 2.0 | - | (f) | (r) | - | - | - | - | - | - | - |
| | 2.4 | - | (g) | (s) | - | - | - | - | - | - | - |
| | 2.8 | - | - | - | - | - | - | - | - | - | - |
| | 3.2 | (a) | - | - | - | - | - | - | - | - | - |
| | 3.6 | - | - | - | - | - | - | - | - | - | - |
| | 4.0 | - | - | - | - | - | - | - | - | - | - |
| | 4.4 | - | - | - | - | - | - | - | - | - | - |
| .5 ↓ | 1.6 | - | (h) | (t) | - | (ii) | - | (c) | (g) | - | - |
| | 2.0 | - | (i) | (u) | - | (jj) | - | - | (h) | - | - |
| | 2.4 | (b) | (j) | (v) | - | (kk) | (a) | (d) | (i) | (o) | - |
| | 2.8 | - | (k) | (w) | - | (ll) | - | - | - | - | - |
| | 3.2 | - | (l) | (x) | - | (mm) | - | - | (j) | - | - |
| | 3.6 | (c) | - | (y) | - | - | - | - | - | - | - |
| | 4.0 | - | - | (z) | - | - | - | - | - | - | - |
| | 4.4 | - | - | - | - | - | - | - | - | - | - |
| | 4.8 | - | - | - | - | - | - | - | - | - | - |
| | 5.2 | - | - | - | - | - | - | - | - | - | - |
| .9 ↓ | 2.0 | - | - | (aa) | - | - | - | - | (k) | - | - |
| | 2.4 | - | - | (bb) | - | (nn) | - | - | (l) | - | - |
| | 2.8 | - | (m) | (cc) | - | (oo) | - | - | (m) | - | - |
| | 3.2 | - | (n) | (dd) | - | (pp) | - | - | (n) | - | - |
| | 3.6 | - | (o) | (ee) | - | - | - | - | - | - | - |

A
2
4
9

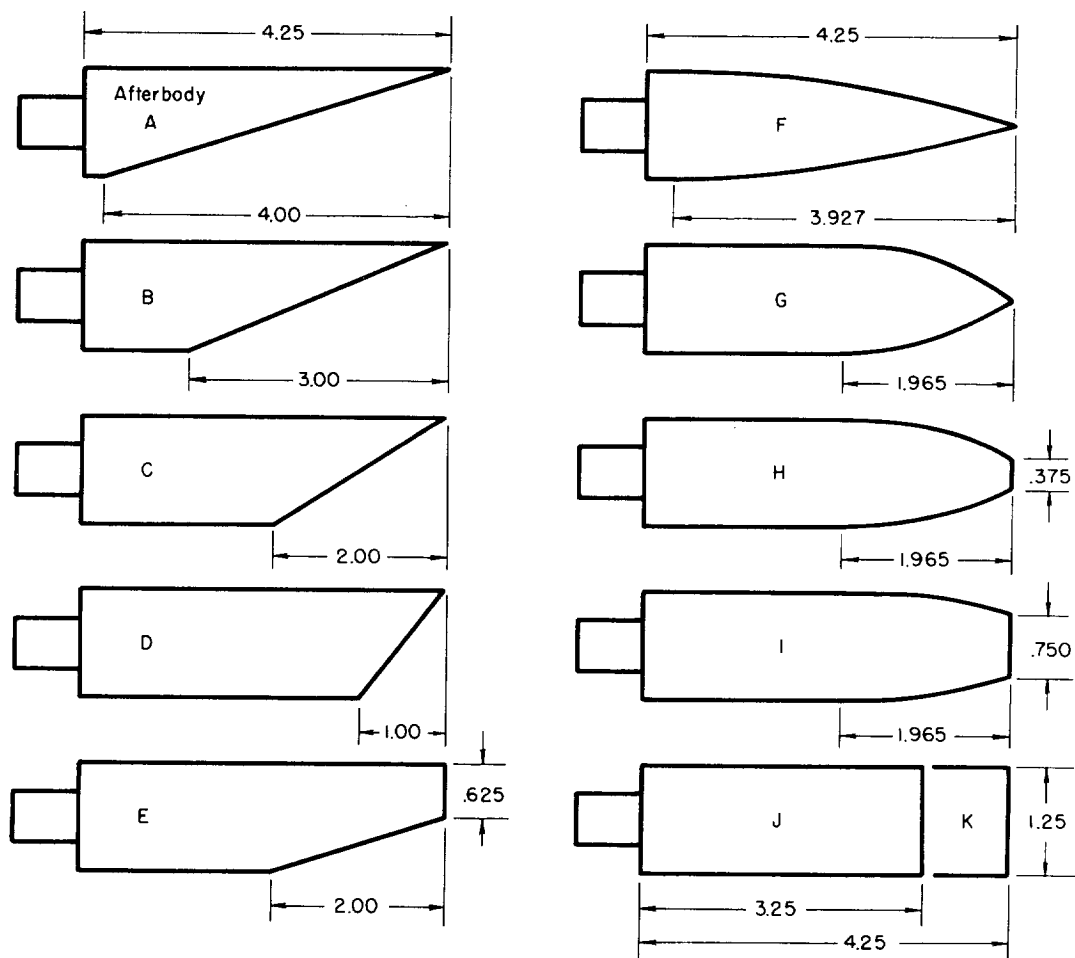
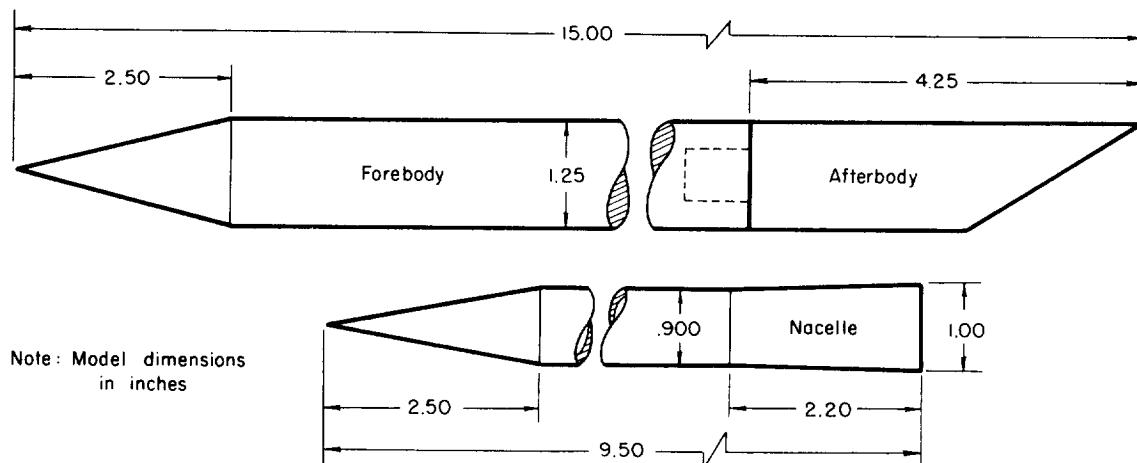


Figure 1.- Model geometry.

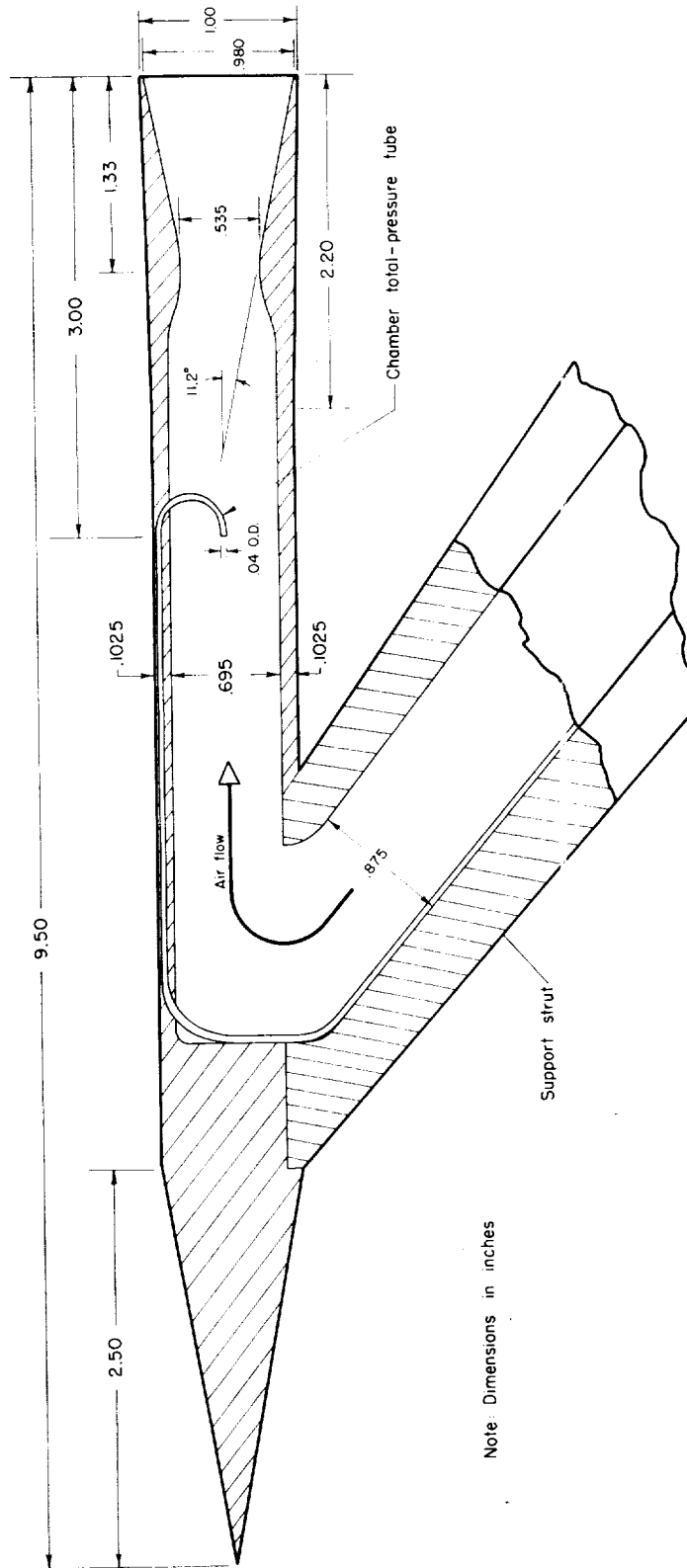


Figure 2.- Details of nacelle geometry.



A-23988.1

Figure 3.- Model installed in the wind tunnel.

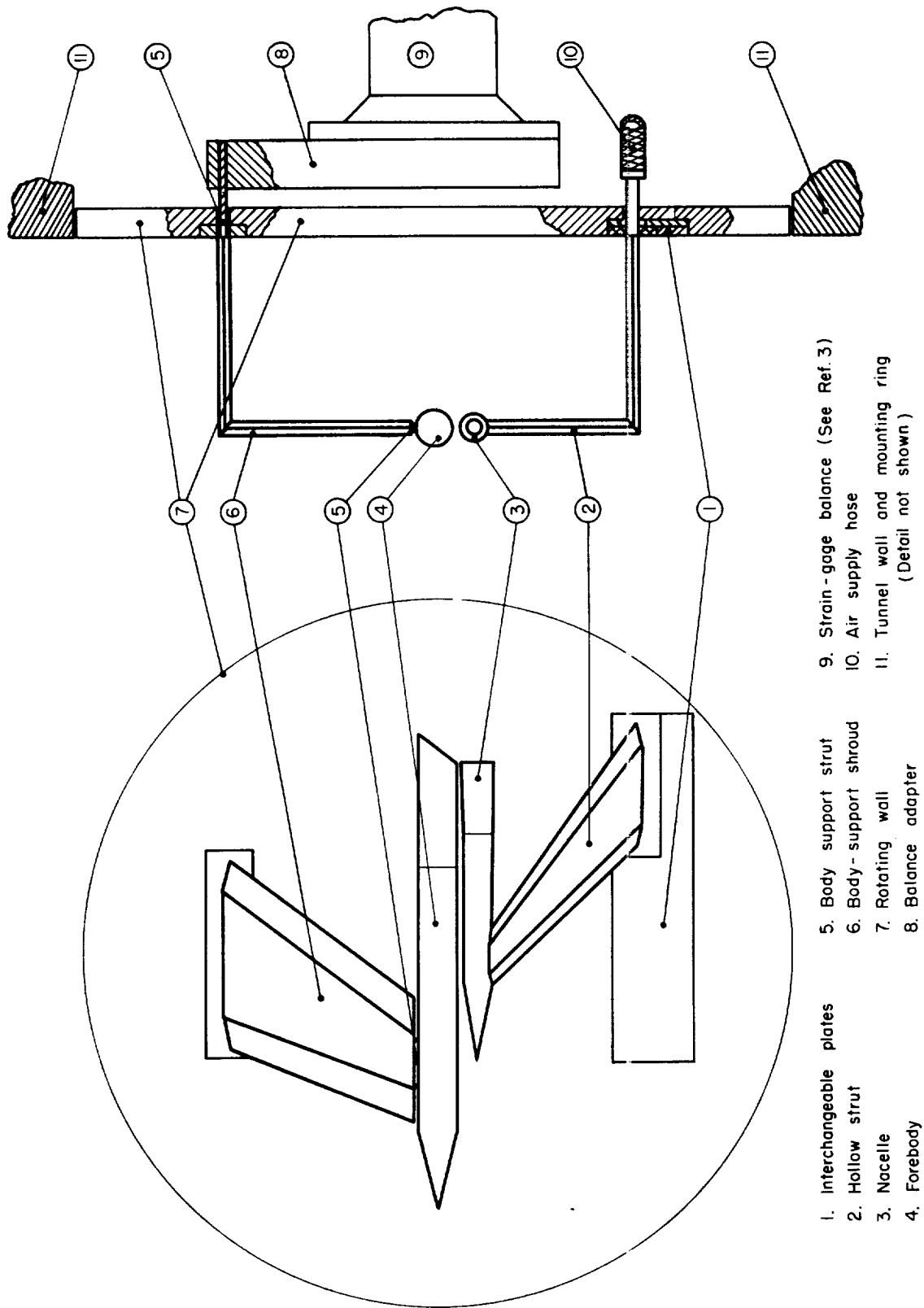


Figure 4.- Model and support assembly in wind tunnel.

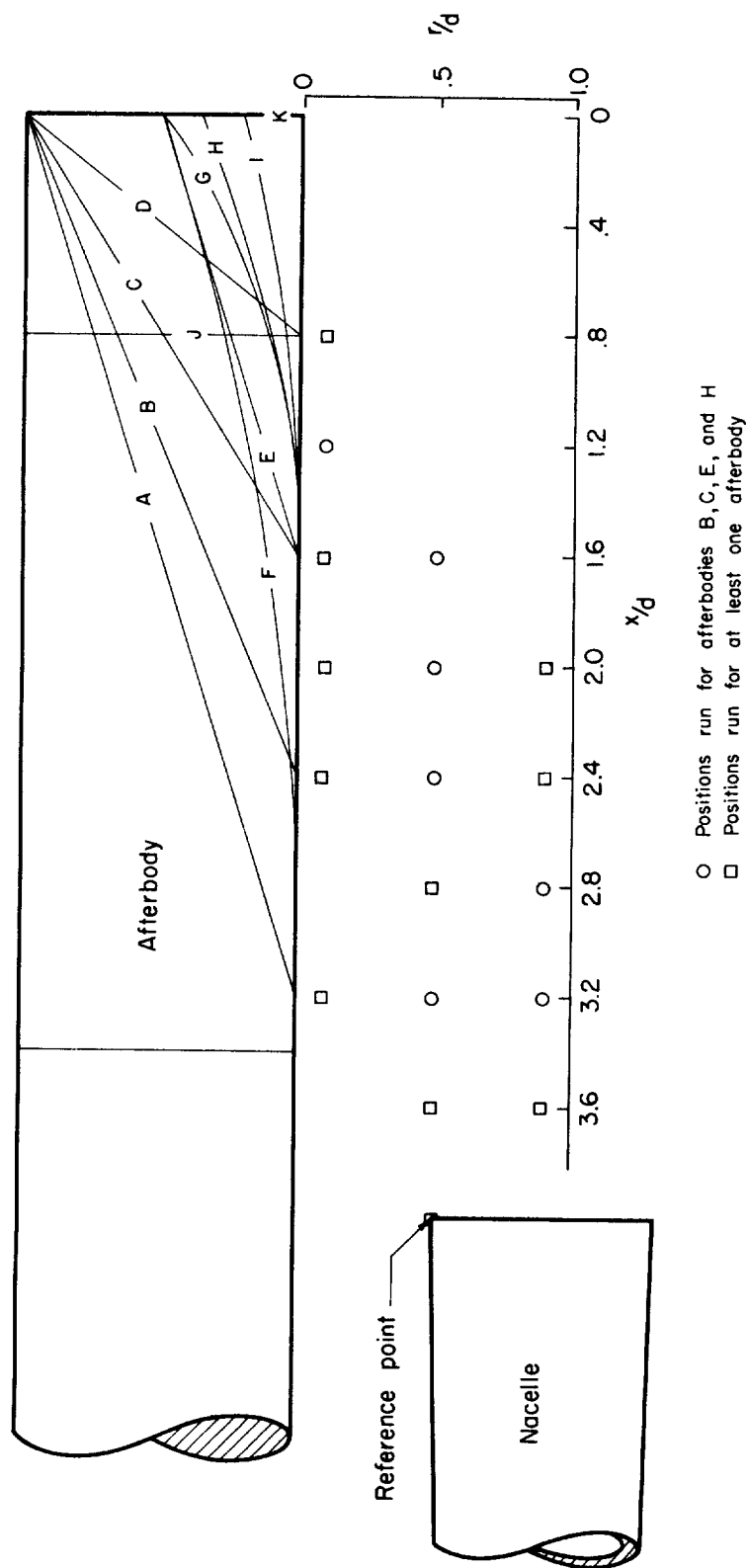
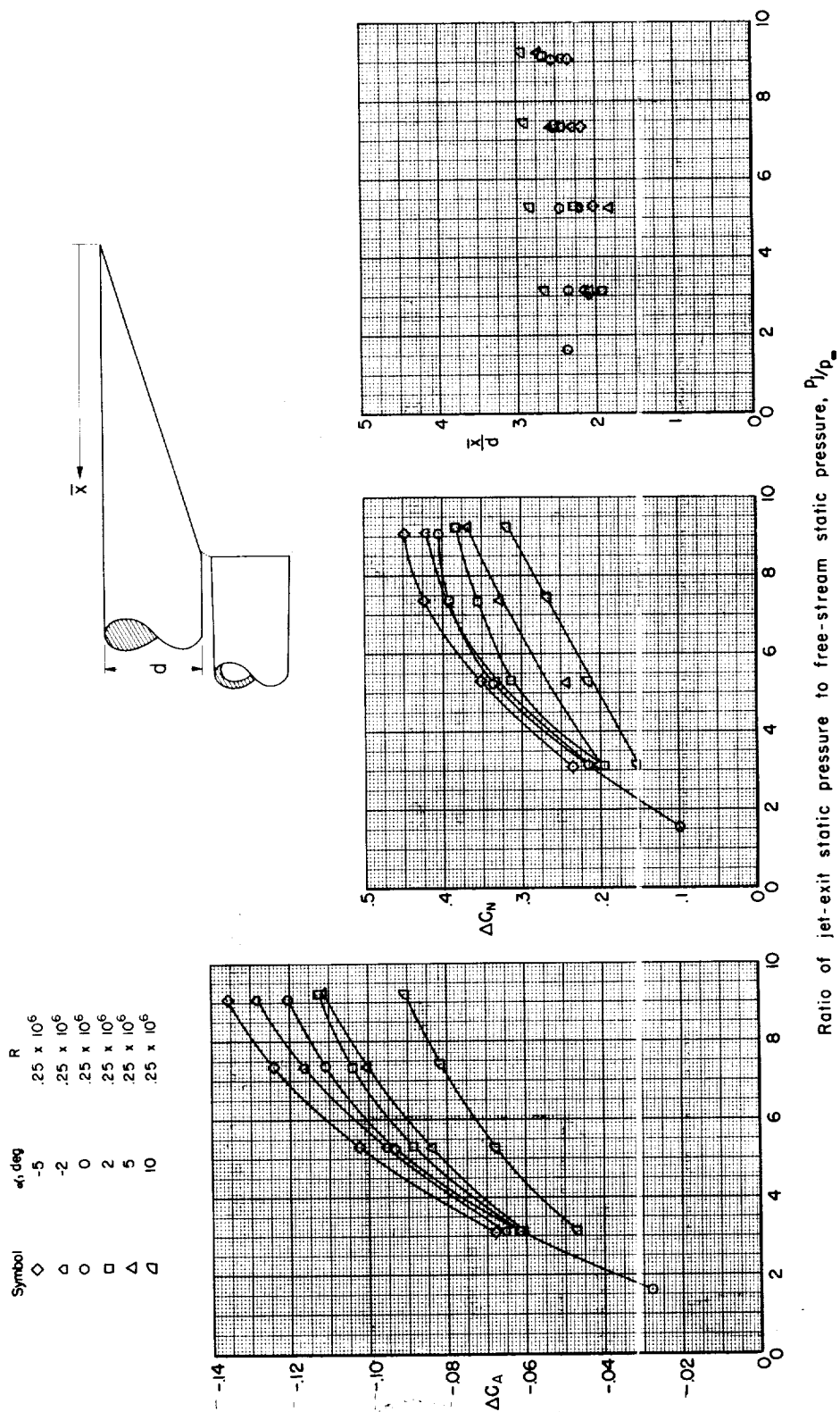


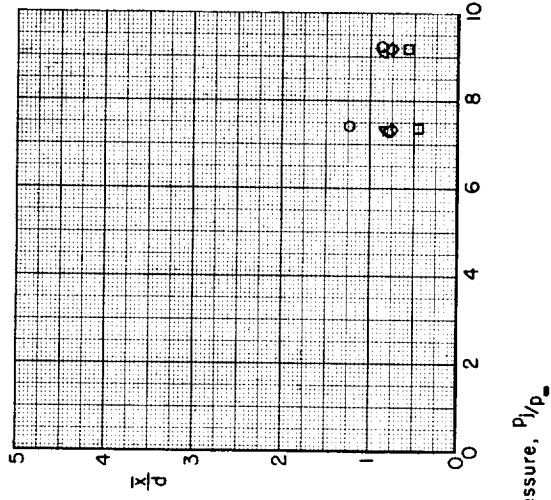
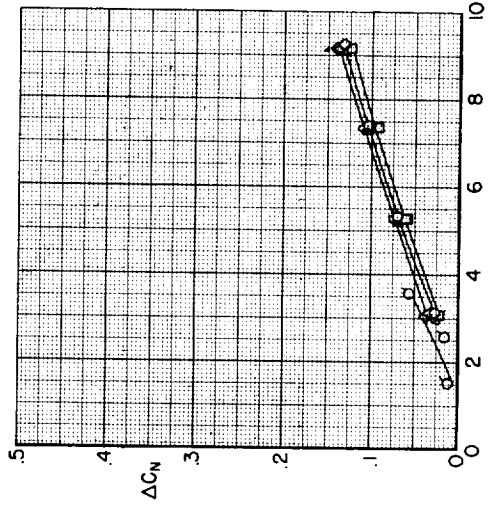
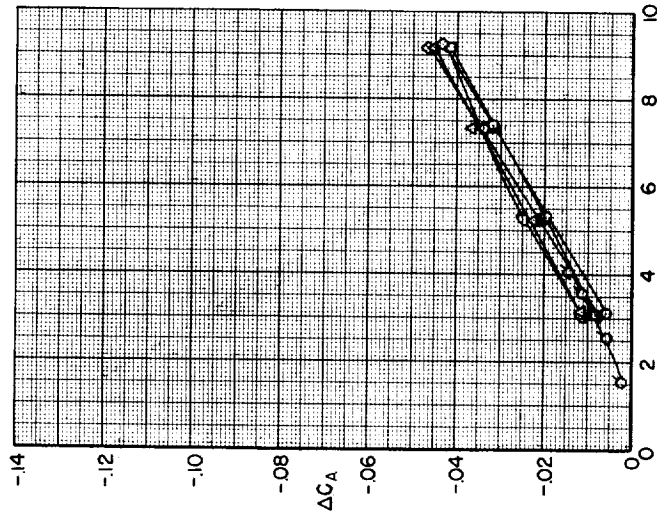
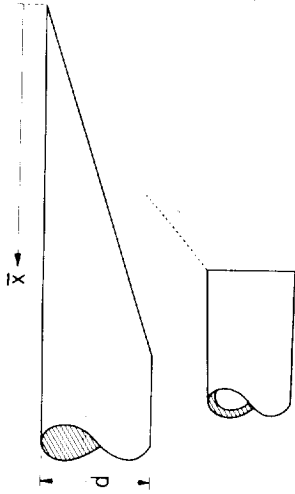
Figure 5.- Coordinates for locating nacelle position relative to the body.



(a) Body A, $r/d = 0.1$, $x/d = 3.2$.

Figure 6.- Effect of pressure ratio on interference forces and center of pressure for slatted afterbodies.

| Symbol | α , deg | R |
|-------------|----------------|-------------------|
| \diamond | -5 | $.25 \times 10^6$ |
| Δ | -2 | $.25 \times 10^6$ |
| \circ | 0 | $.25 \times 10^6$ |
| \square | 2 | $.25 \times 10^6$ |
| \triangle | 5 | $.25 \times 10^6$ |
| ∇ | 10 | $.25 \times 10^6$ |
| \circ | 0 | $.50 \times 10^6$ |



Ratio of jet-exit static pressure to free-stream static pressure, P_1/P_∞

(b) Body A, $r/d = 0.5$, $x/d = 2.4$.

Figure 6.- Continued.

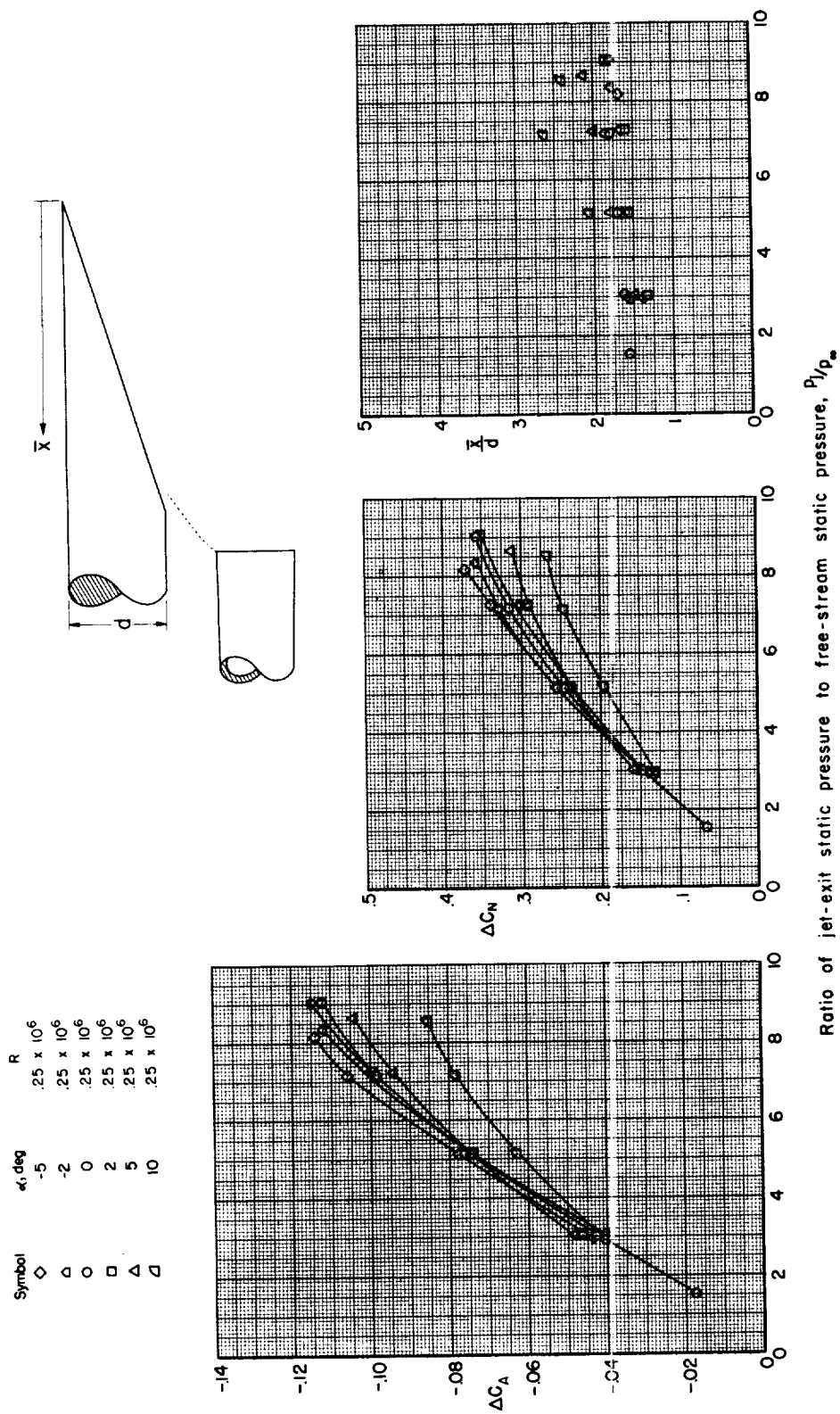
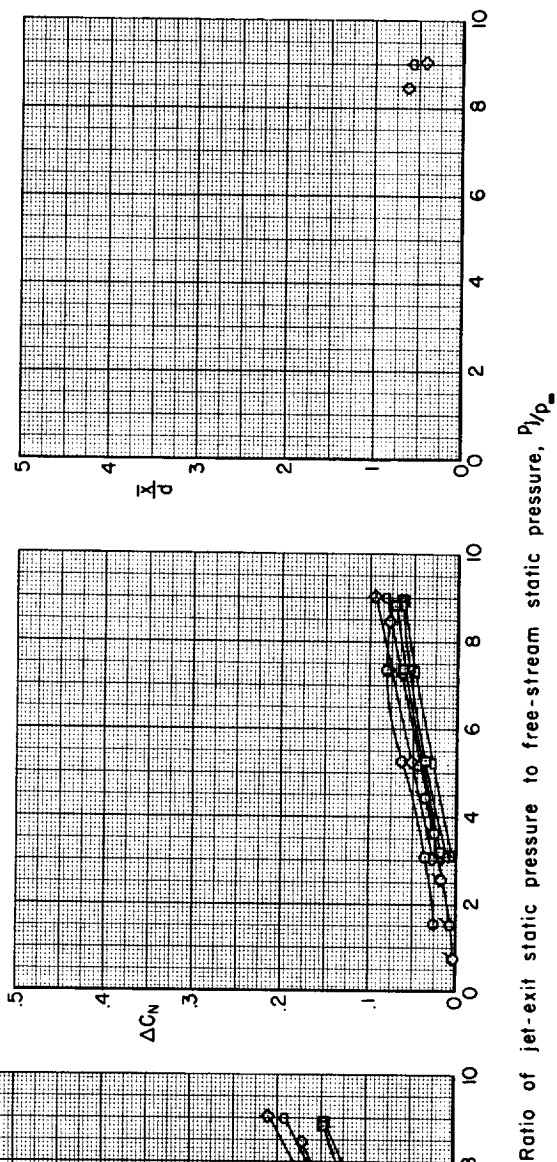
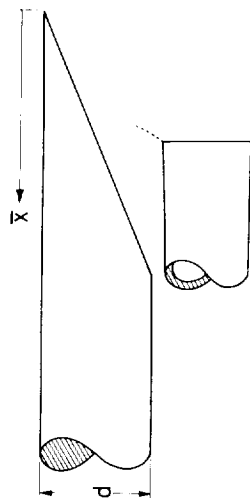
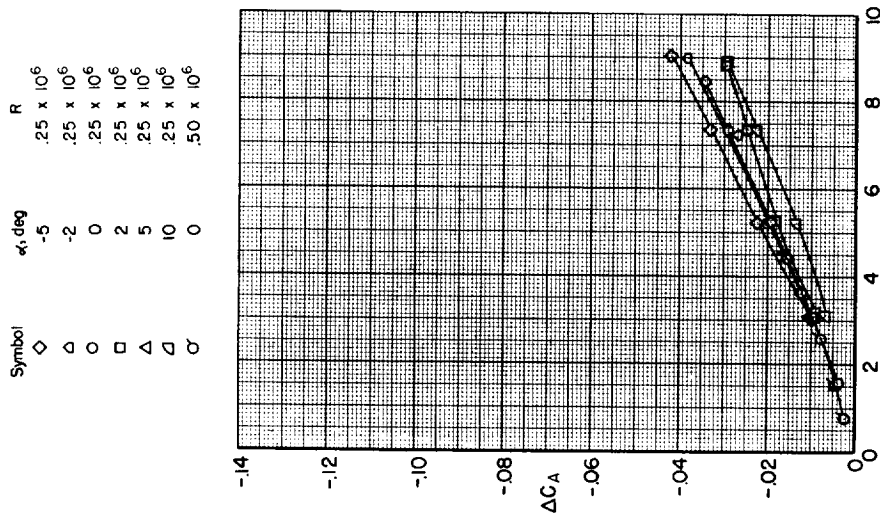
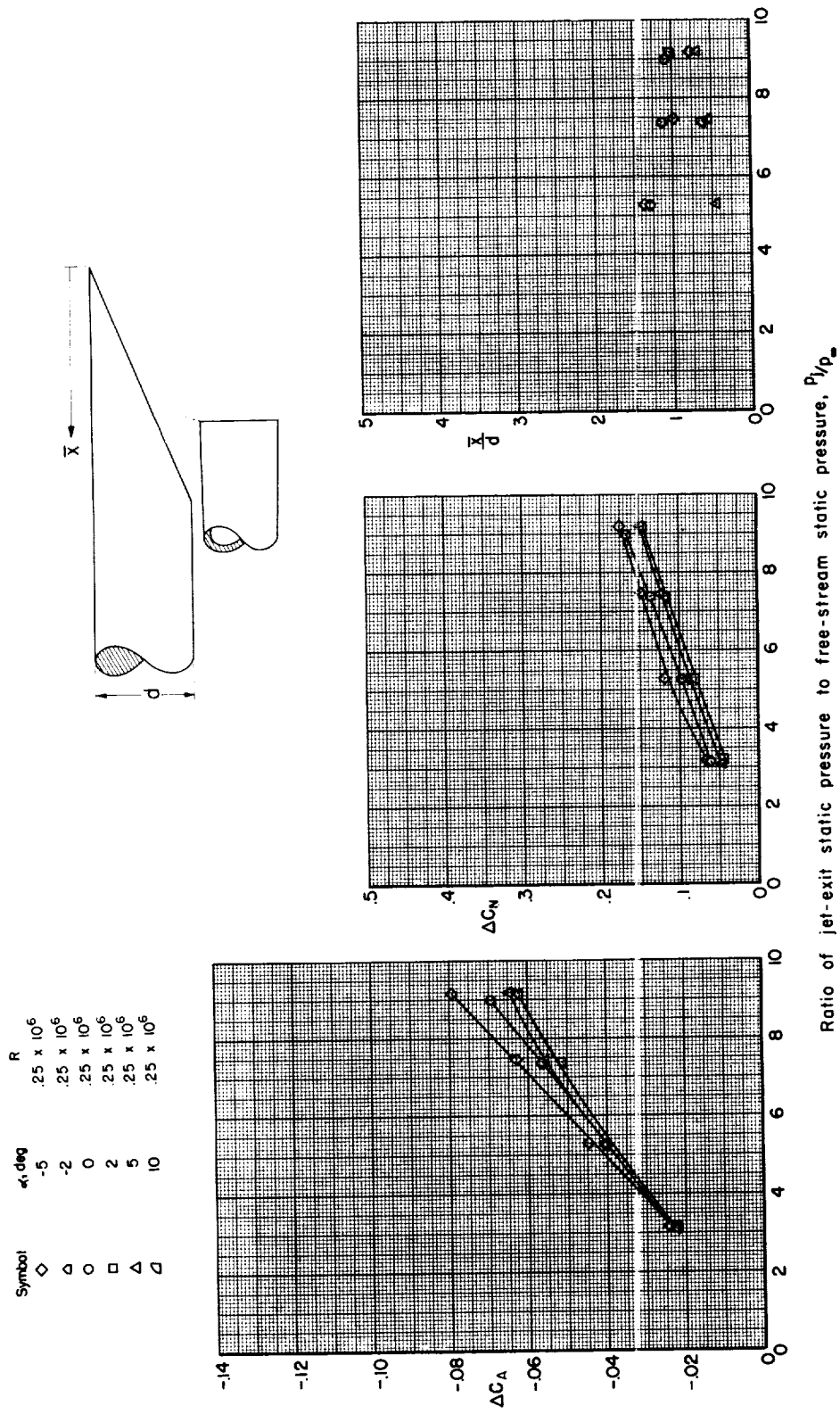


Figure 6.- Continued.



(d) Body B, $r/d = 0.1$, $x/d = 1.2$.

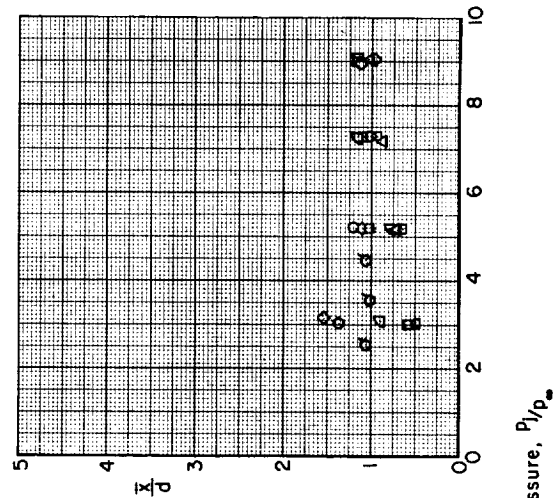
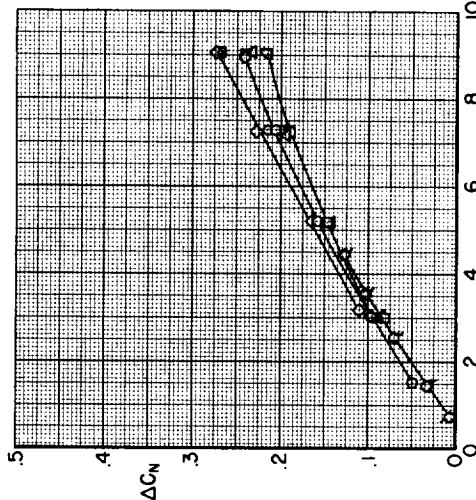
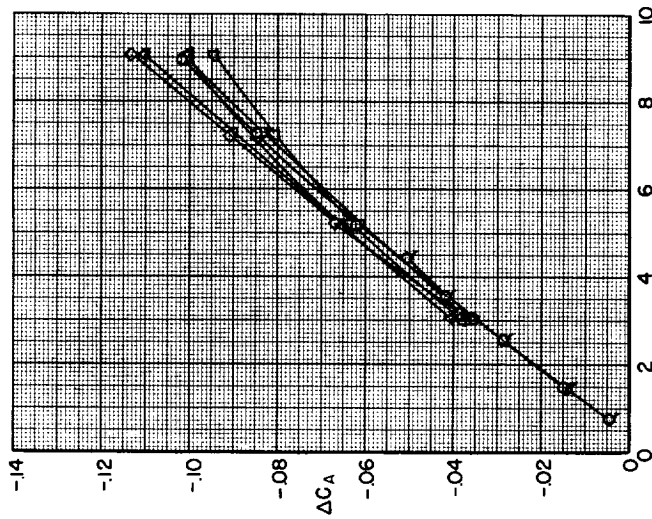
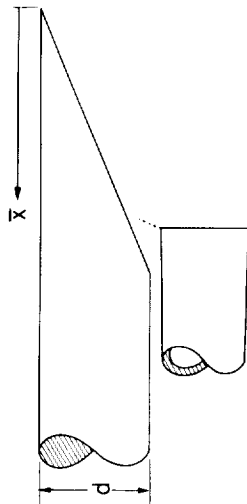
Figure 6.- Continued.



(e) Body B, $r/d = 0.1$, $x/d = 1.6$.

Figure 6.- Continued.

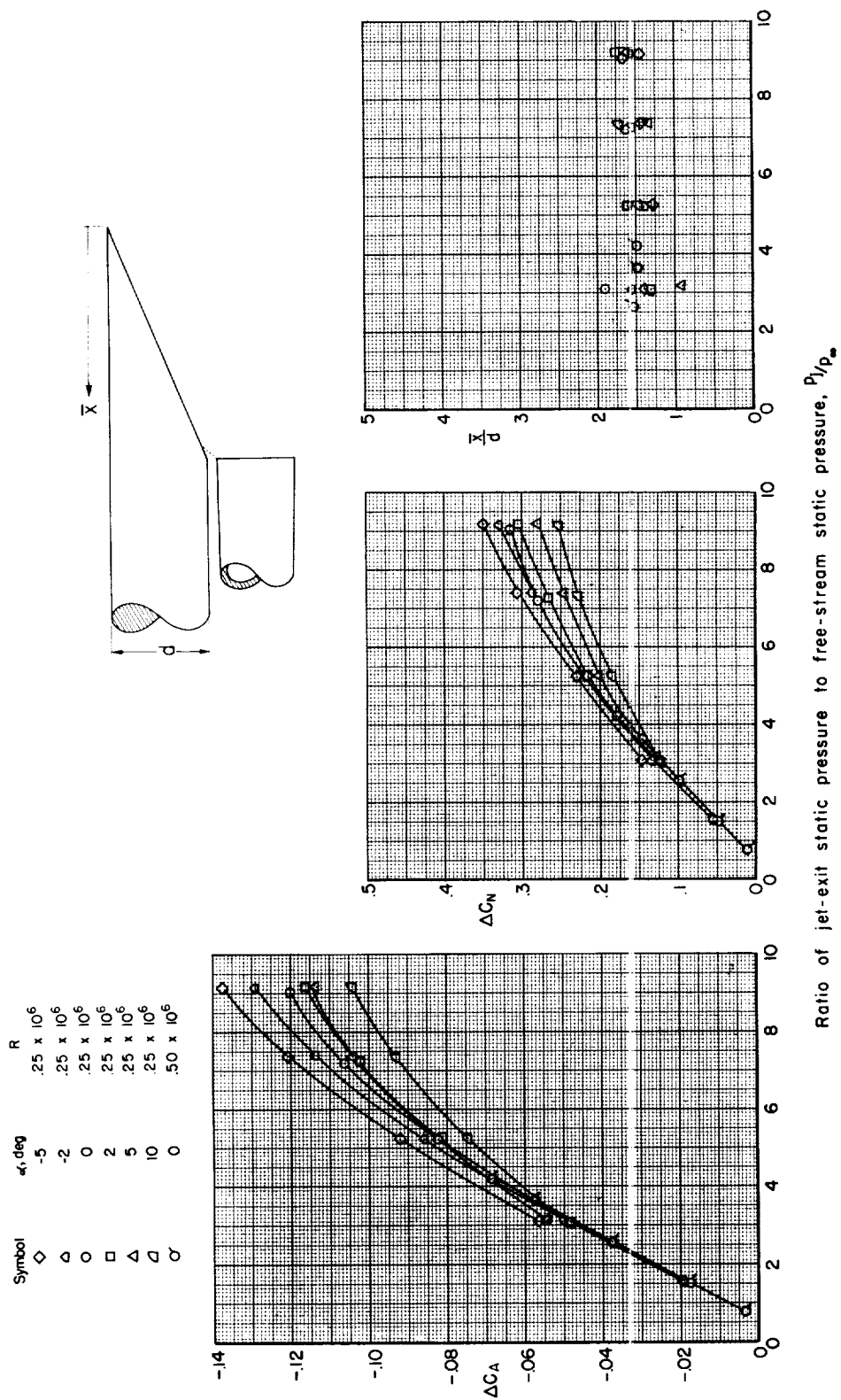
| Symbol | α_1 , deg | R |
|-------------|------------------|-------------------|
| \diamond | -5 | $.25 \times 10^6$ |
| \triangle | -2 | $.25 \times 10^6$ |
| \circ | 0 | $.25 \times 10^6$ |
| \square | 2 | $.25 \times 10^6$ |
| \triangle | 5 | $.25 \times 10^6$ |
| \triangle | 10 | $.25 \times 10^6$ |
| σ | 0 | $.50 \times 10^6$ |



Ratio of jet-exit static pressure to free-stream static pressure, P_j/P_∞

(f) Body B, $r/d = 0.1$, $x/d = 2.0$.

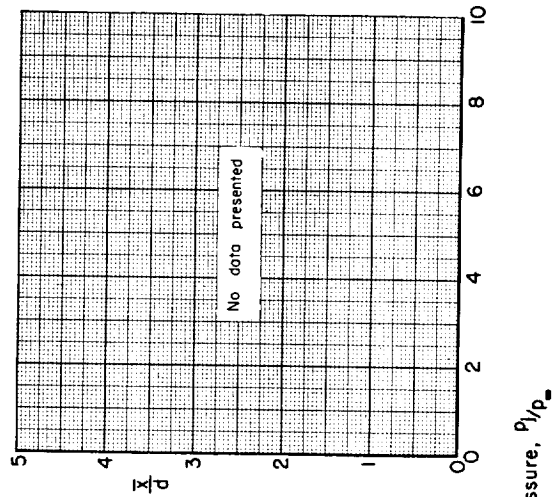
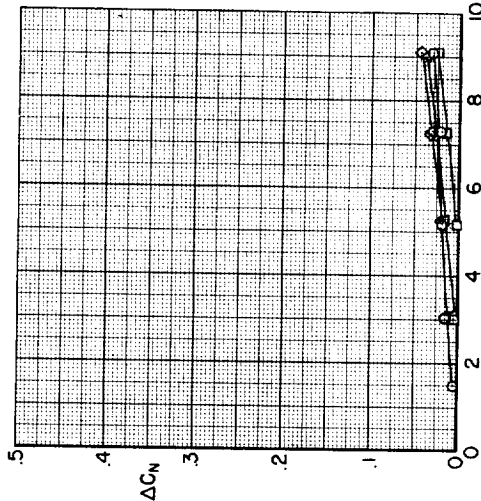
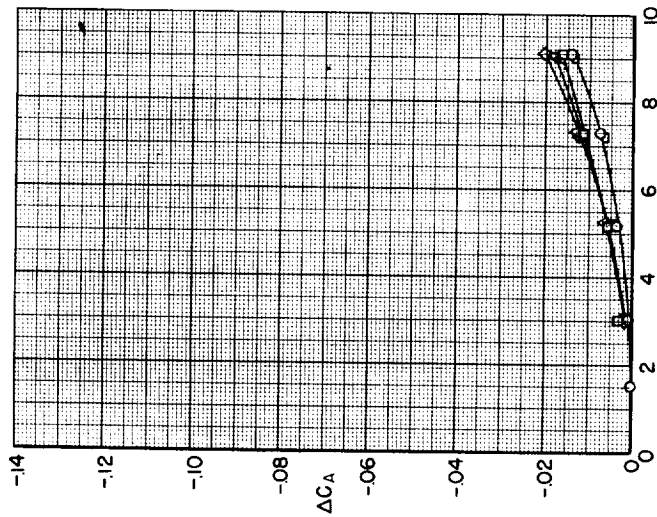
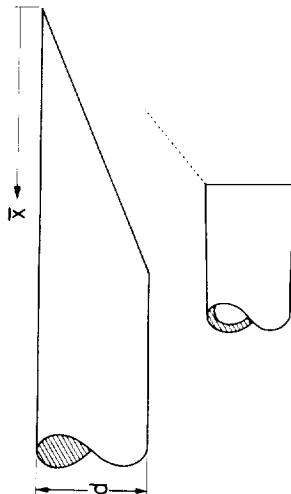
Figure 6.- Continued.



(g) Body B, $r/\bar{a} = 0.1$, $x/\bar{a} = 2.4$.

Figure 6.- Continued.

| Symbol | α_1 , deg | R |
|-------------|------------------|-------------------|
| \diamond | -5 | $.25 \times 10^6$ |
| \triangle | -2 | $.25 \times 10^6$ |
| \circ | 0 | $.25 \times 10^6$ |
| \square | 2 | $.25 \times 10^6$ |
| \triangle | 5 | $.25 \times 10^6$ |
| ∇ | 10 | $.25 \times 10^6$ |



Ratio of jet-exit static pressure to free-stream static pressure, P/P_∞

(h) Body B, $r/d = 0.5$, $x/d = 1.6$.

Figure 6.- Continued.

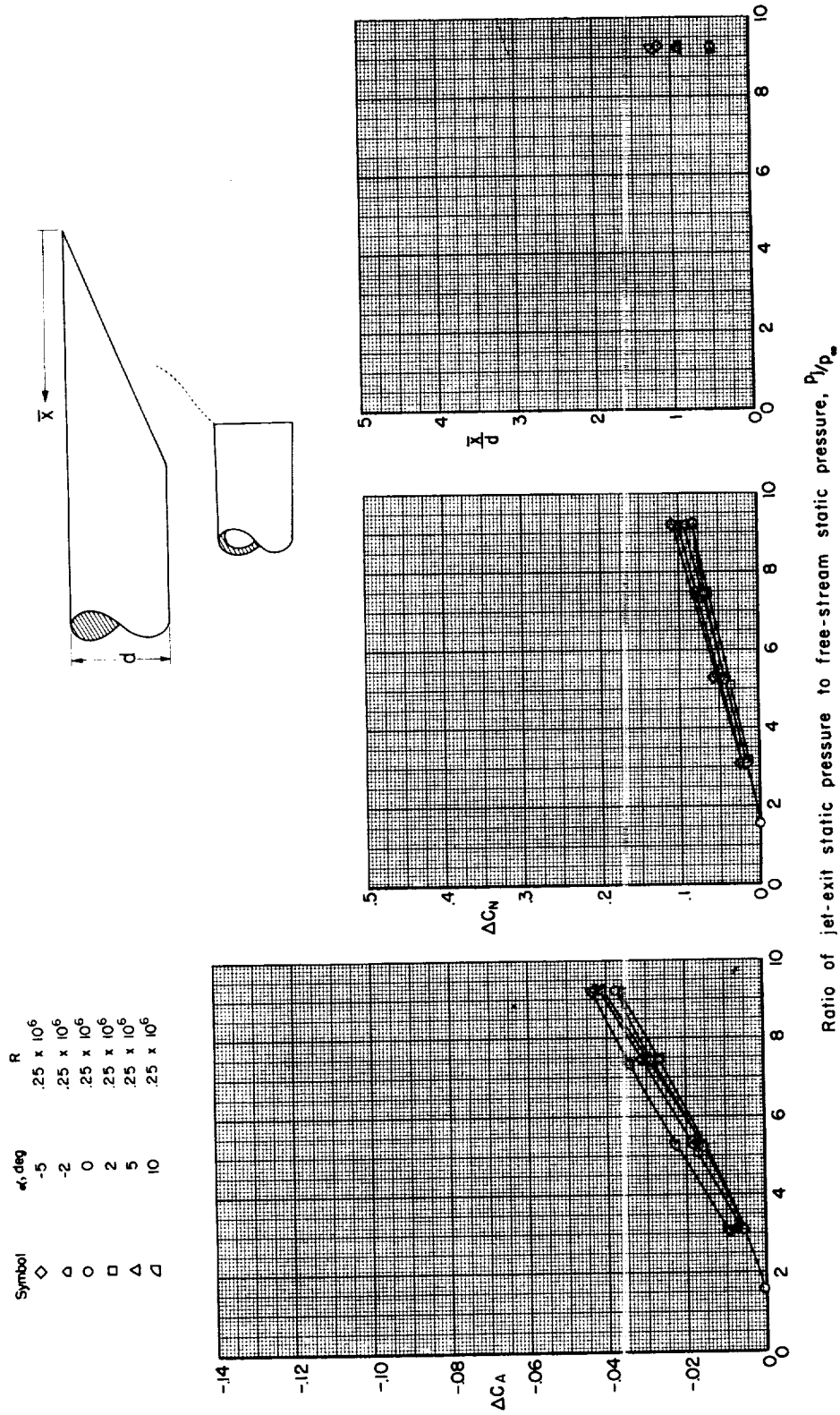
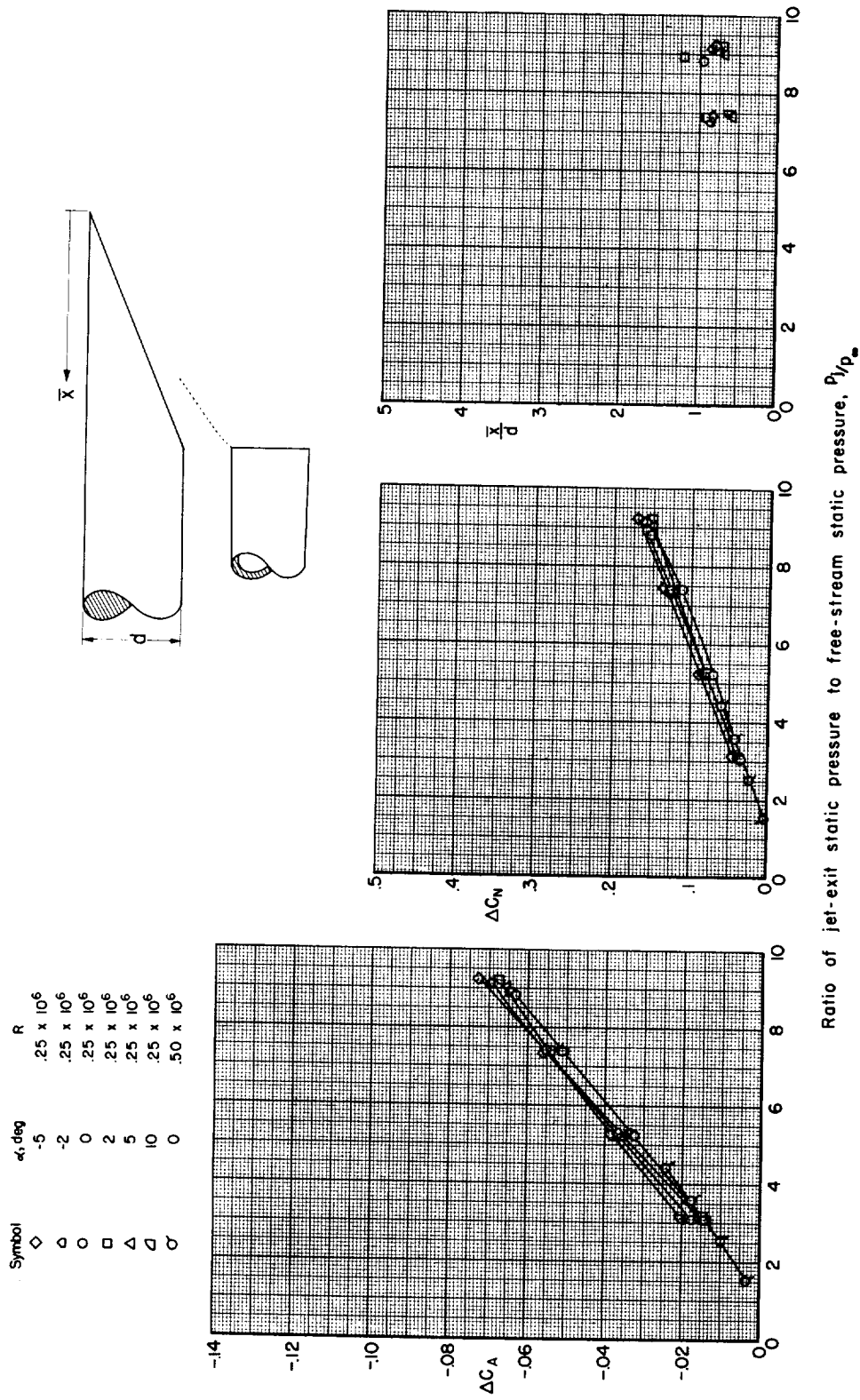


Figure 6.- Continued.



(j) Body B, $r/d = 0.5$, $x/d = 2.4$.

Figure 6.- Continued.

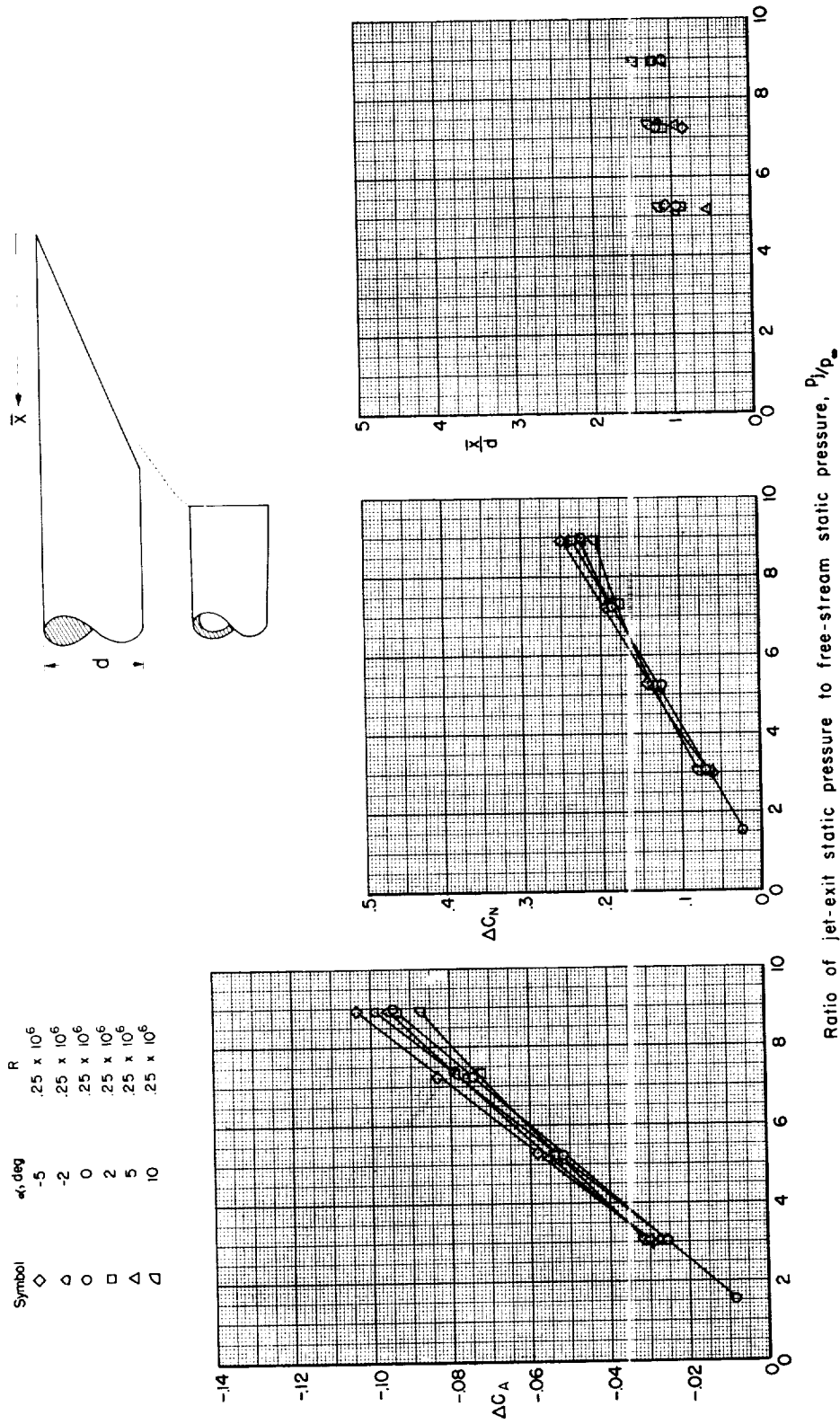
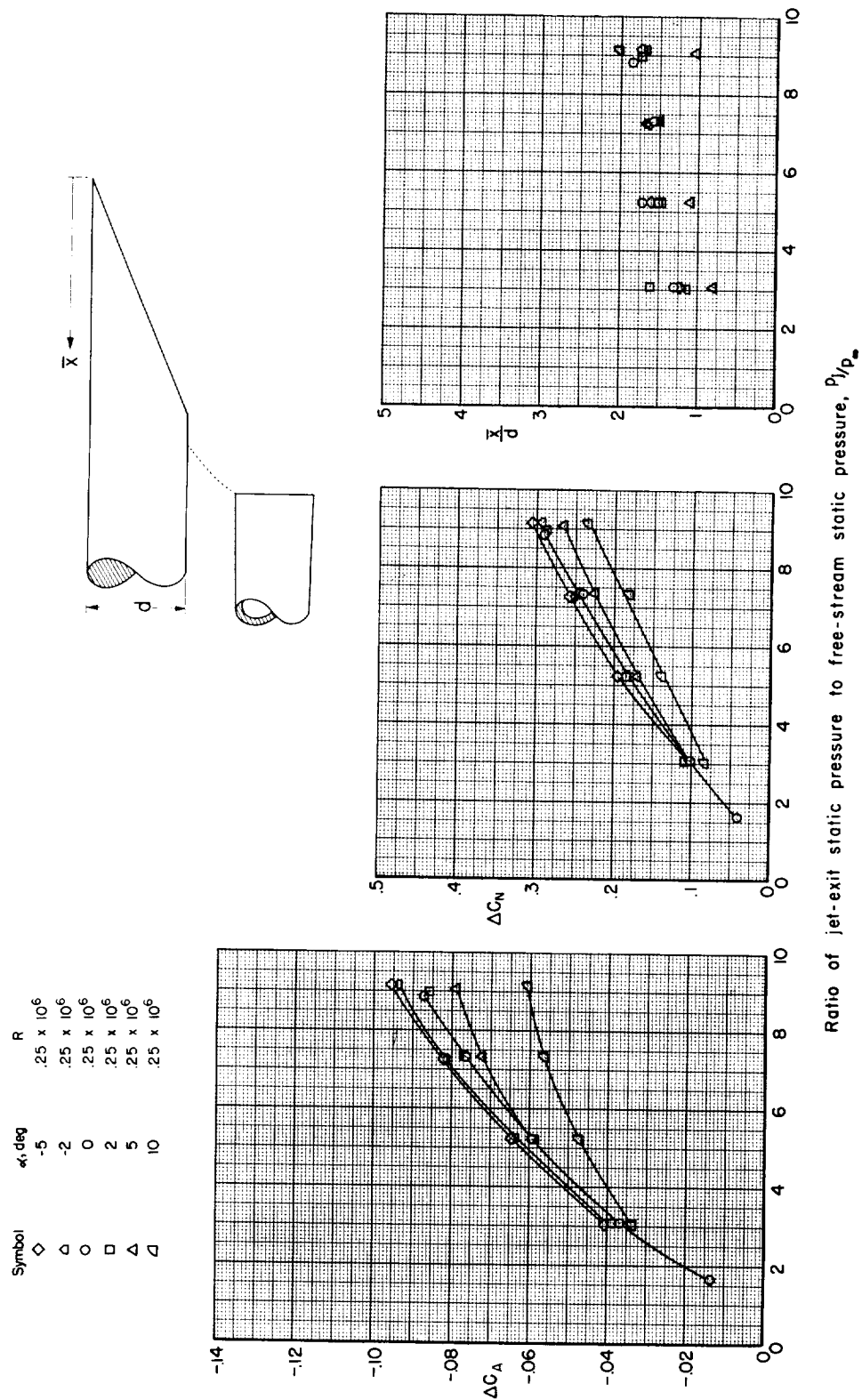


Figure 6.- Continued.



(7) Body B, $r/d = 0.5$, $x/d = 3.2$

Figure 6.- Continued.

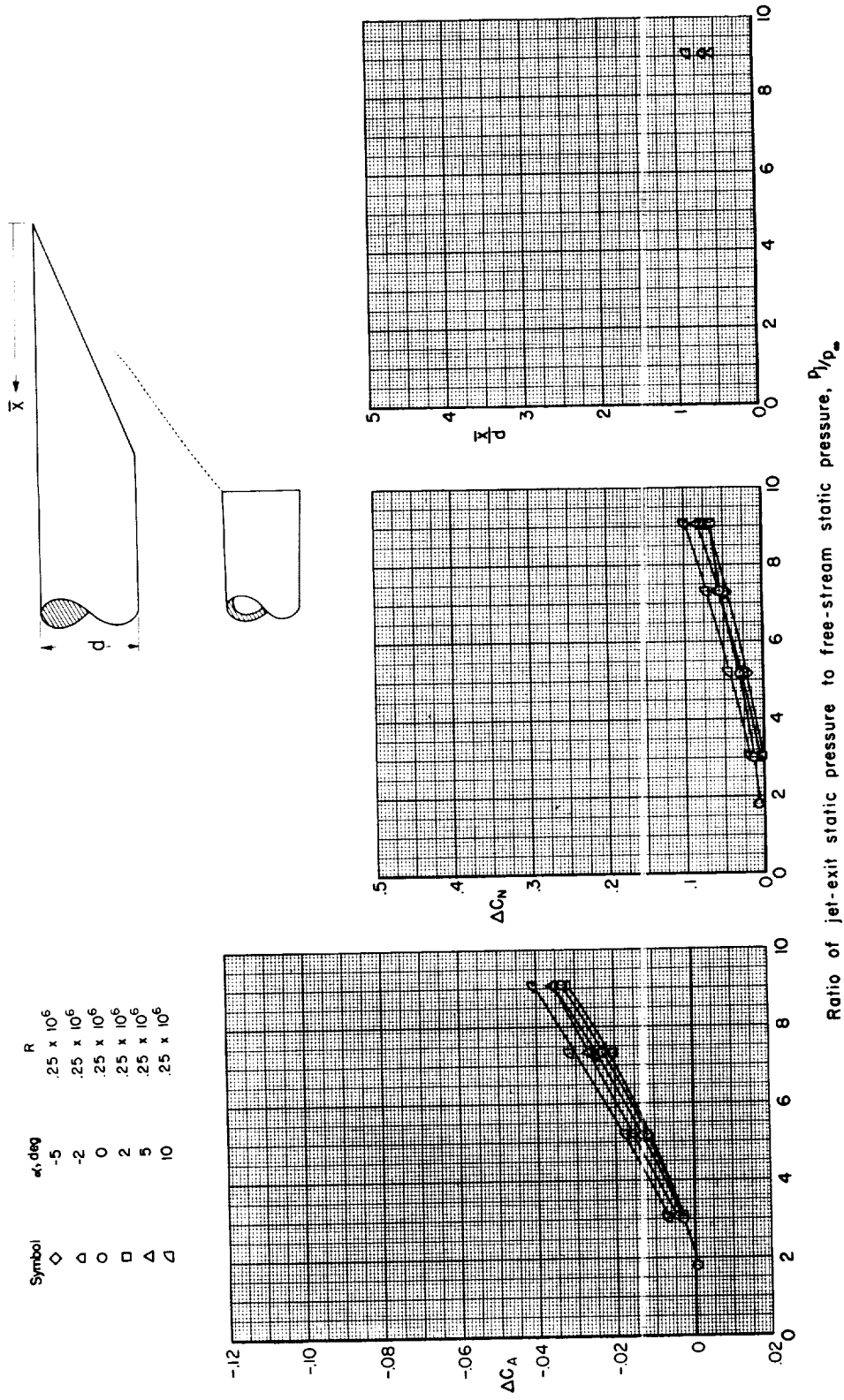
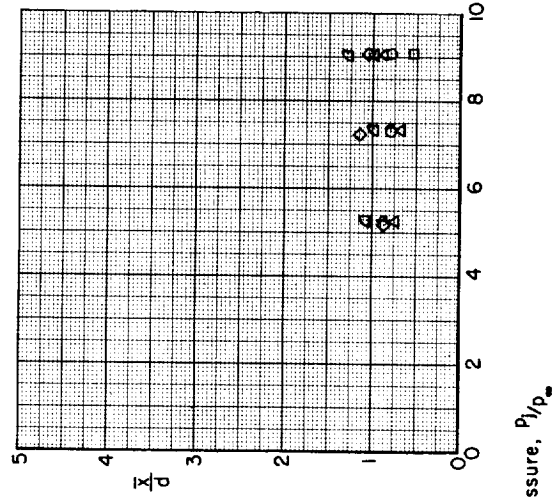
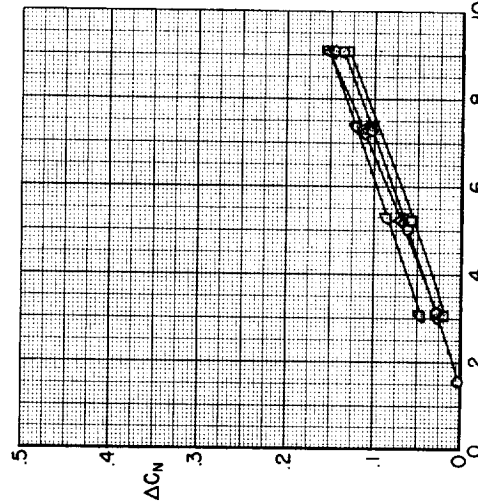
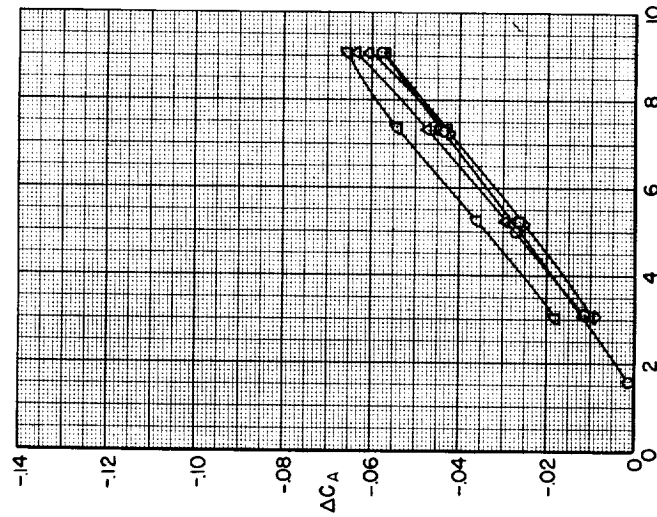
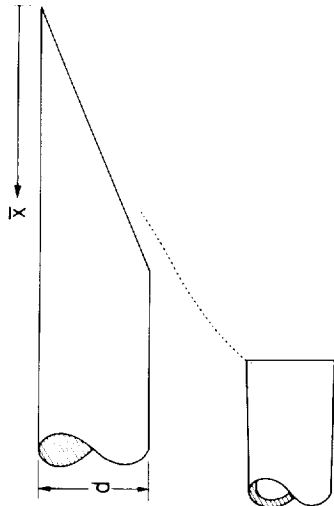


Figure 6.- Continued.

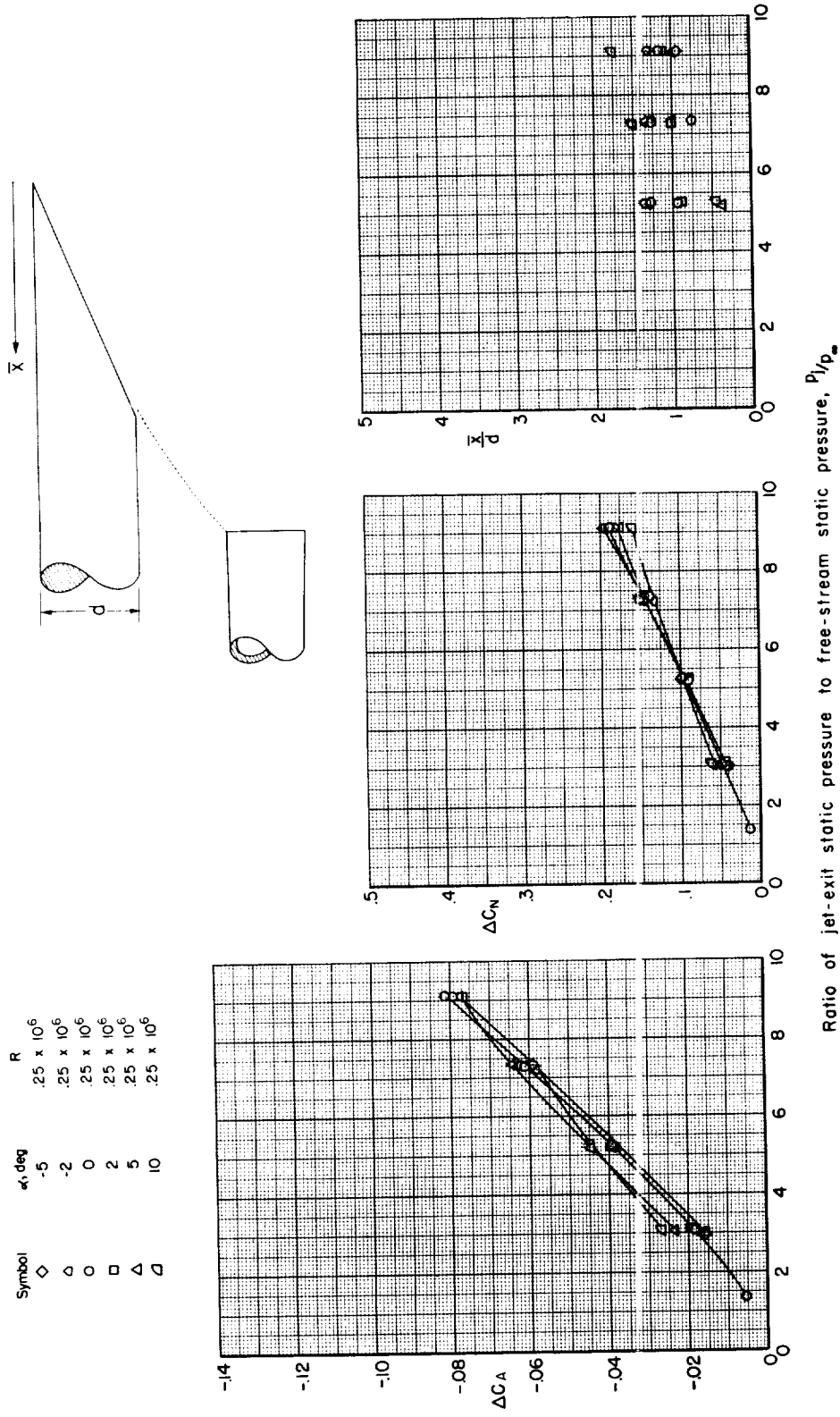
| Symbol | α_1 , deg | R |
|-------------|------------------|-------------------|
| \diamond | -5 | $.25 \times 10^6$ |
| \triangle | -2 | $.25 \times 10^6$ |
| \circ | 0 | $.25 \times 10^6$ |
| \square | 2 | $.25 \times 10^6$ |
| \triangle | 5 | $.25 \times 10^6$ |
| ∇ | 10 | $.25 \times 10^6$ |



Ratio of jet-exit static pressure to free-stream static pressure, P_1/P_∞

(n) Body B, $r/d = 0.9$, $x/d = 3.2$.

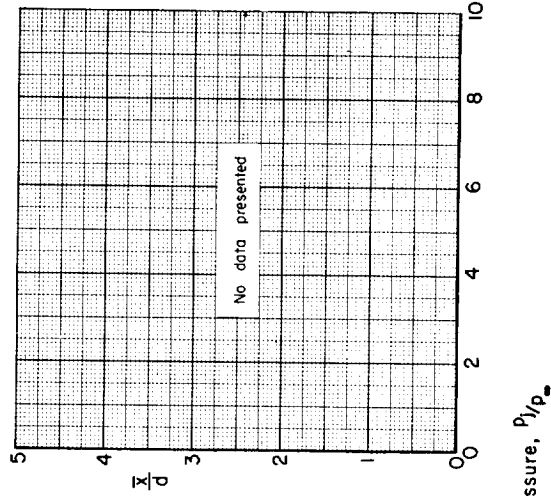
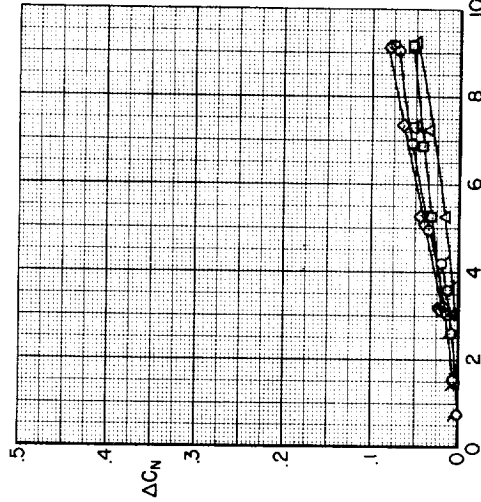
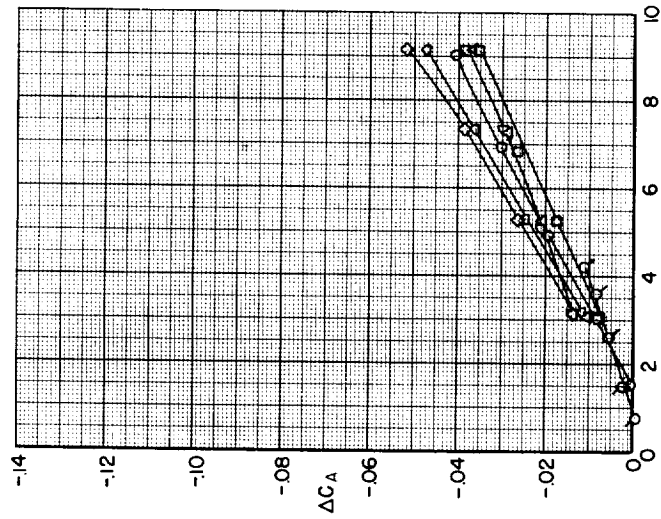
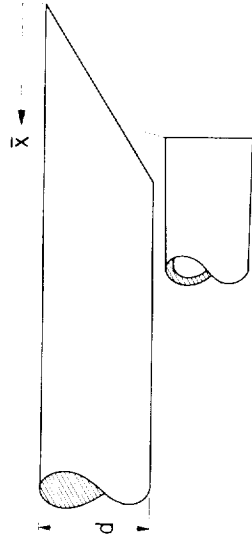
Figure 6.- Continued.



(o) Body B, $r/d = 0.9$, $x/d = 3.6$.

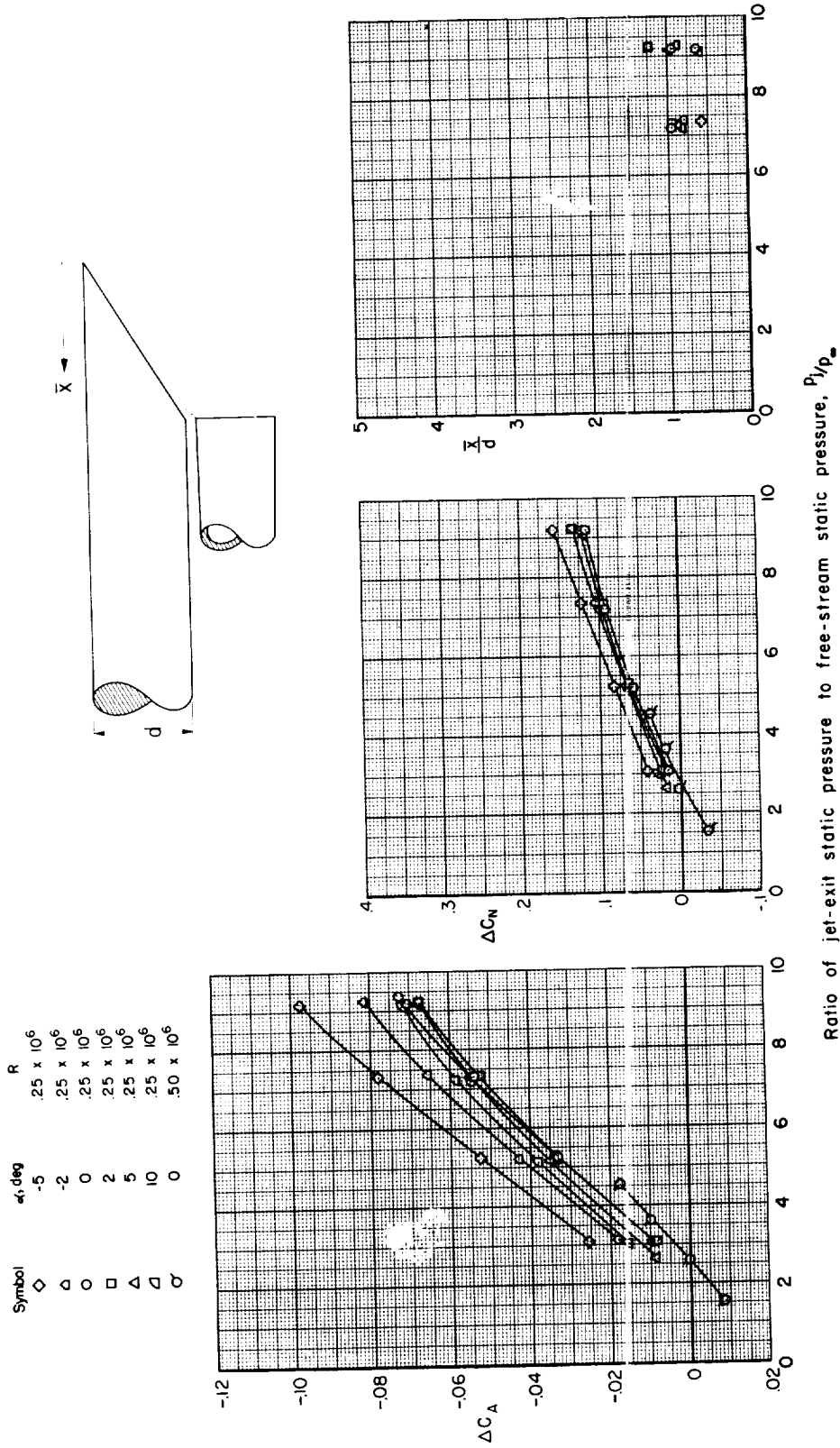
Figure 6.- Continued.

| Symbol | α_i , deg | R |
|-------------|------------------|-------------------|
| \diamond | -5 | $.25 \times 10^6$ |
| \triangle | -2 | $.25 \times 10^6$ |
| \circ | 0 | $.25 \times 10^6$ |
| \square | 2 | $.25 \times 10^6$ |
| \triangle | 5 | $.25 \times 10^6$ |
| \triangle | 10 | $.25 \times 10^6$ |
| σ | 0 | $.50 \times 10^6$ |



(p) Body C, $r/d = 0.1$, $x/d = 1.2$.

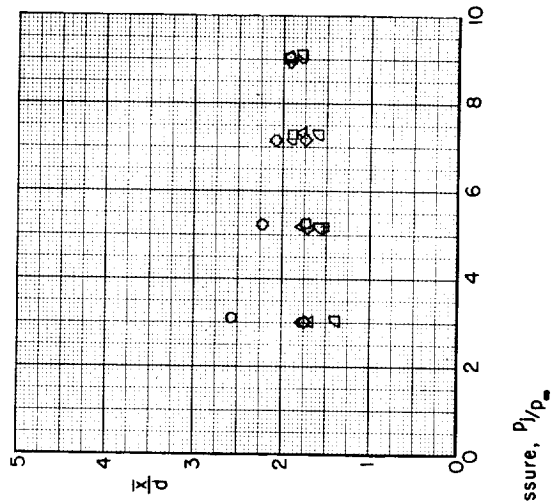
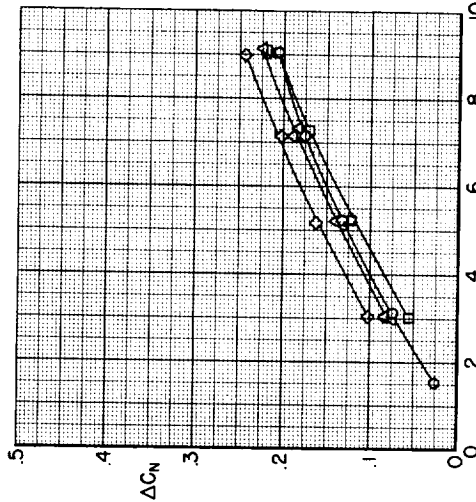
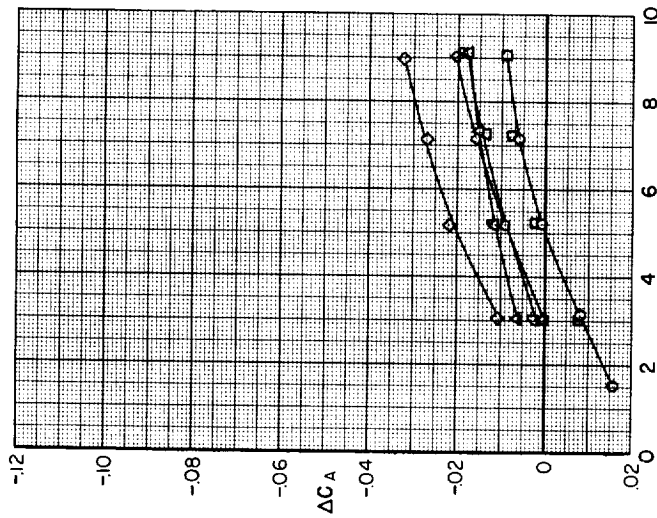
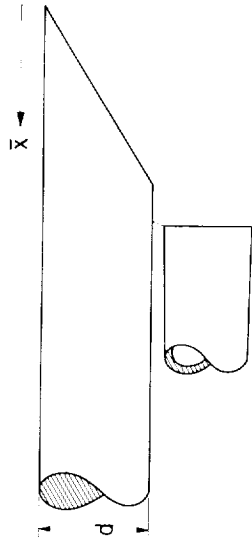
Figure 6.- Continued.



(q) Body C, $r/d = 0.1$, $x/d = 1.6$.

Figure 6.- Continued.

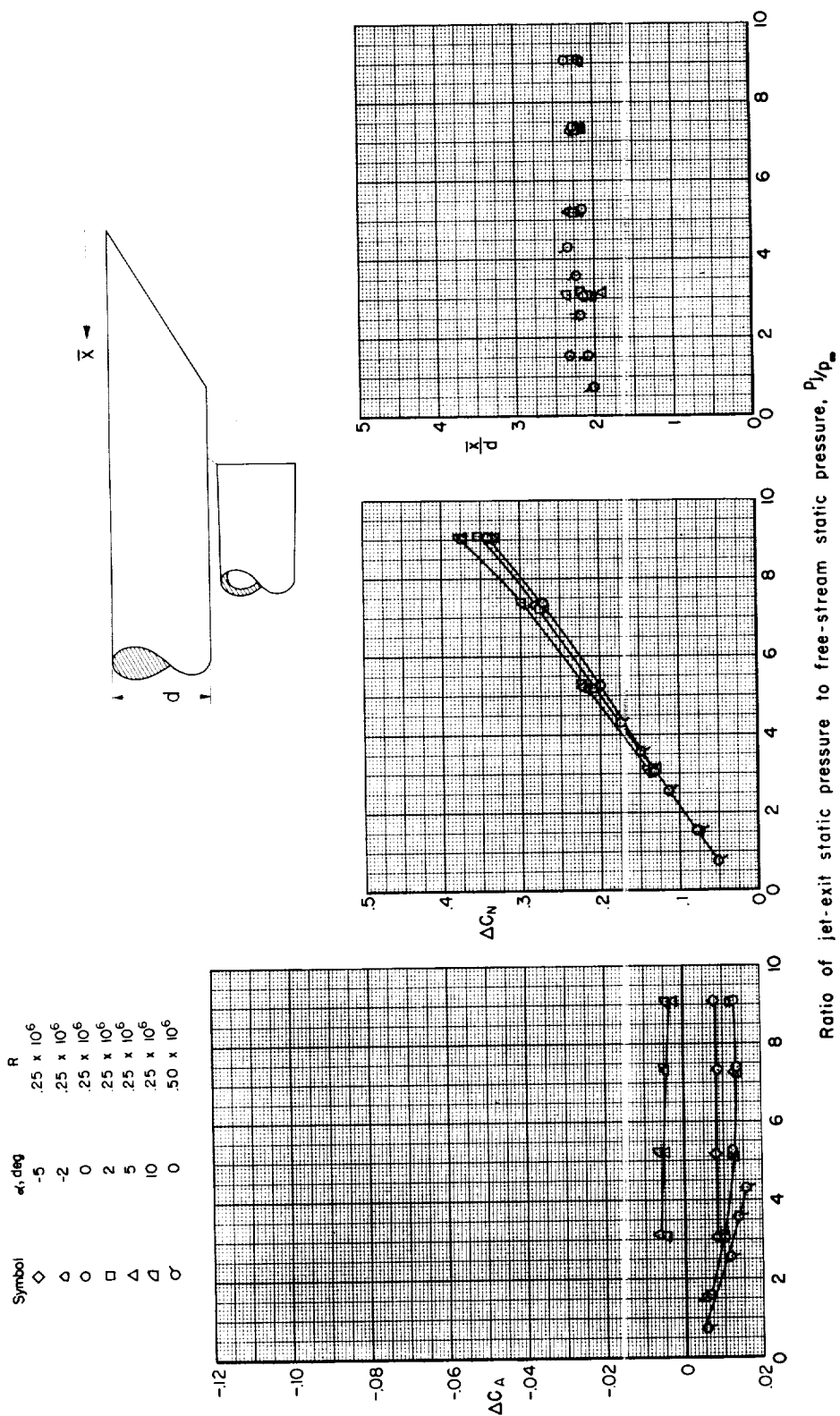
| Symbol | α , deg | R |
|-------------|----------------|-------------------|
| \diamond | -5 | $.25 \times 10^6$ |
| \triangle | -2 | $.25 \times 10^6$ |
| \circ | 0 | $.25 \times 10^6$ |
| \square | 2 | $.25 \times 10^6$ |
| \triangle | 5 | $.25 \times 10^6$ |
| ∇ | 10 | $.25 \times 10^6$ |



Ratio of jet-exit static pressure to free-stream static pressure, P_j/P_∞

(r) Body C, $r/d = 0.1$, $x/d = 2.0$.

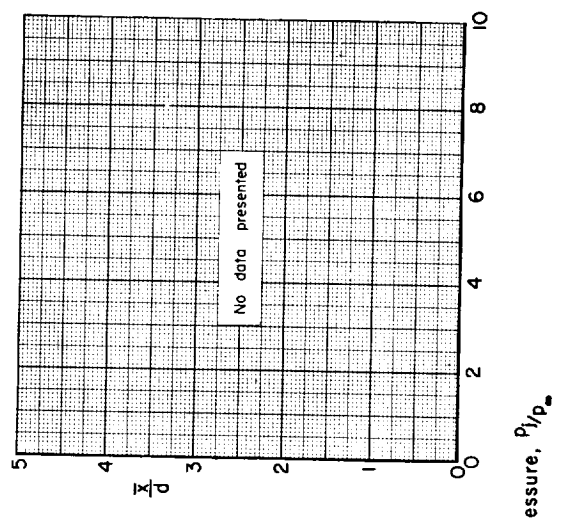
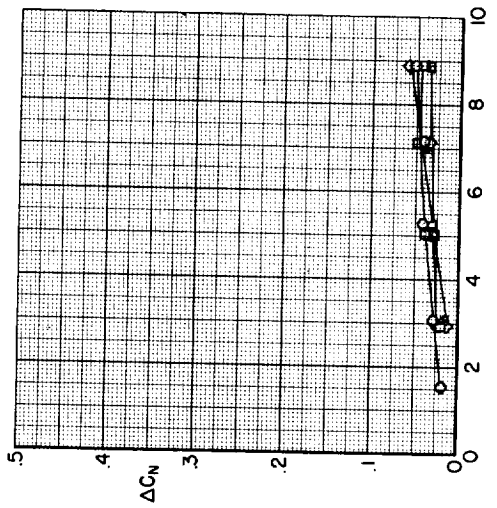
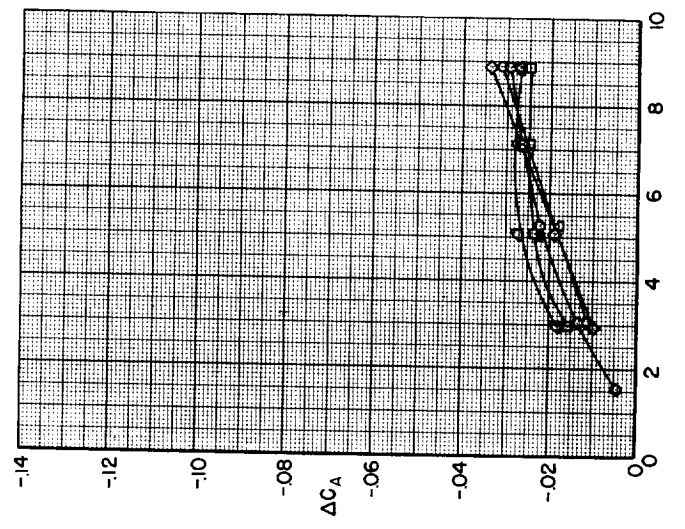
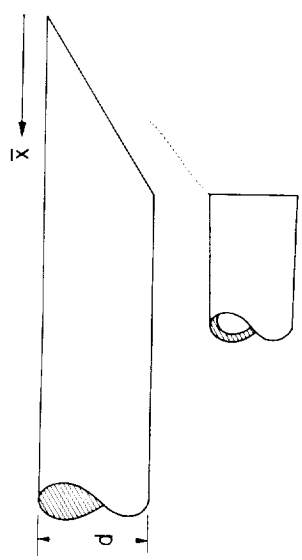
Figure 6.- Continued.



(s) Body C, $r/d = 0.1$, $x/d = 2.4$.

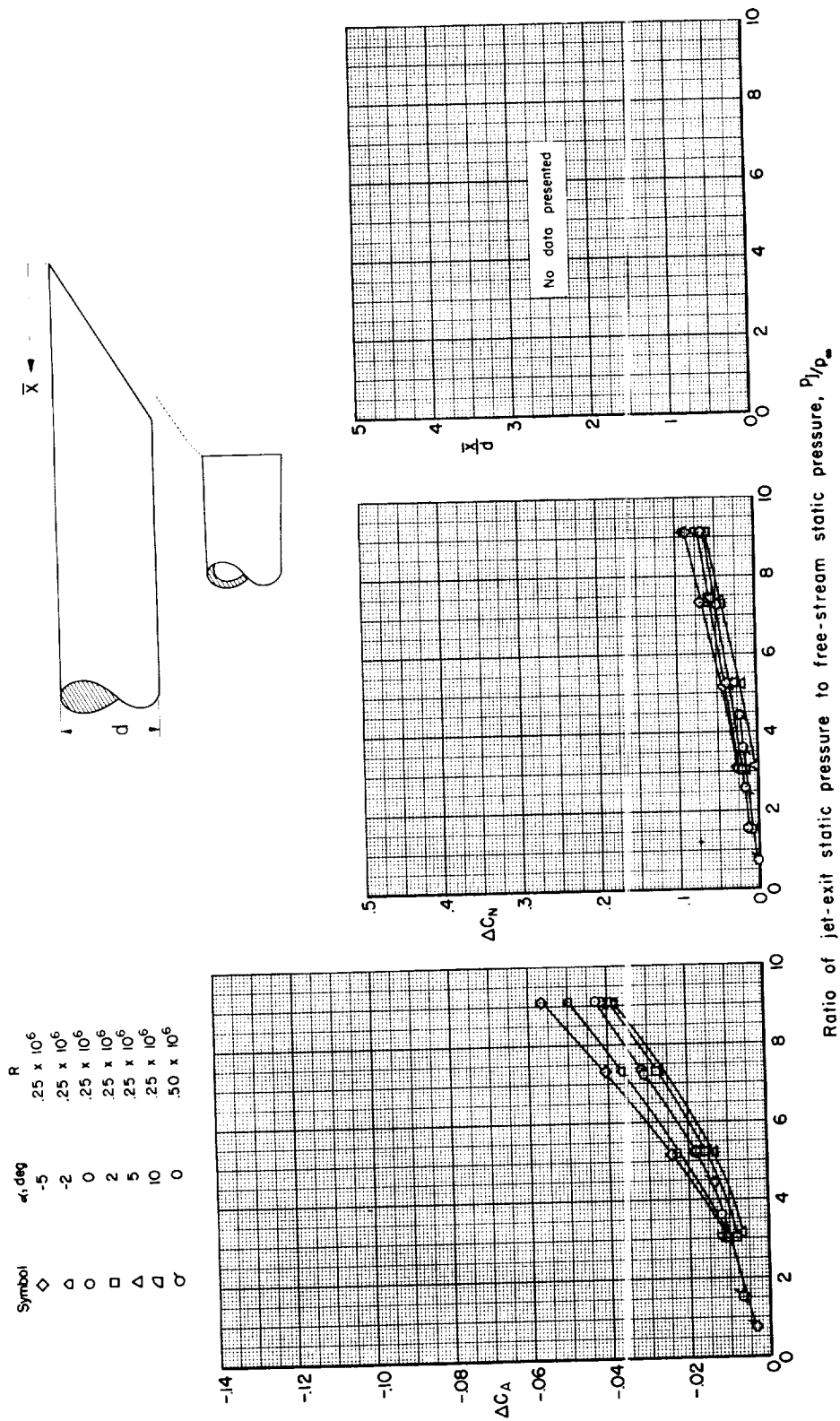
Figure 6.- Continued.

| Symbol | α , deg | R |
|-------------|----------------|-------------------|
| \diamond | -5 | $.25 \times 10^6$ |
| \triangle | -2 | $.25 \times 10^6$ |
| \circ | 0 | $.25 \times 10^6$ |
| \square | 2 | $.25 \times 10^6$ |
| \triangle | 5 | $.25 \times 10^6$ |
| \square | 10 | $.25 \times 10^6$ |



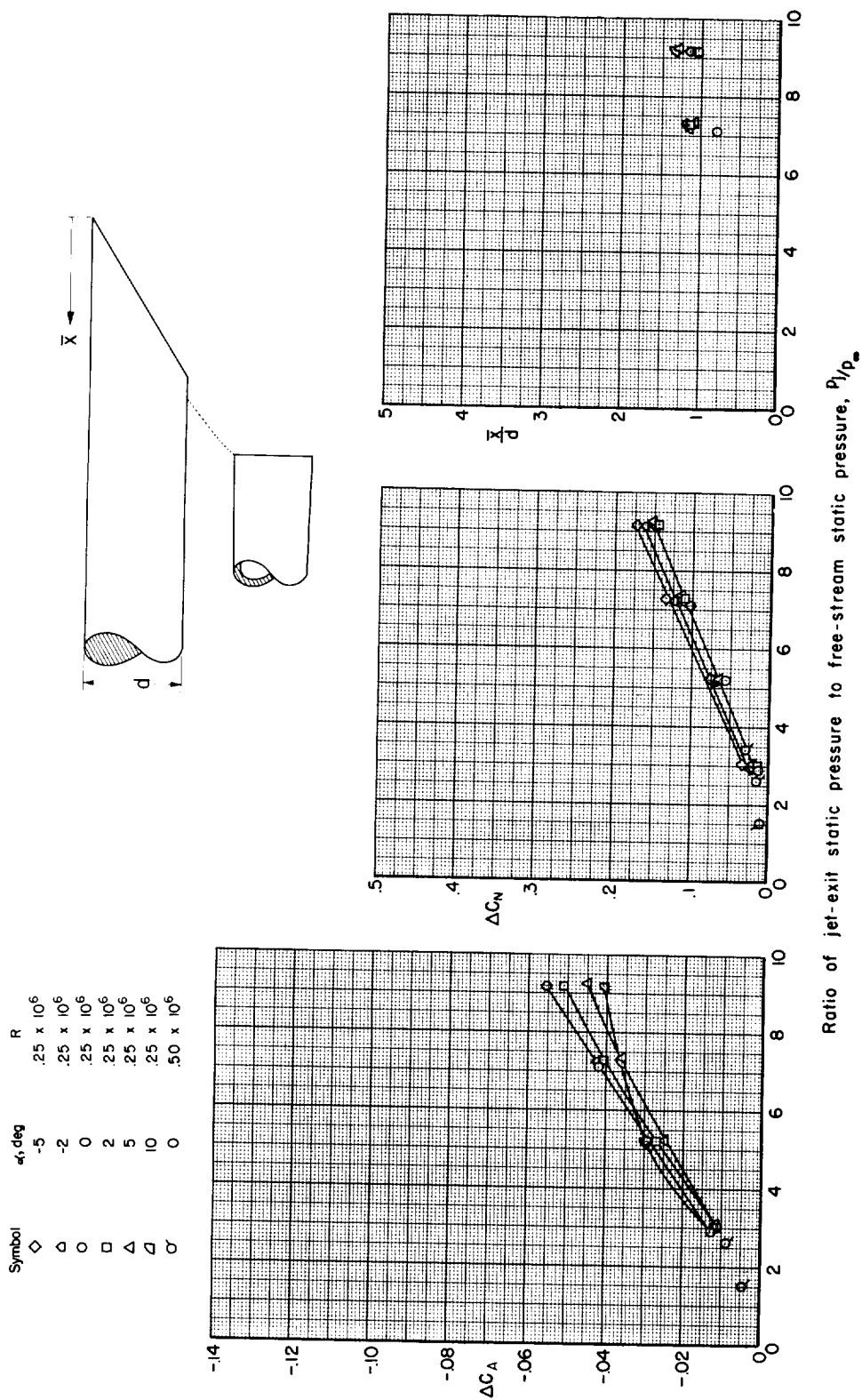
(t) Body C, $r/d = 0.5$, $x/d = 1.6$.

Figure 6.- Continued.



(u) Body C, $r/d = 0.5$, $x/d = 2.0$.

Figure 6.- Continued.



(v) Body C, $r/d = 0.5$, $x/d = 2.4$.

Figure 6.- Continued.

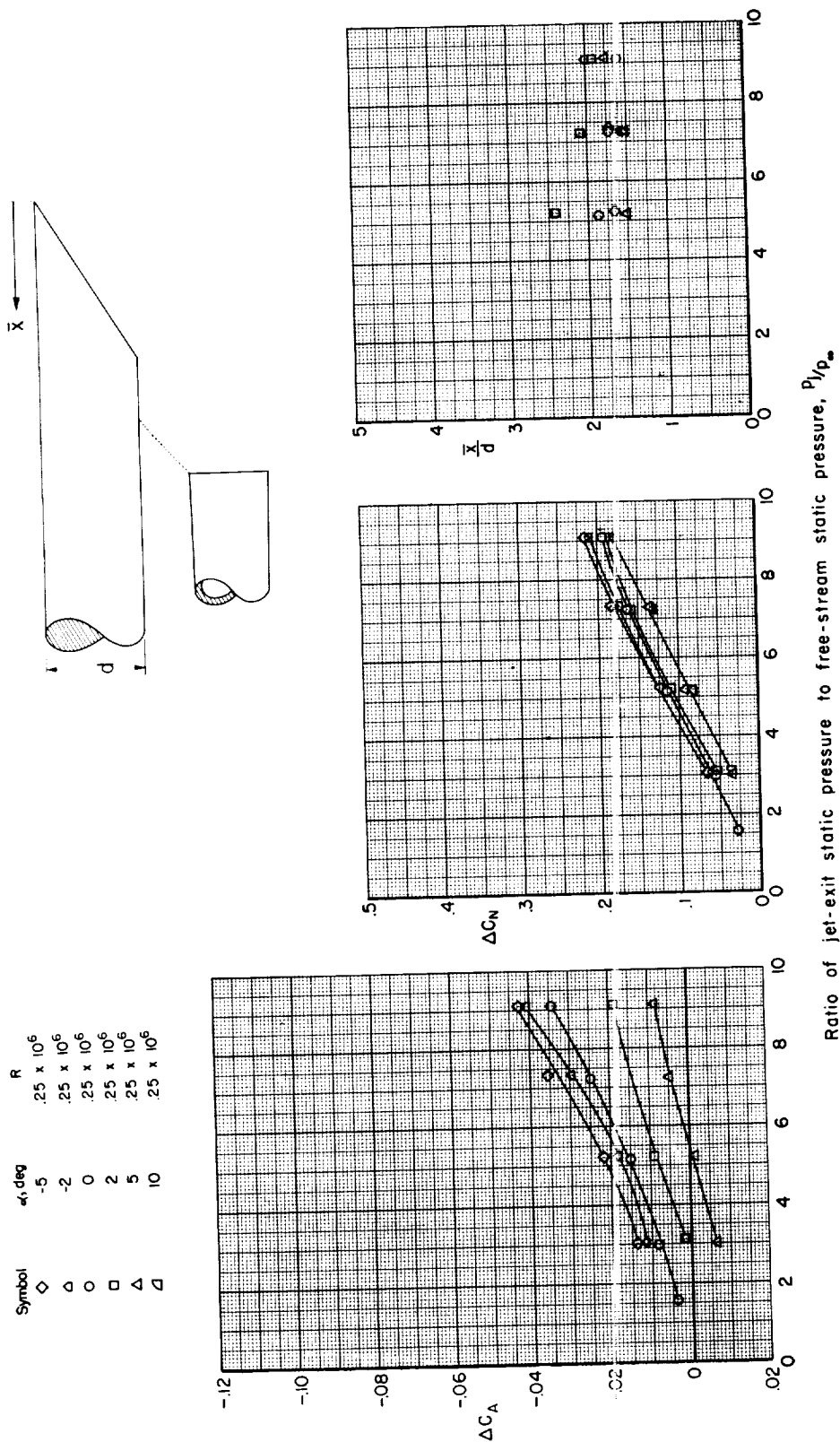
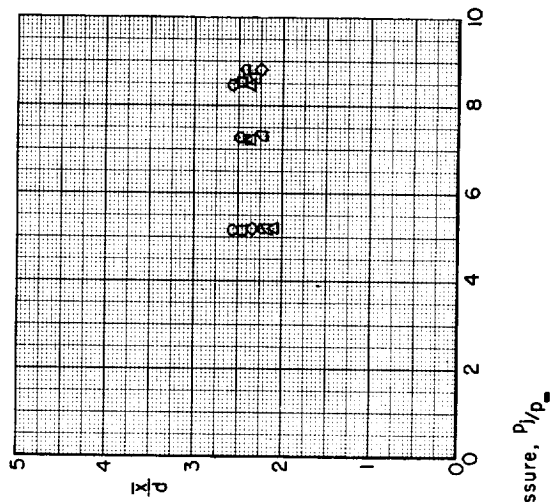
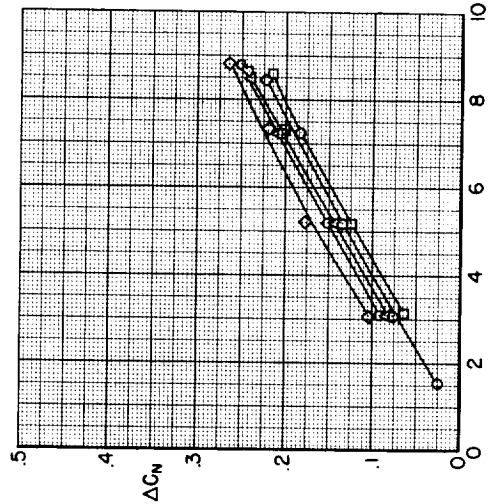
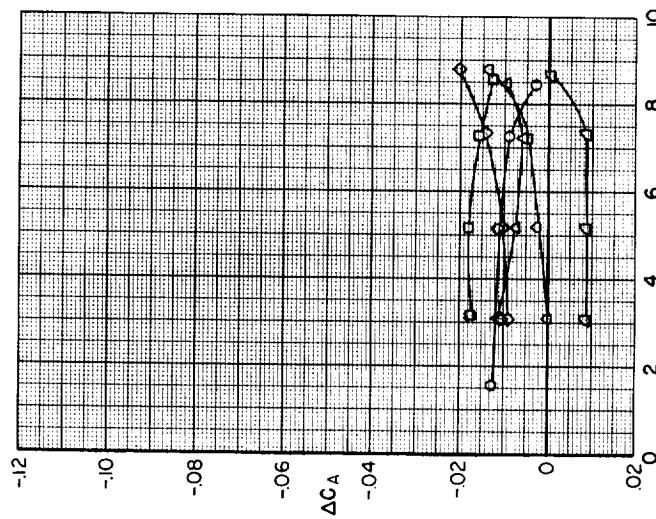
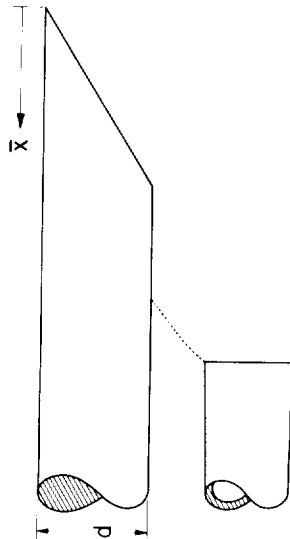


Figure 6.- Continued.

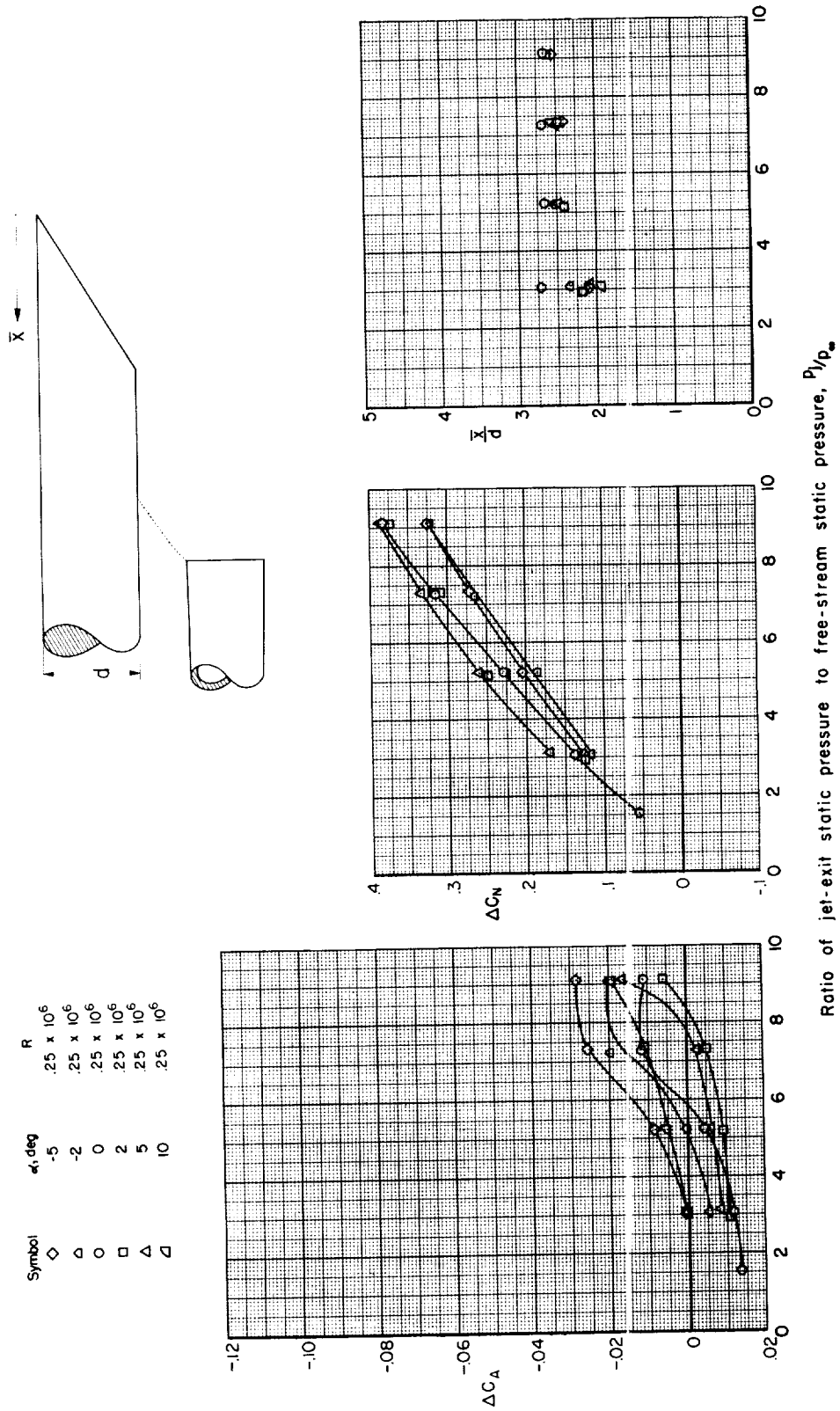
| Symbol | α_1 , deg | R |
|-------------|------------------|-------------------|
| \diamond | -5 | $.25 \times 10^6$ |
| \triangle | -2 | $.25 \times 10^6$ |
| \circ | 0 | $.25 \times 10^6$ |
| \square | 2 | $.25 \times 10^6$ |
| \triangle | 5 | $.25 \times 10^6$ |
| \triangle | 10 | $.25 \times 10^6$ |



Ratio of jet-exit static pressure to free-stream static pressure, P_1/P_∞

(x) Body C, $r/d = 0.5$, $x/d = 3.2$.

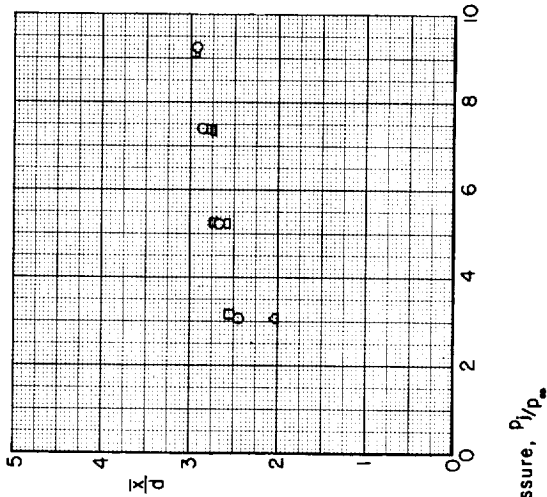
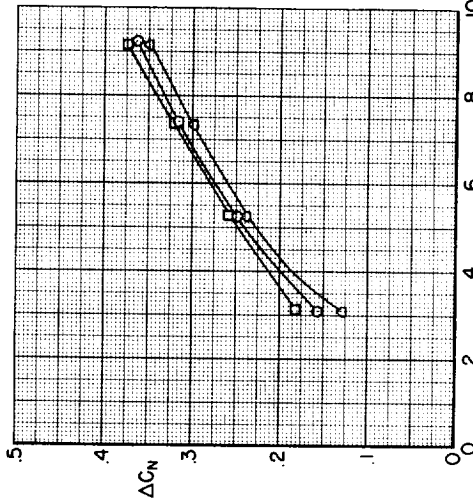
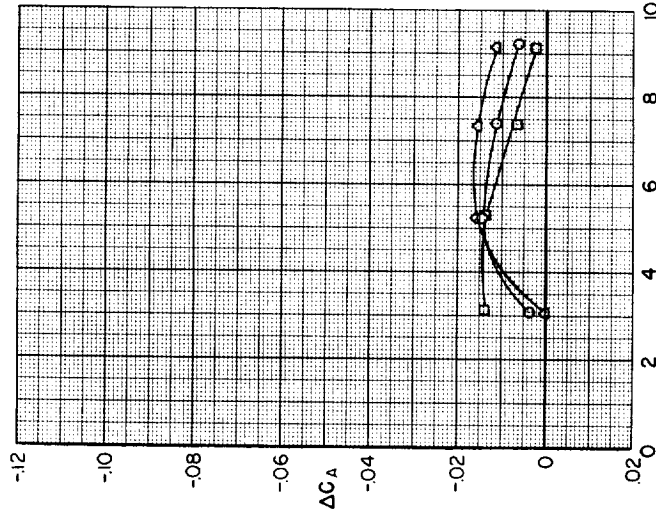
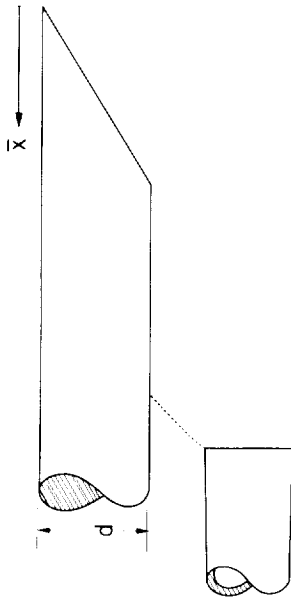
Figure 6.- Continued.



(y) Body C, $r/d = 0.5$, $x/d = 3.6$.

Figure 6.- Continued.

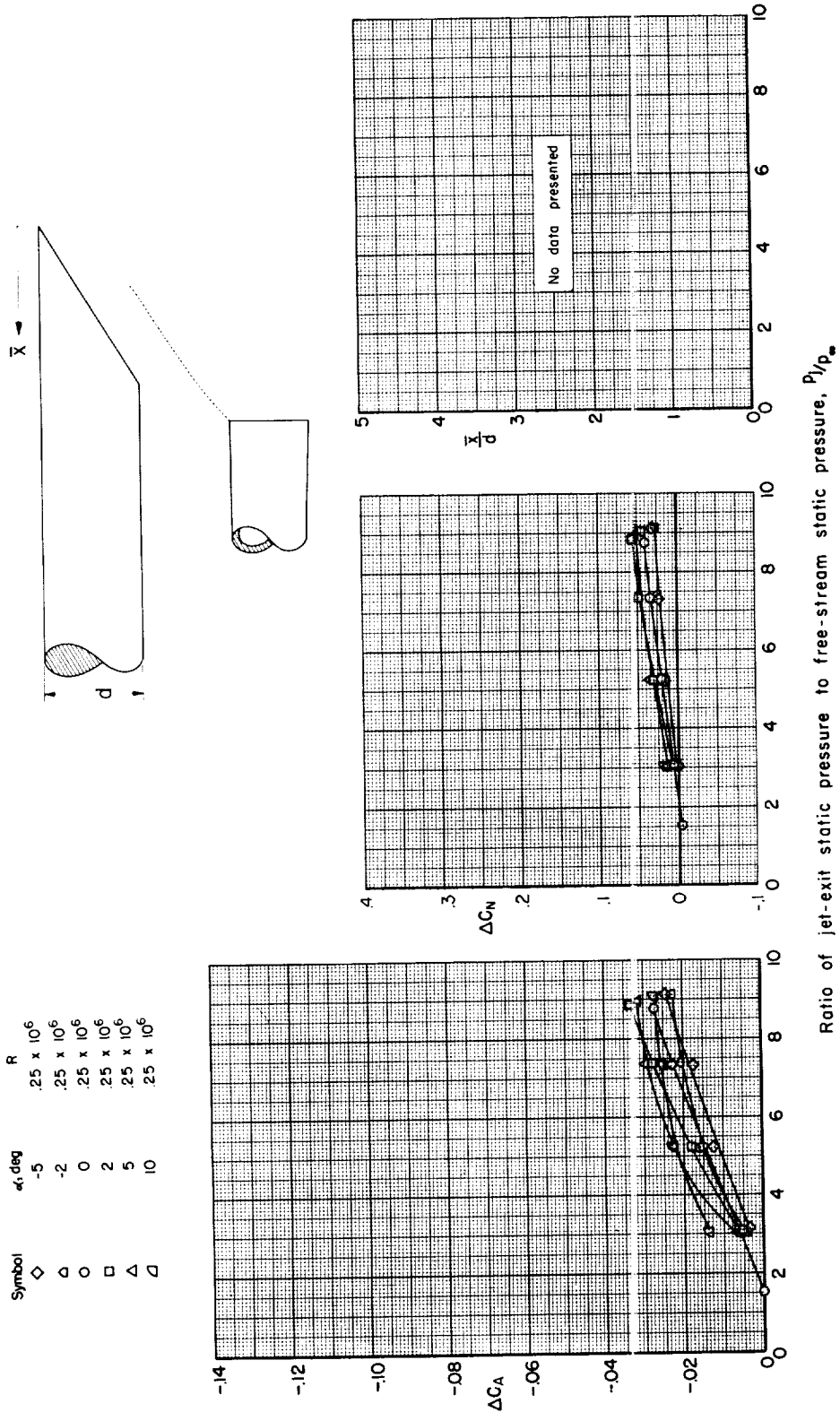
| Symbol | α_1 , deg | R |
|-----------|------------------|-------------------|
| Δ | -2 | $.25 \times 10^6$ |
| \circ | 0 | $.25 \times 10^6$ |
| \square | 2 | $.25 \times 10^6$ |



Ratio of jet-exit static pressure to free-stream static pressure, P/P_∞

(z) Body C, $r/d = 0.5$, $x/d = 4.0$.

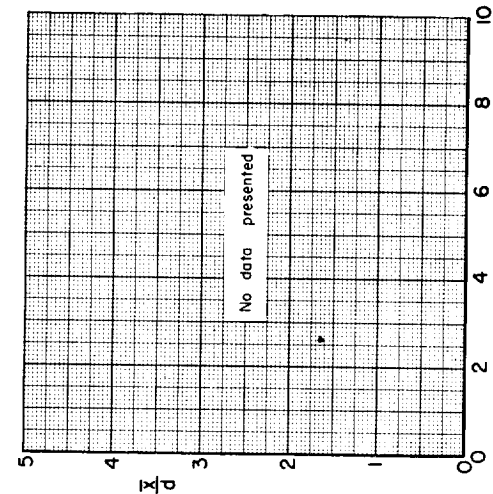
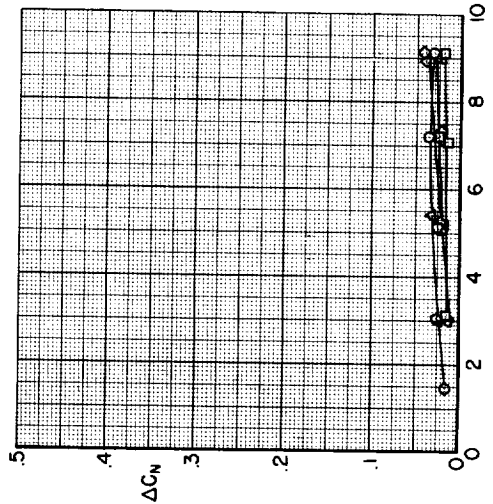
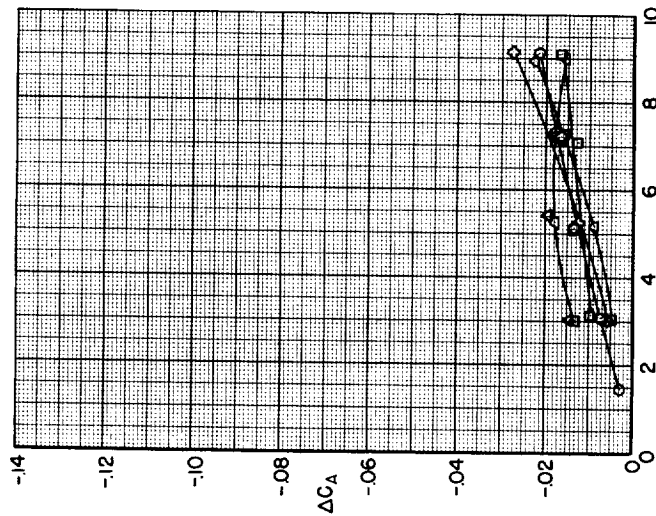
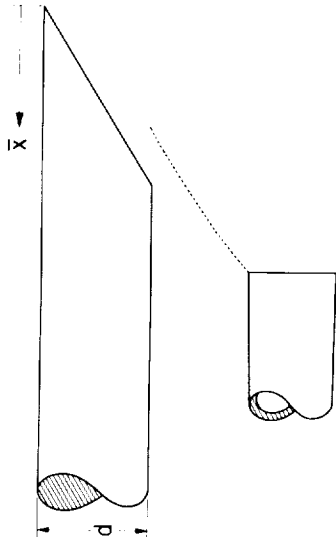
Figure 6.- Continued.



(aa) Body C, $r/d = 0.9$, $x/d = 2.0$.

Figure 6.- Continued.

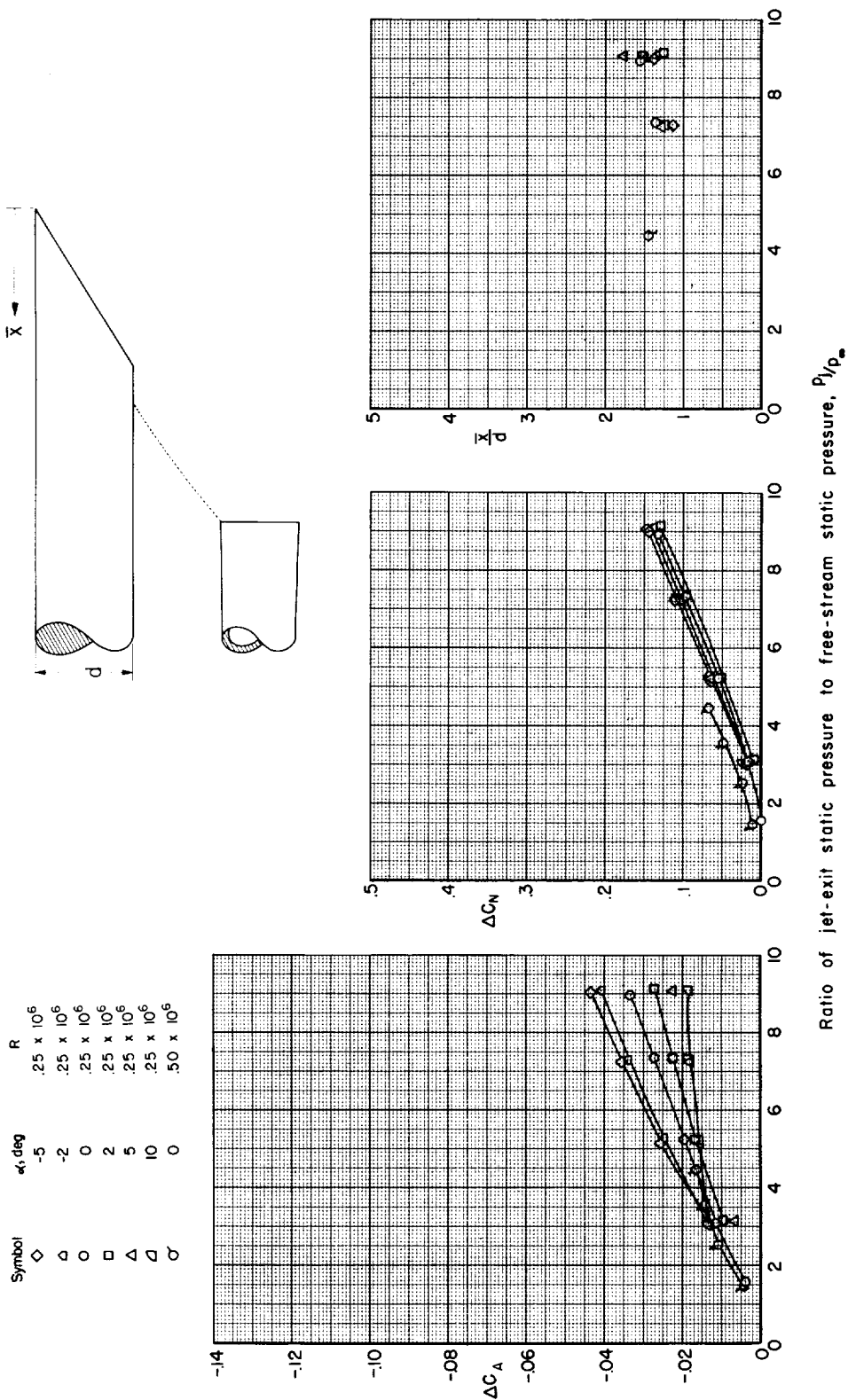
| Symbol | α_1 , deg. | R |
|-------------|-------------------|-------------------|
| \diamond | -5 | $.25 \times 10^6$ |
| \triangle | -2 | $.25 \times 10^6$ |
| \circ | 0 | $.25 \times 10^6$ |
| \square | 2 | $.25 \times 10^6$ |
| \triangle | 5 | $.25 \times 10^6$ |
| ∇ | 10 | $.25 \times 10^6$ |



Ratio of jet-exit static pressure to free-stream static pressure, P_i/P_∞

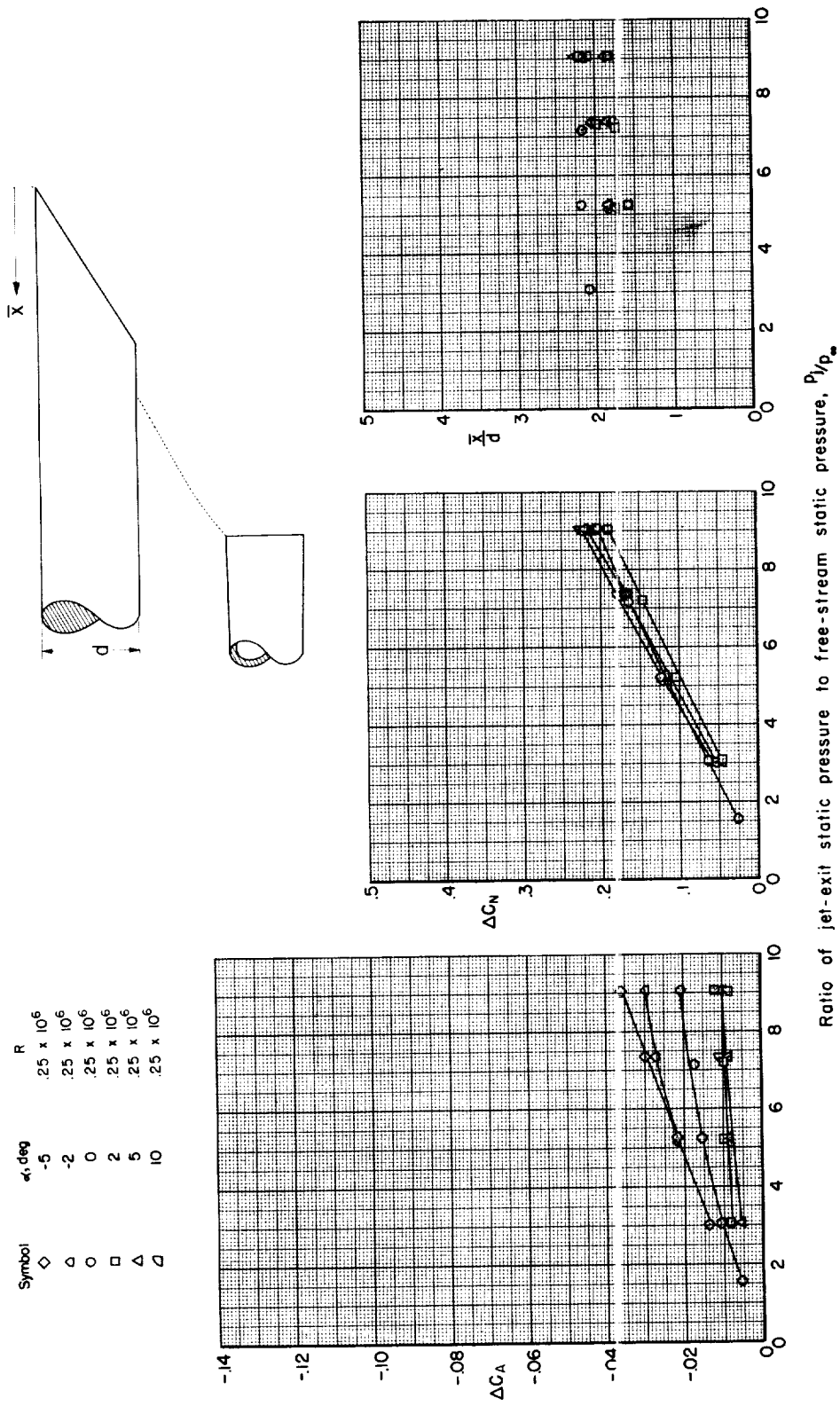
(bb) Body C, $r/\bar{a} = 0.9$, $x/\bar{a} = 2.4$.

Figure 6.- Continued.



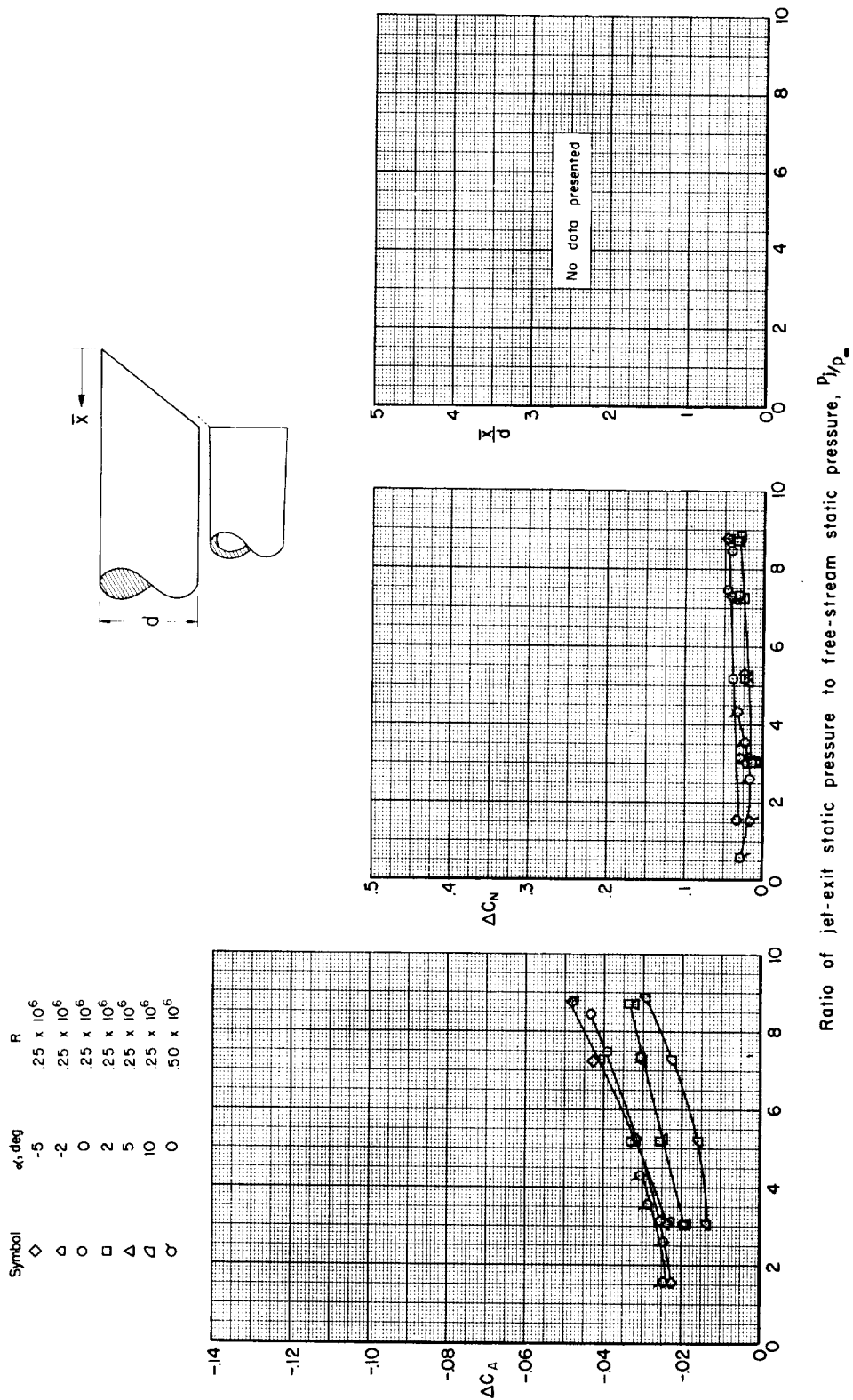
(dd) Body C, $r/d = 0.9$, $x/d = 3.2$.

Figure 6.- Continued.



(ee) Body C, $r/d = 0.9$, $x/d = 3.6$.

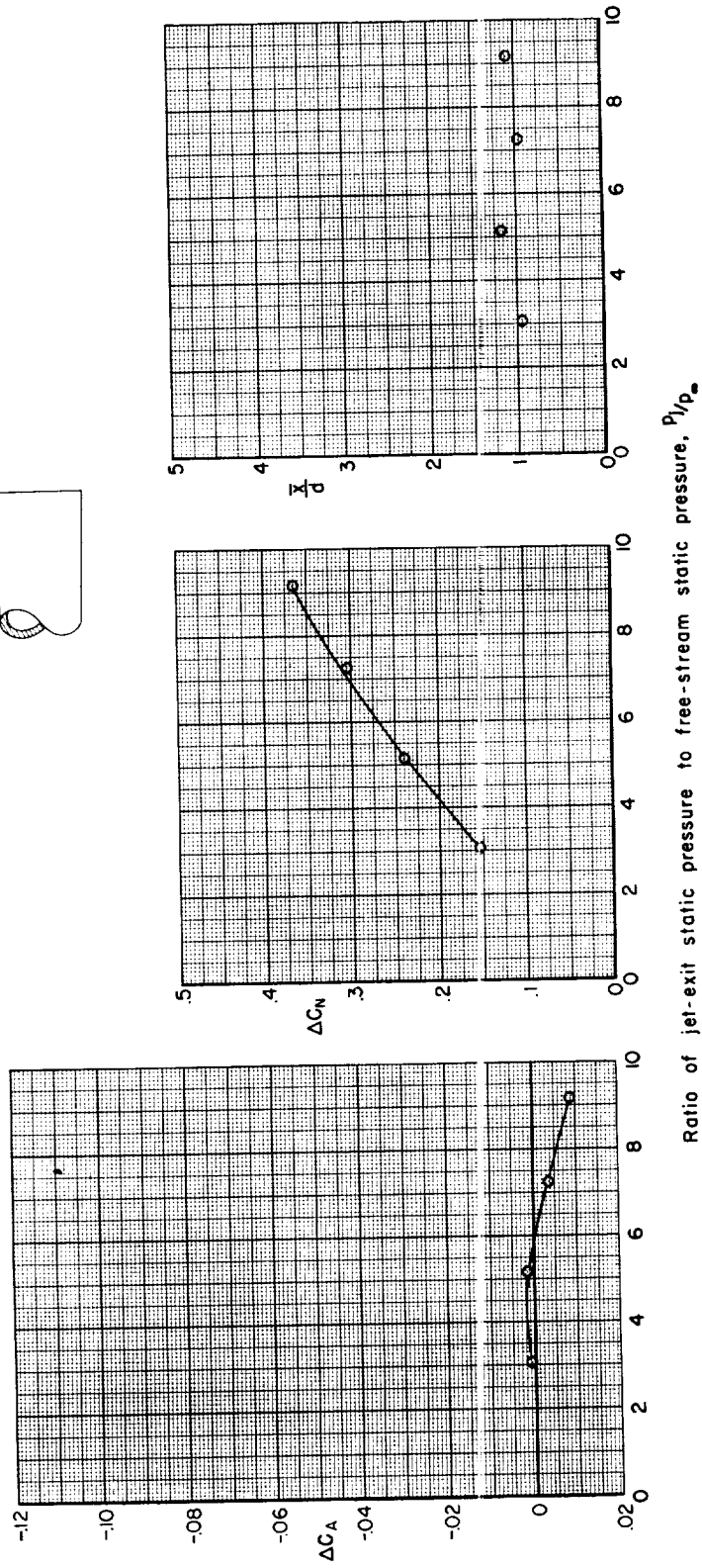
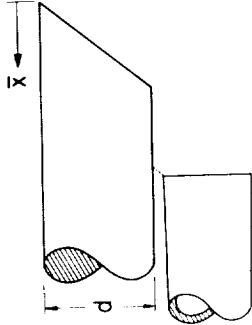
Figure 6.- Continued.



(ff) Body D, $r/d = 0.1$, $x/d = 0.8$.

Figure 6.- Continued.

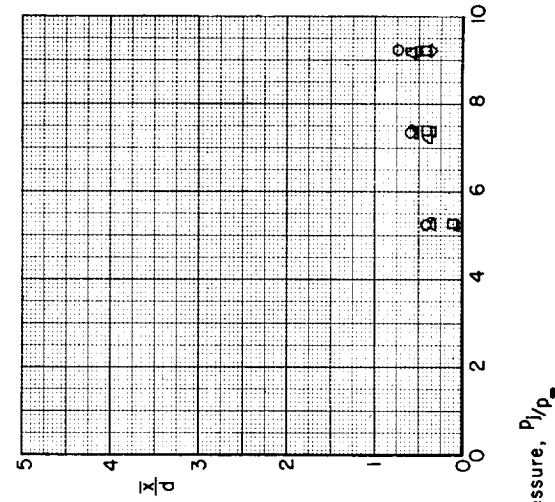
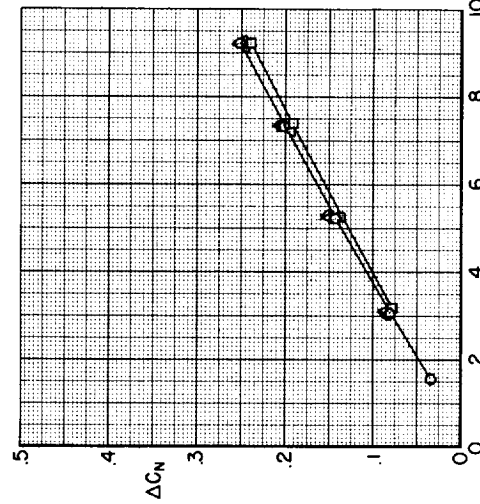
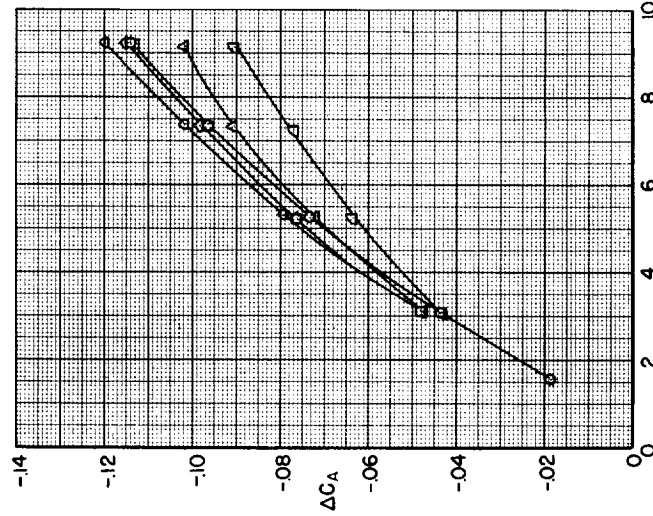
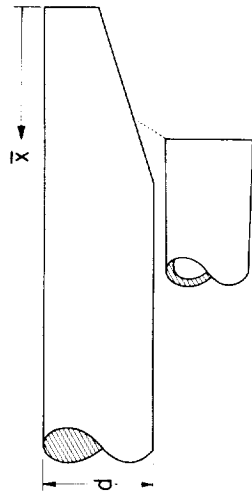
| Symbol | α , deg | R |
|--------|----------------|-------------------|
| O | 0 | $.25 \times 10^6$ |



(gg) Body D, $r/d = 0.1$, $x/d = 1.6$.

Figure 6.- Continued.

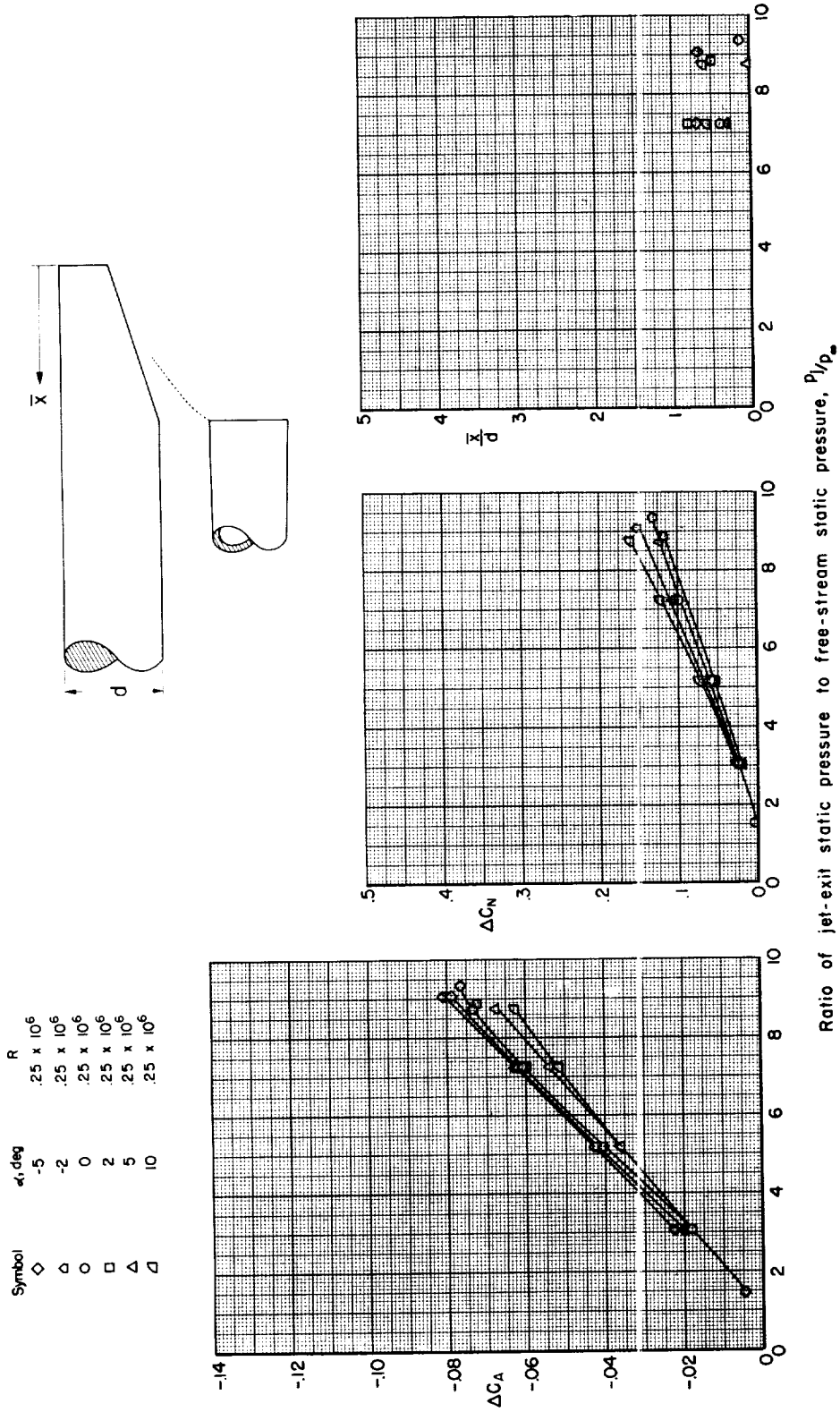
| Symbol | α , deg | R |
|-------------|----------------|-------------------|
| \diamond | -5 | $.25 \times 10^6$ |
| \triangle | -2 | $.25 \times 10^6$ |
| \circ | 0 | $.25 \times 10^6$ |
| \square | 2 | $.25 \times 10^6$ |
| \triangle | 5 | $.25 \times 10^6$ |
| ∇ | 10 | $.25 \times 10^6$ |



Ratio of jet-exit static pressure to free-stream static pressure, P_j/P_∞

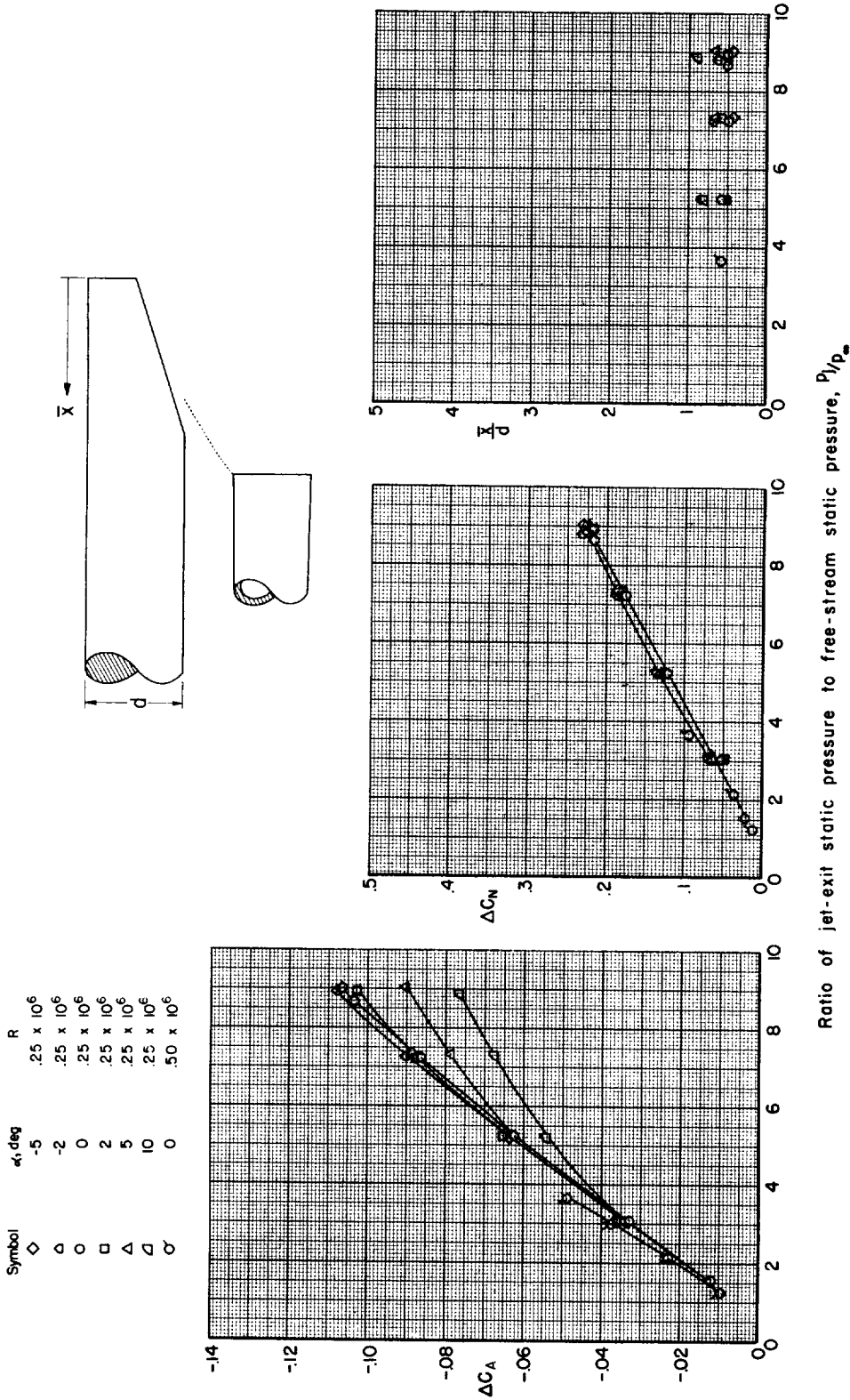
(hh) Body E, $r/d = 0.1$, $x/d = 1.2$.

Figure 6.- Continued.



(ii) Body E, $r/d = 0.5$, $x/d = 1.6$.

Figure 6.- Continued.



(jj) Body E, $r/d = 0.5$, $x/d = 2.0$.

Figure 6.- Continued.

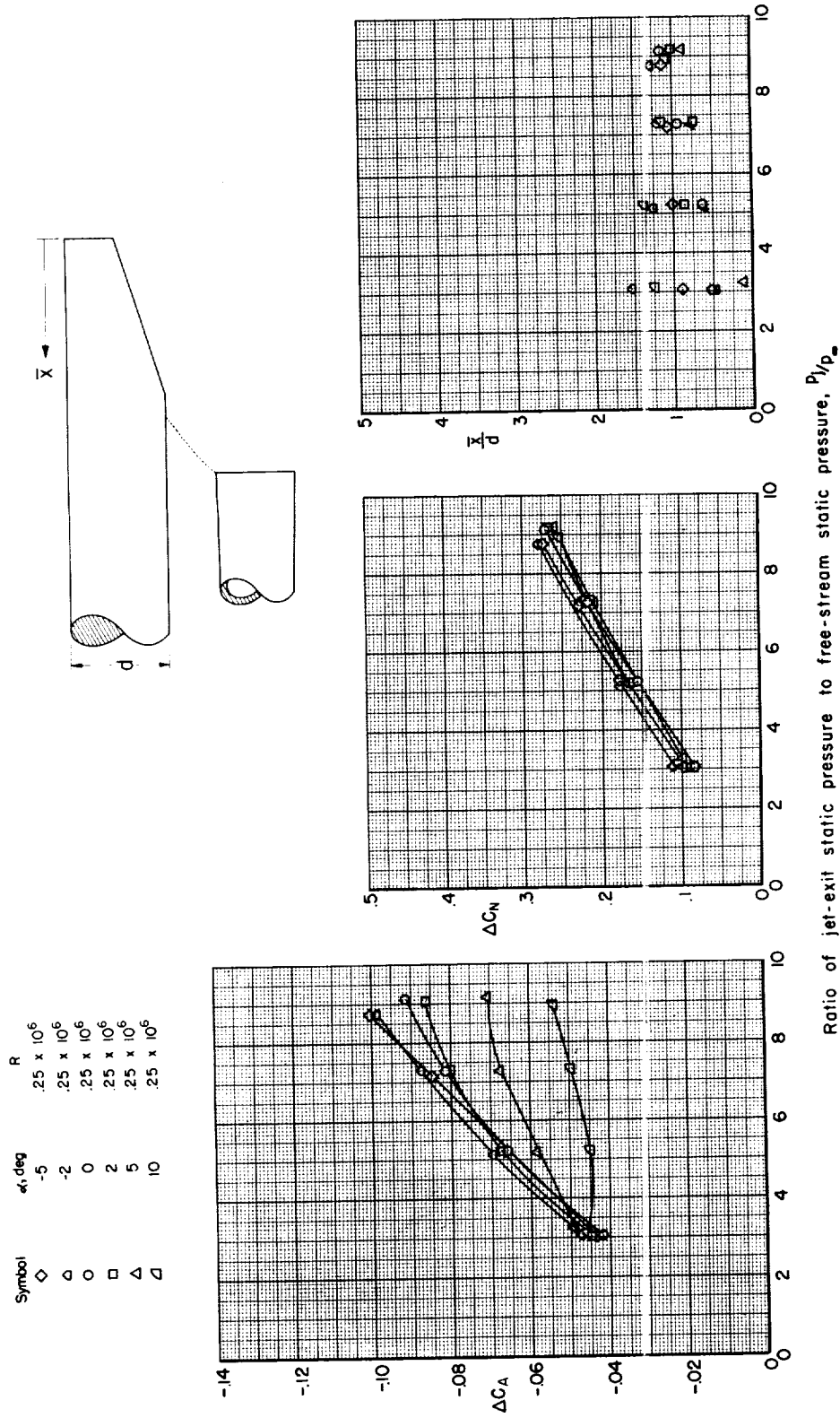
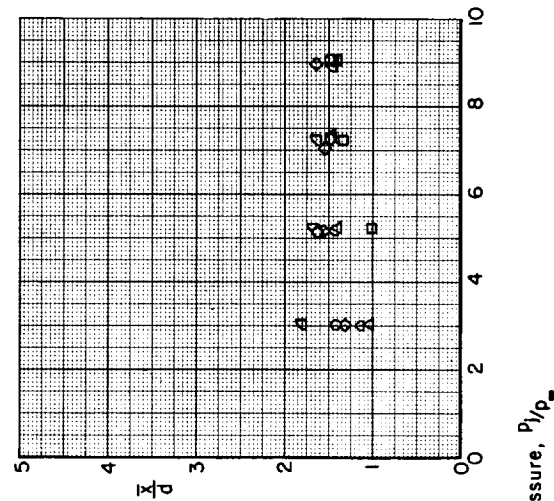
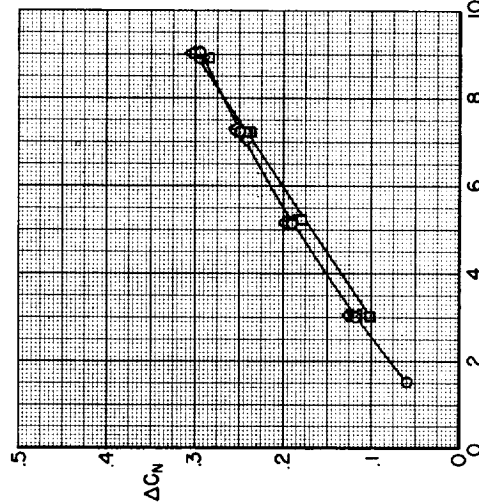
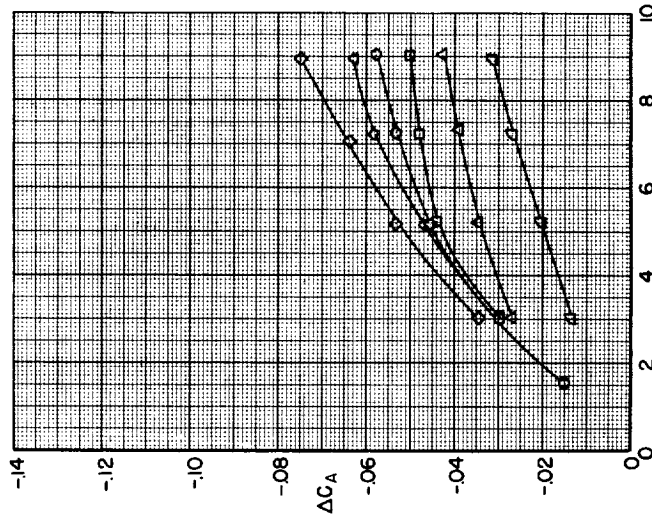
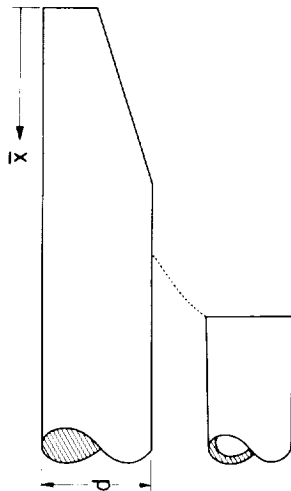


Figure 6.- Continued.

| Symbol | α , deg | R |
|-------------|----------------|-------------------|
| \diamond | -5 | $.25 \times 10^6$ |
| \triangle | -2 | $.25 \times 10^6$ |
| \circ | 0 | $.25 \times 10^6$ |
| \square | 2 | $.25 \times 10^6$ |
| \triangle | 5 | $.25 \times 10^6$ |
| ∇ | 10 | $.25 \times 10^6$ |



(22) Body E, $r/d = 0.5$, $x/d = 2.8$.

Figure 6.- Continued.

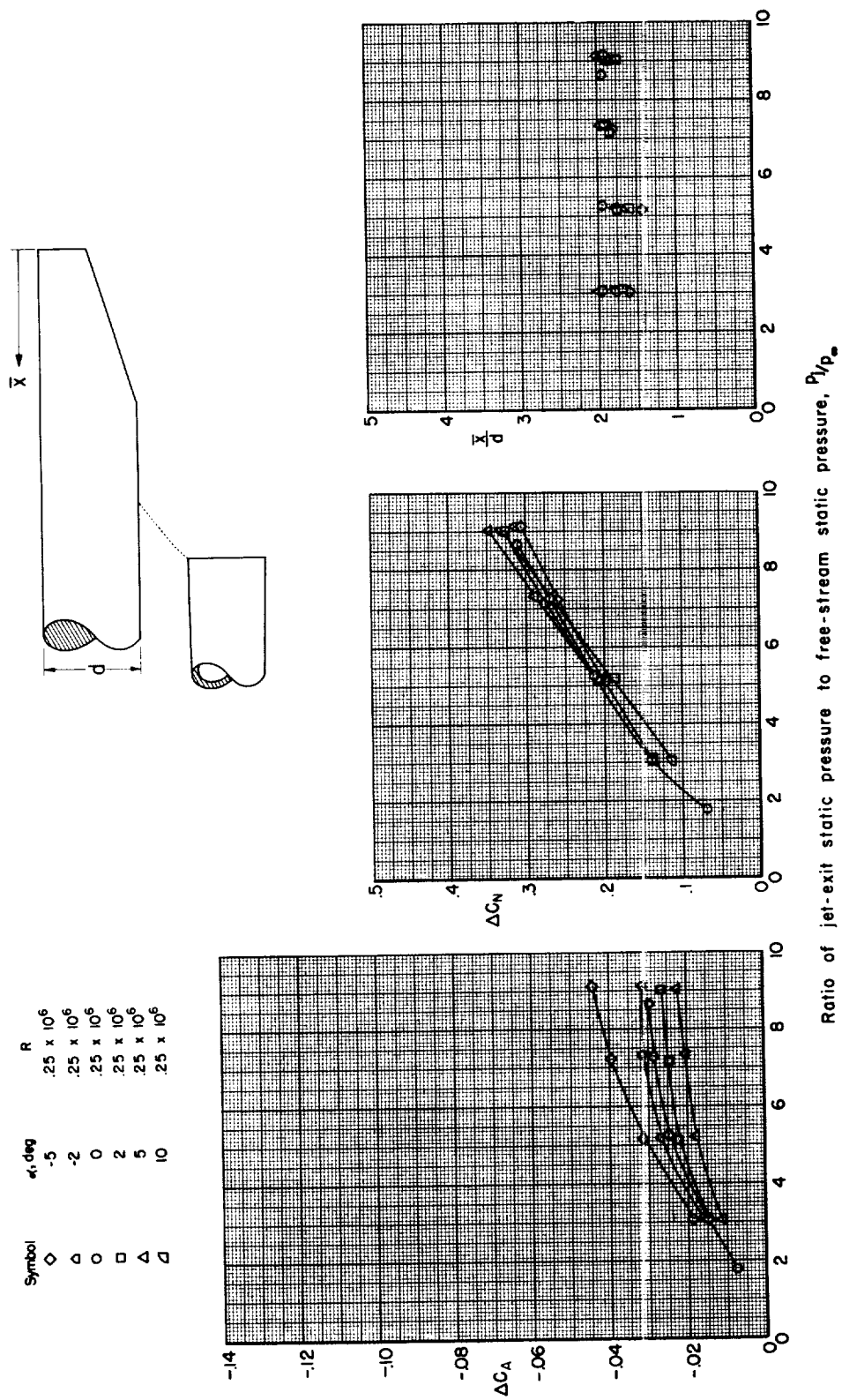
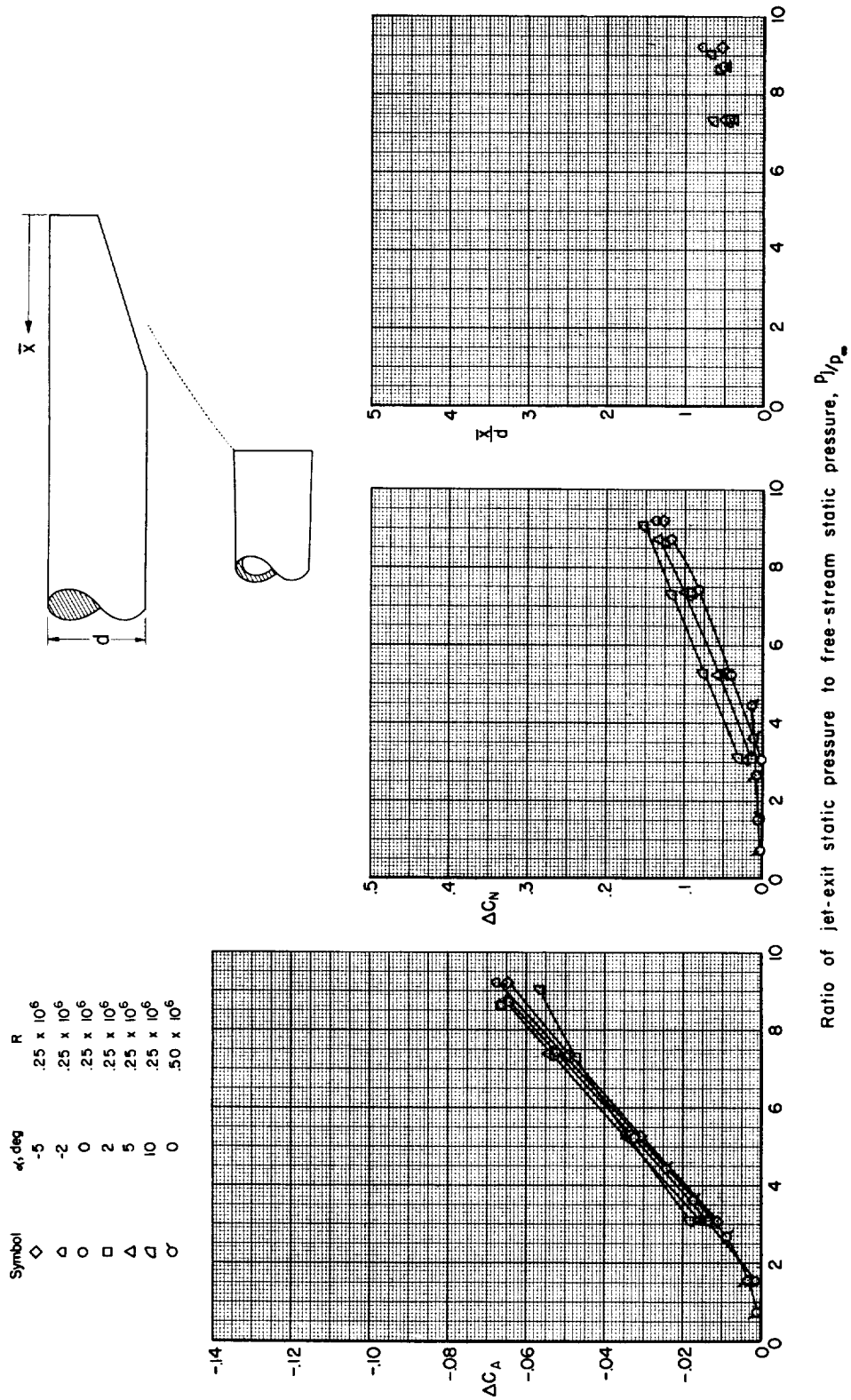
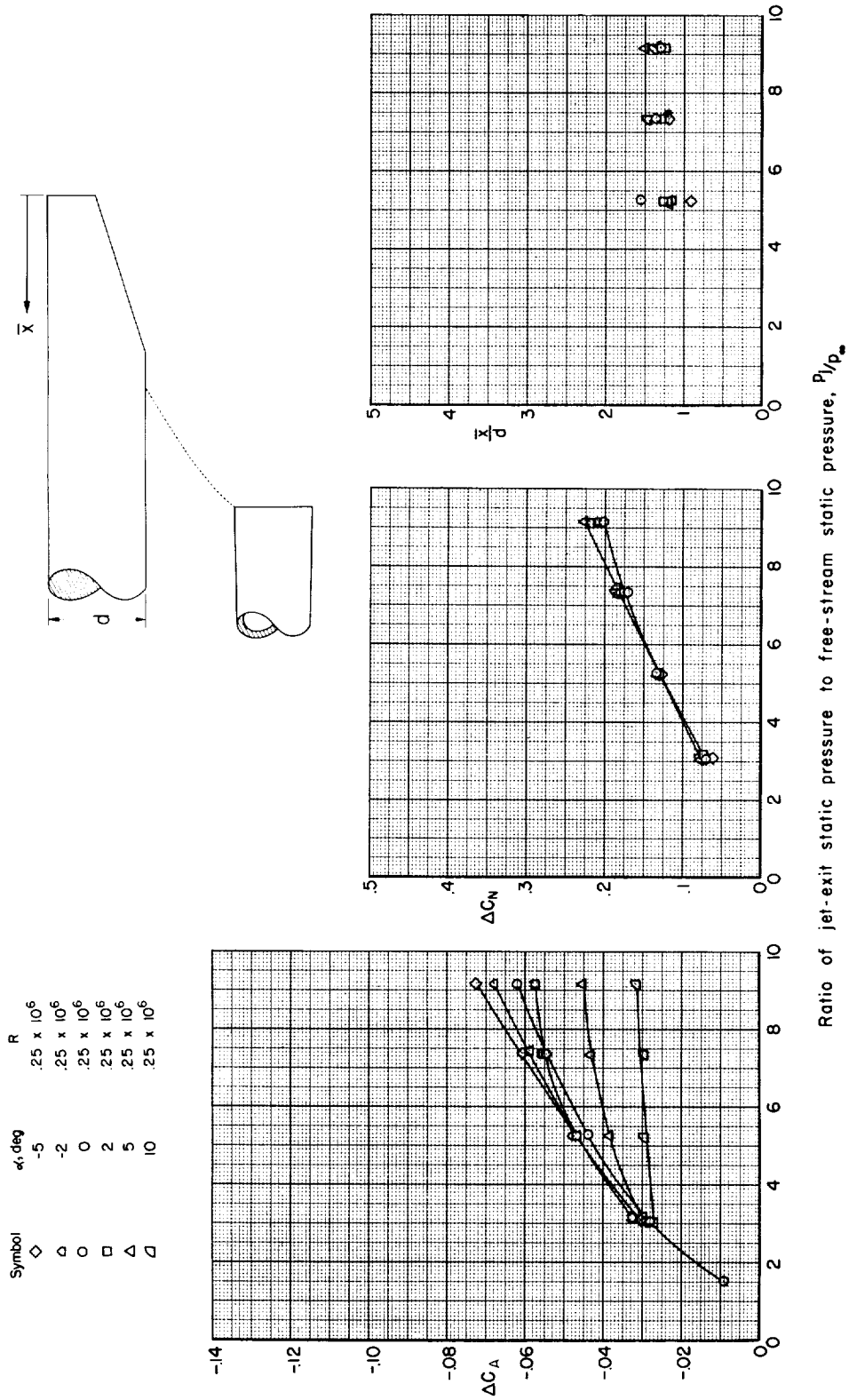


Figure 6.- Continued.



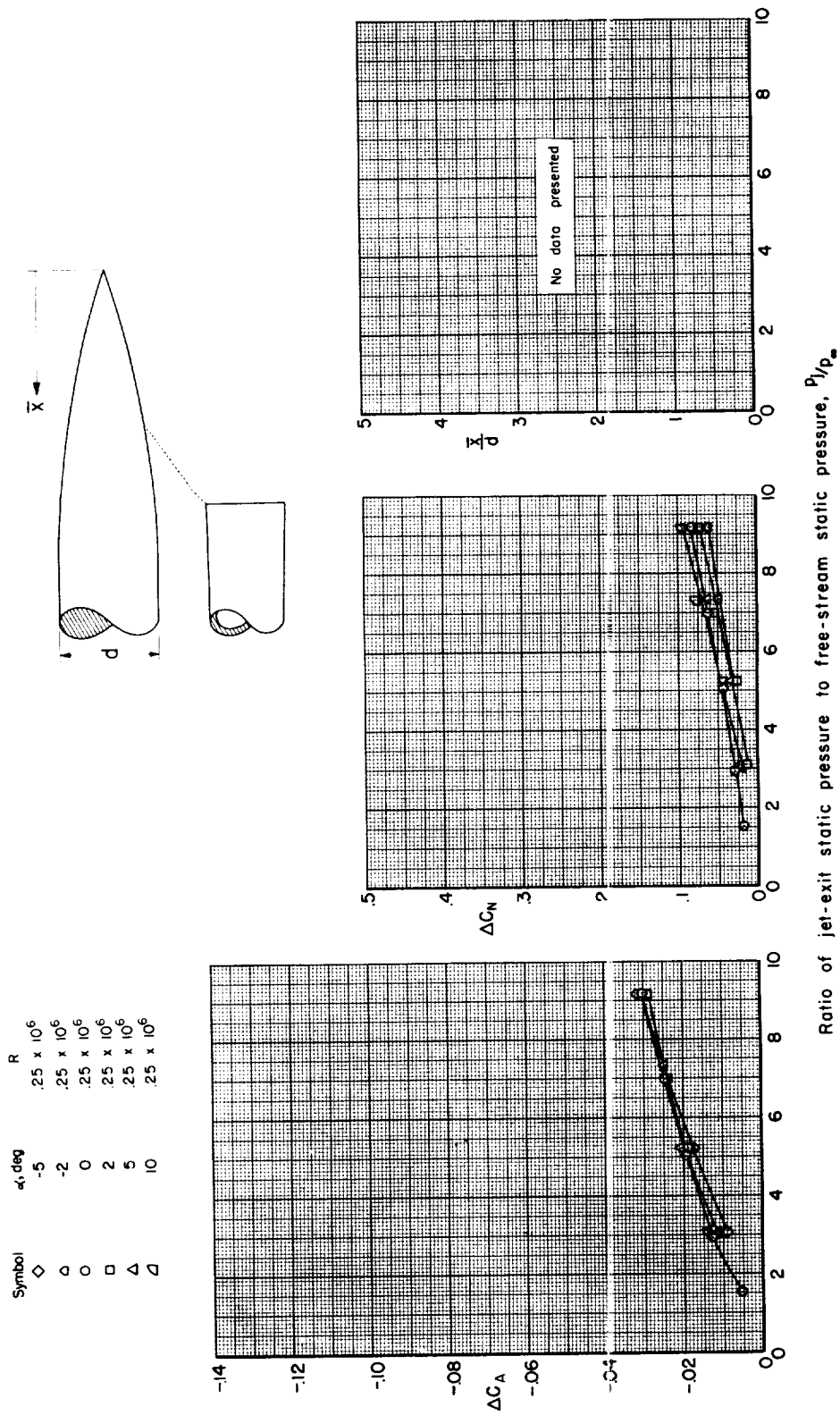
(nn) Body E, $r/d = 0.9$, $x/d = 2.4$.

Figure 6.- Continued.



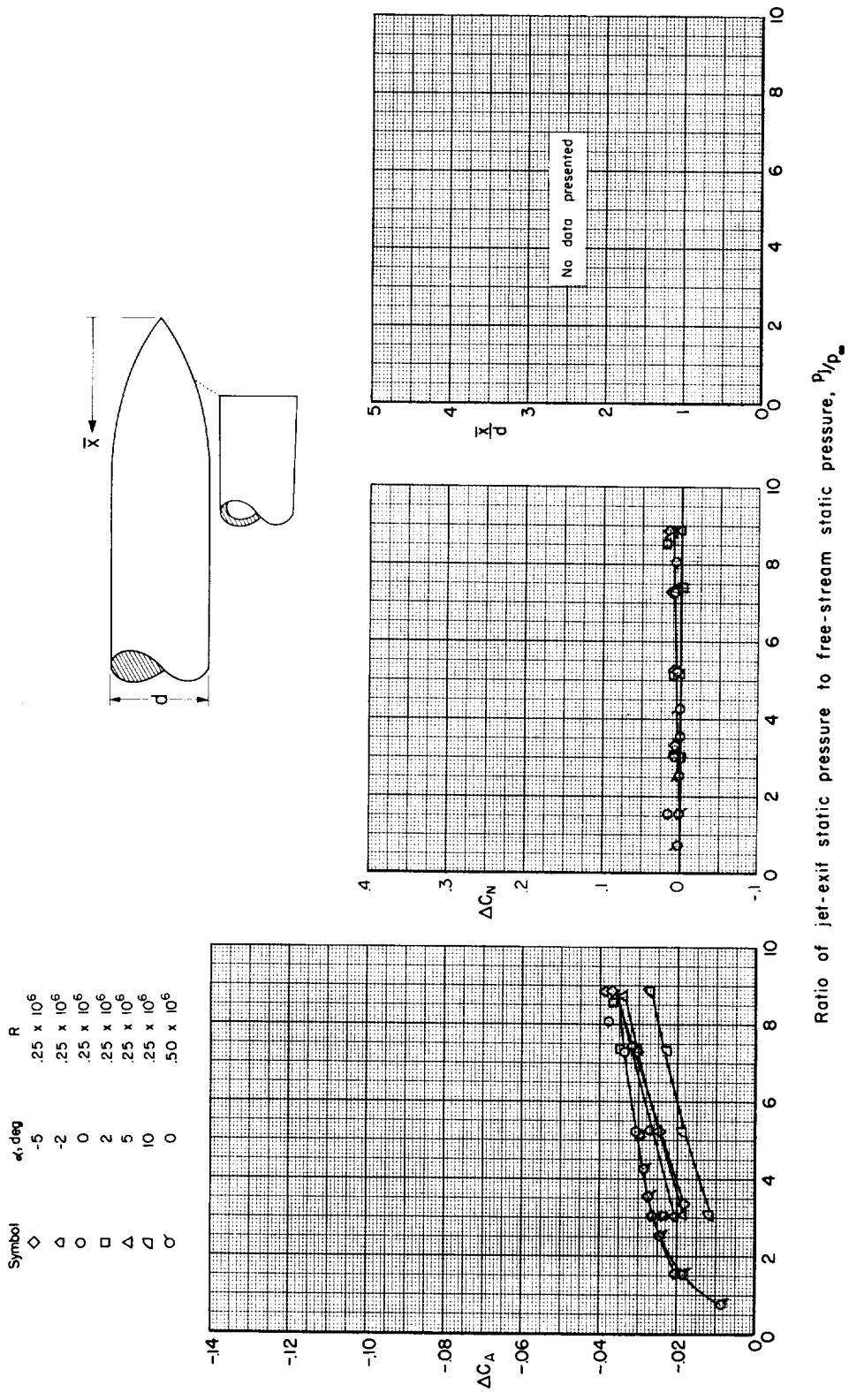
(pp) Body E, $r/d = 0.9$, $x/\bar{d} = 3.2$.

Figure 6.- Concluded.



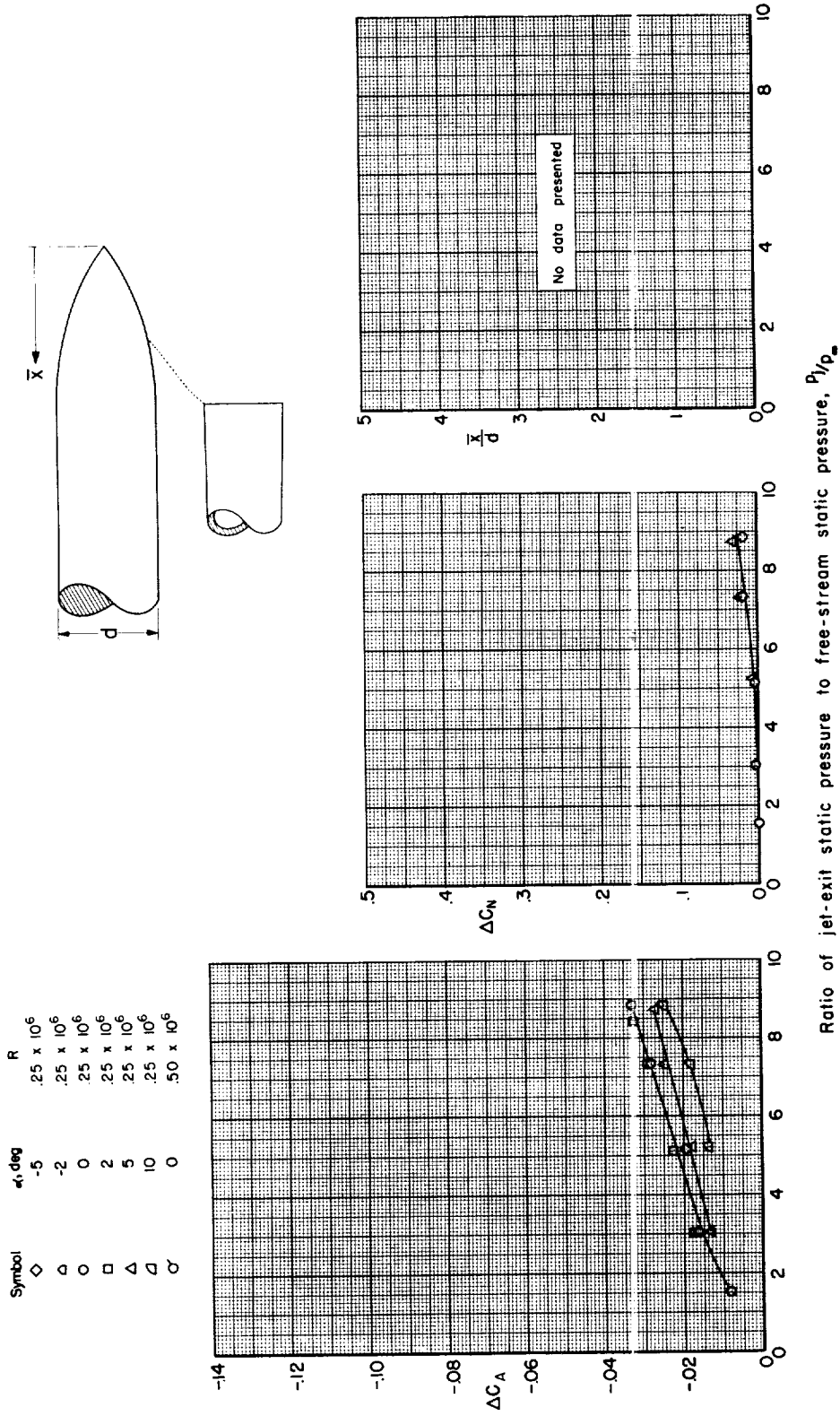
(a) Body F, $r/d = 0.5$, $x/d = 2.4$.

Figure 7.- Effect of pressure ratio on interference forces and center of pressure for ogival afterbodies.



(b) Body G, $r/d = 0.1$, $x/d = 0.8$.

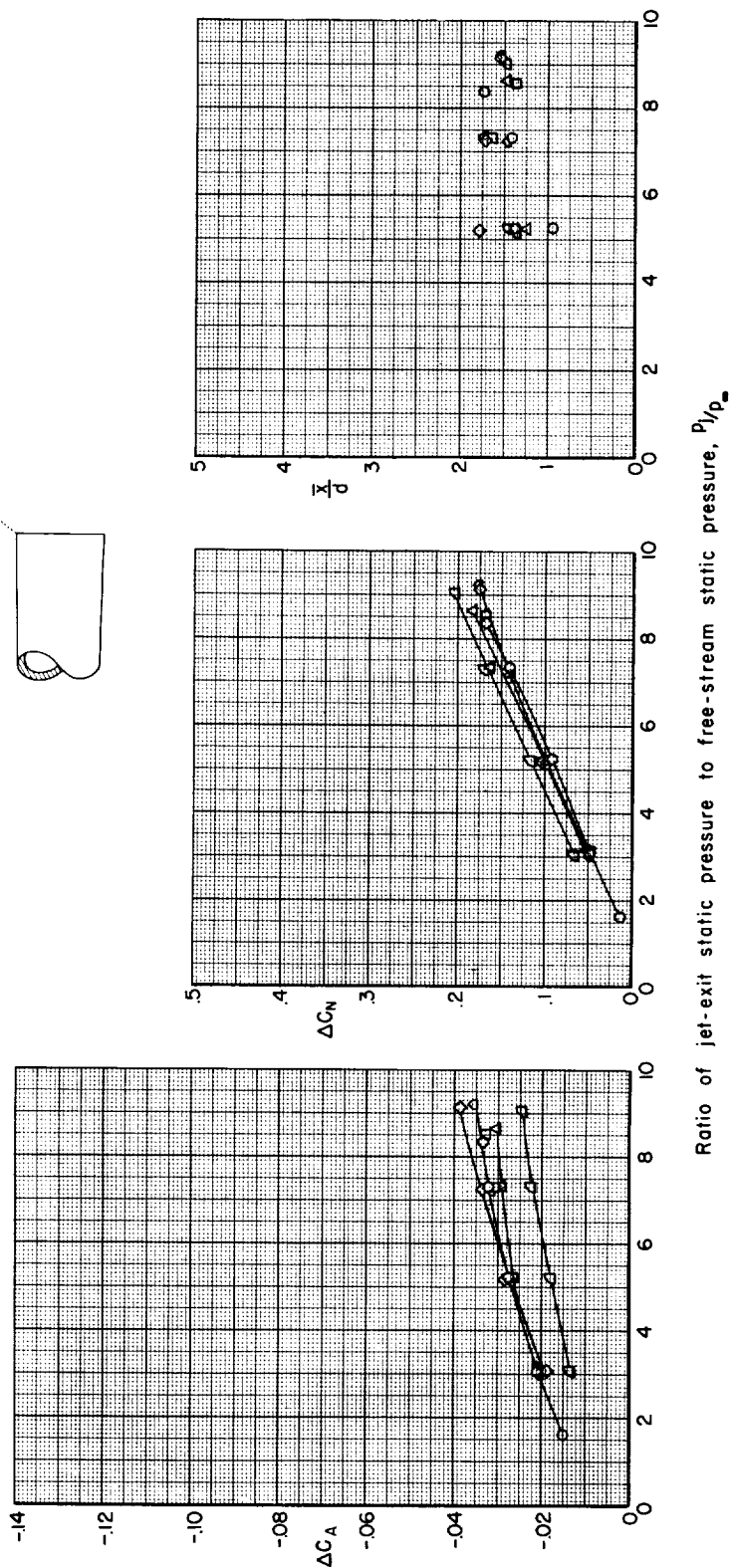
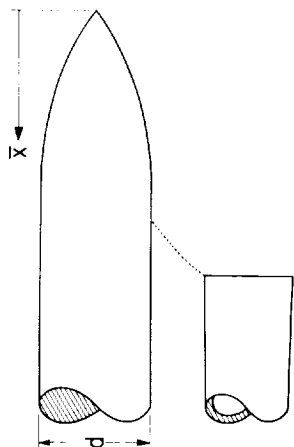
Figure 7.- Continued.



(c) Body G, $r/d = 0.5$, $x/d = 1.6$.

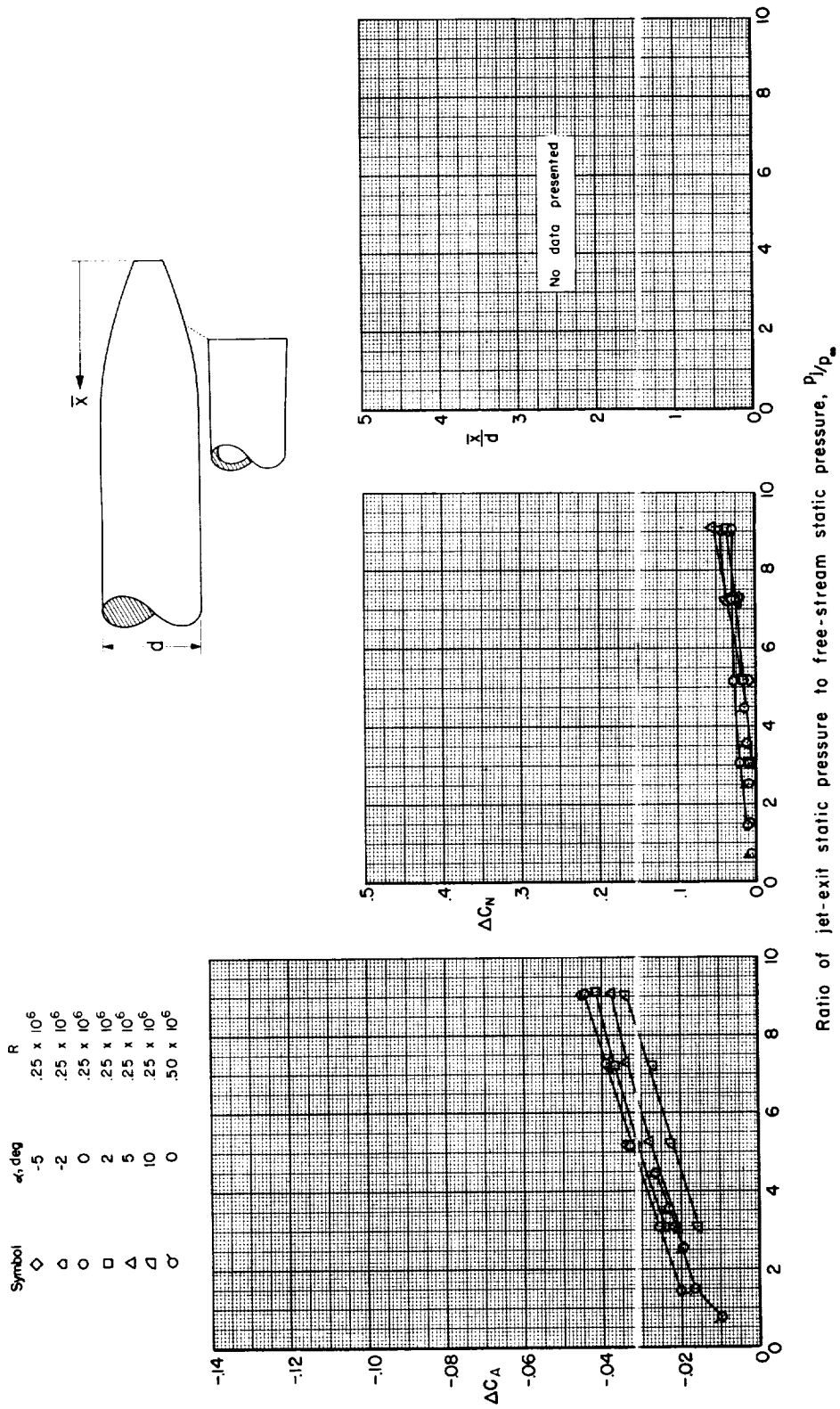
Figure 7.- Continued.

| Symbol | α_i, deg | R |
|-------------|------------------------|-------------------|
| \diamond | -5 | $.25 \times 10^6$ |
| \circ | -2 | $.25 \times 10^6$ |
| \square | 0 | $.25 \times 10^6$ |
| \triangle | 2 | $.25 \times 10^6$ |
| ∇ | 5 | $.25 \times 10^6$ |
| \square | 10 | $.25 \times 10^6$ |



(d) Body G, $r/\bar{d} = 0.5$, $x/\bar{d} = 2.4$.

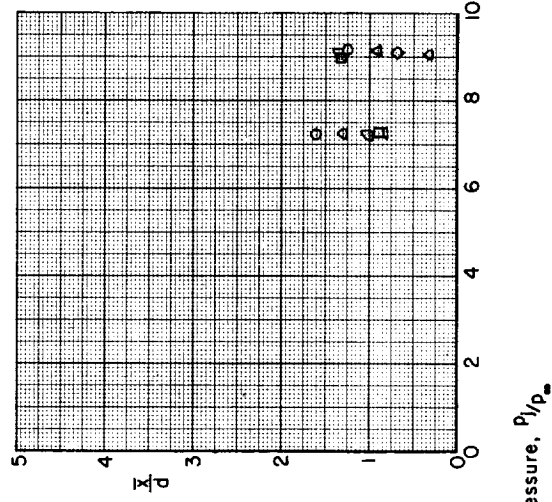
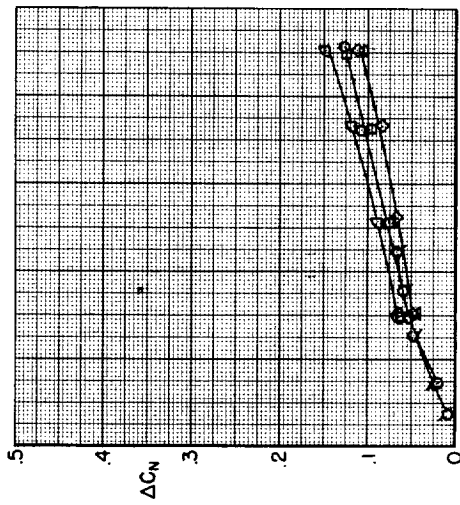
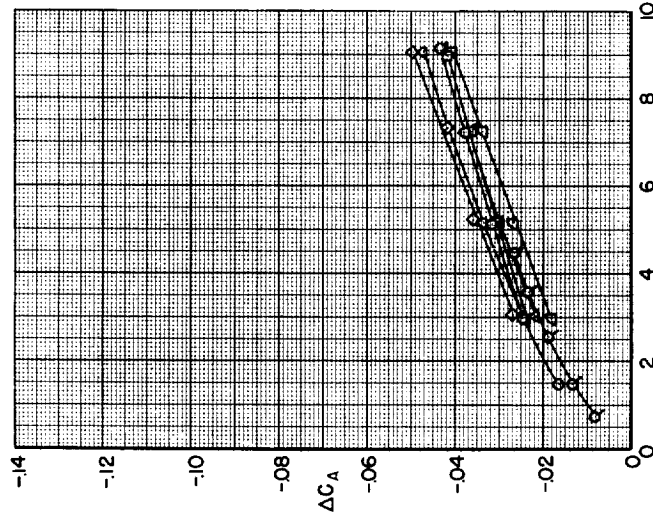
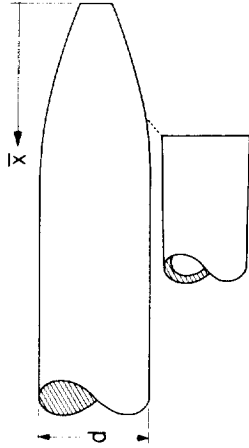
Figure 7.- Continued.



(e) Body H, $r/d = 0.1$, $x/d = 0.8$.

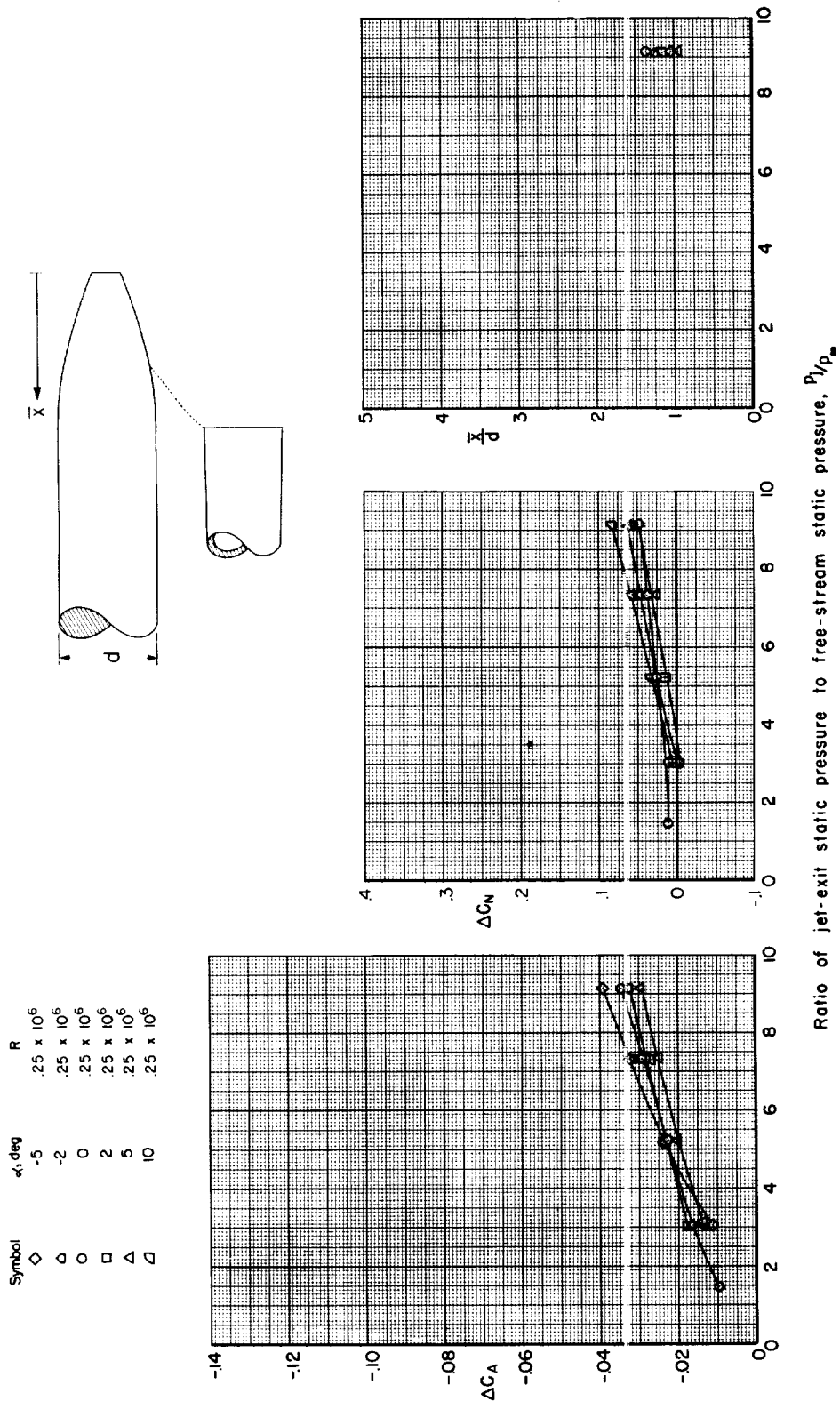
Figure 7.- Continued.

| Symbol | α , deg | R |
|-------------|----------------|-------------------|
| \diamond | -5 | $.25 \times 10^6$ |
| \triangle | -2 | $.25 \times 10^6$ |
| \circ | 0 | $.25 \times 10^6$ |
| \square | 2 | $.25 \times 10^6$ |
| \triangle | 5 | $.25 \times 10^6$ |
| \triangle | 10 | $.25 \times 10^6$ |
| σ | 0 | $.50 \times 10^6$ |



(f) Body H, $r/d = 0.1$, $x/d = 1.2$.

Figure 7.- Continued.



(g) Body H, $r/d = 0.5$, $x/d = 1.6$.

Figure 7.- Continued.

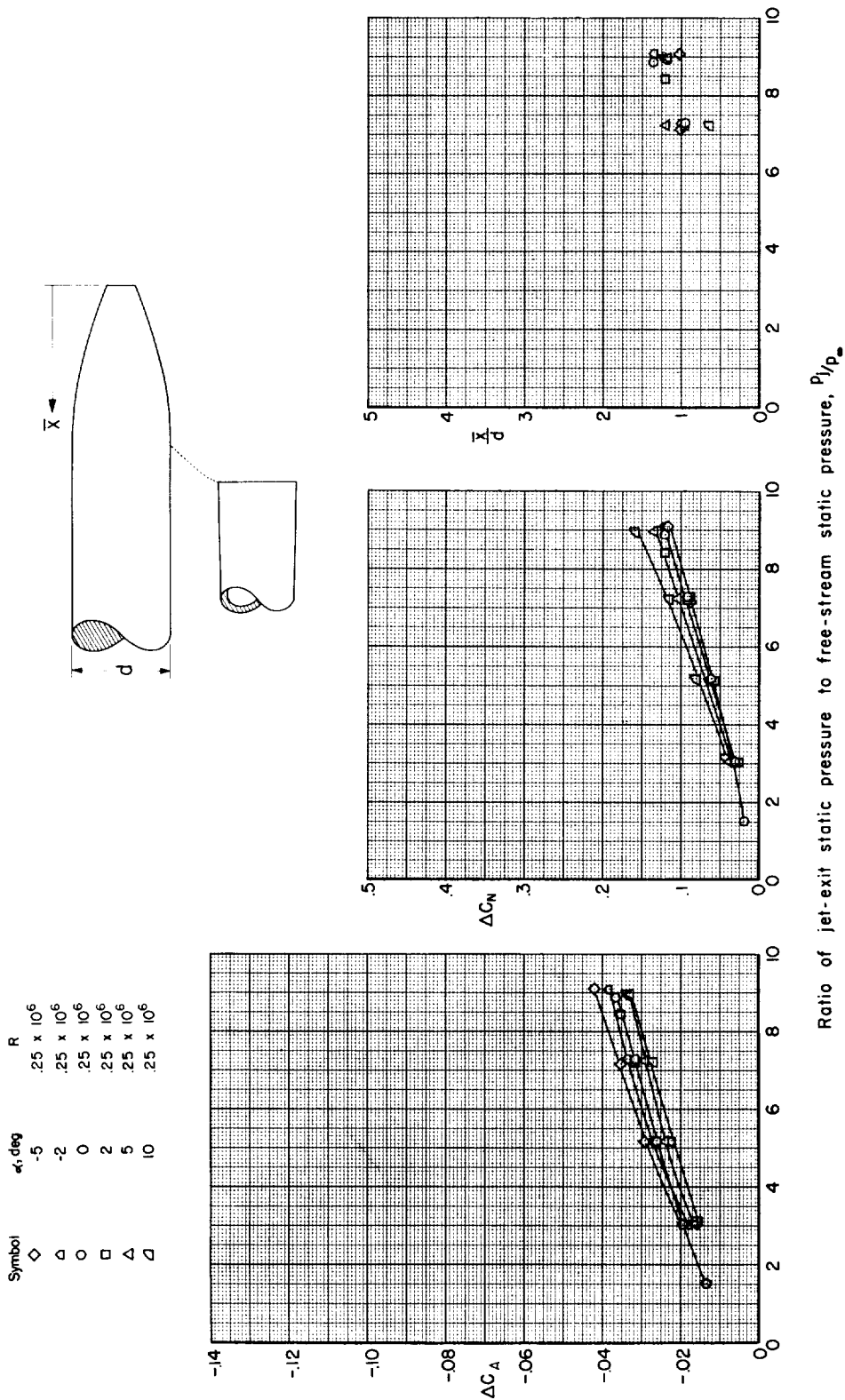
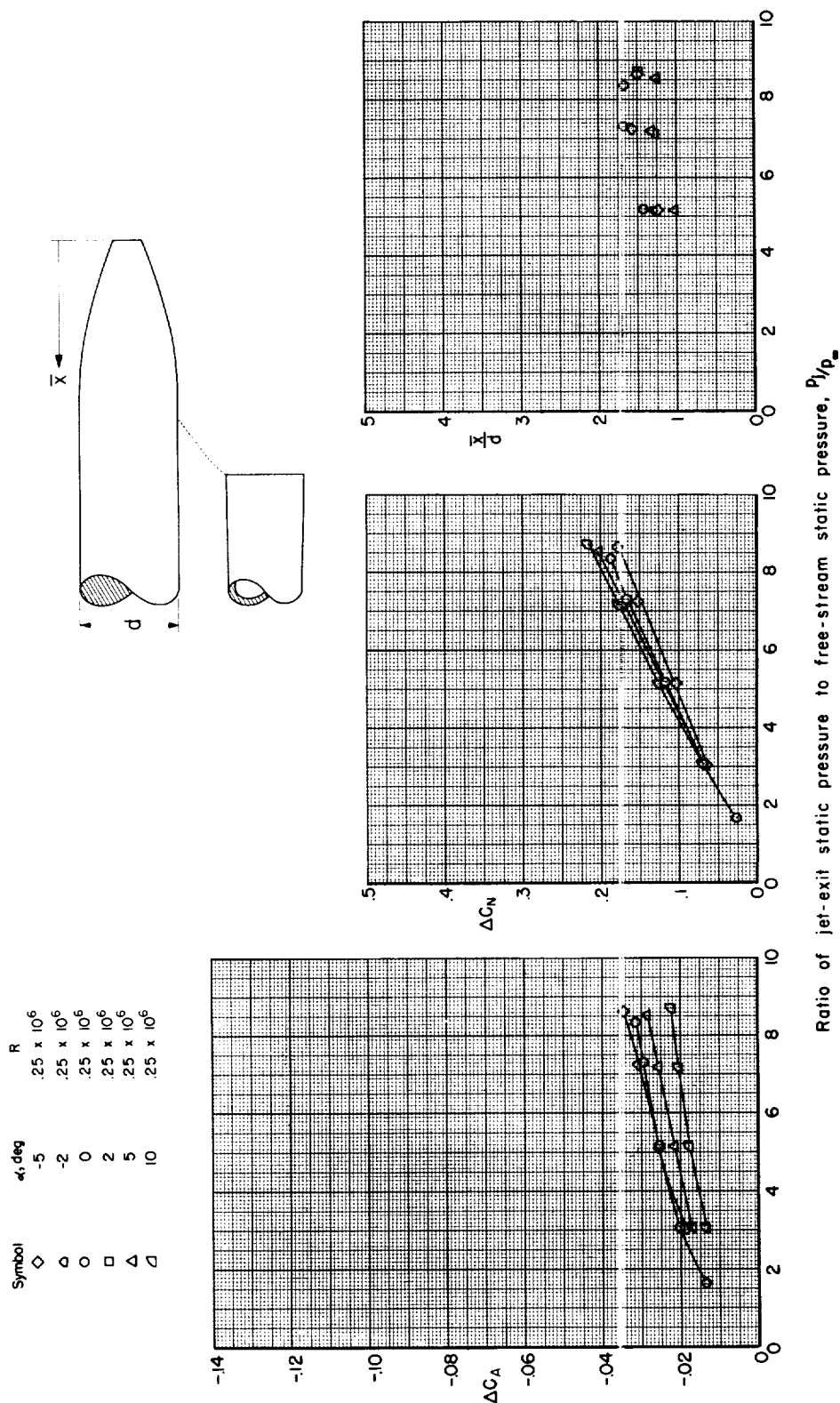


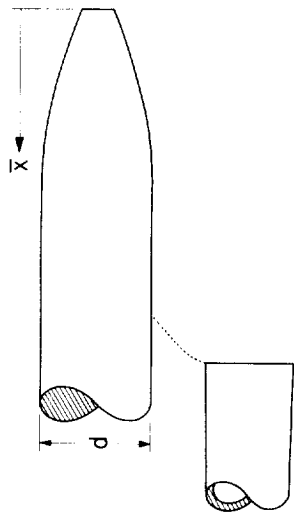
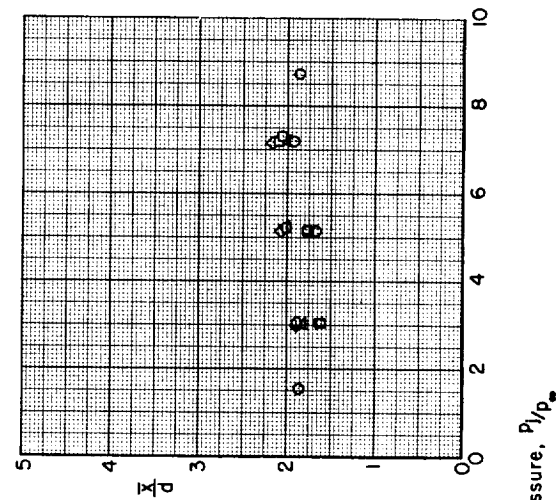
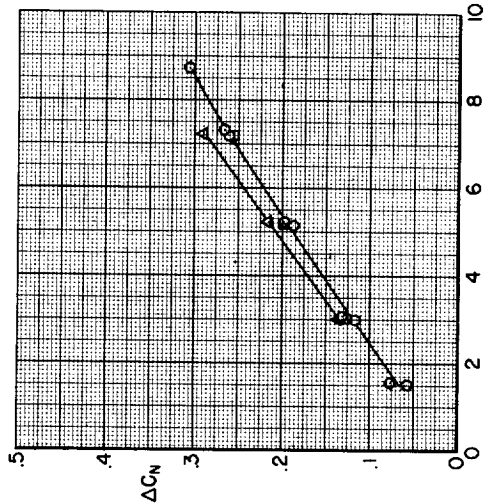
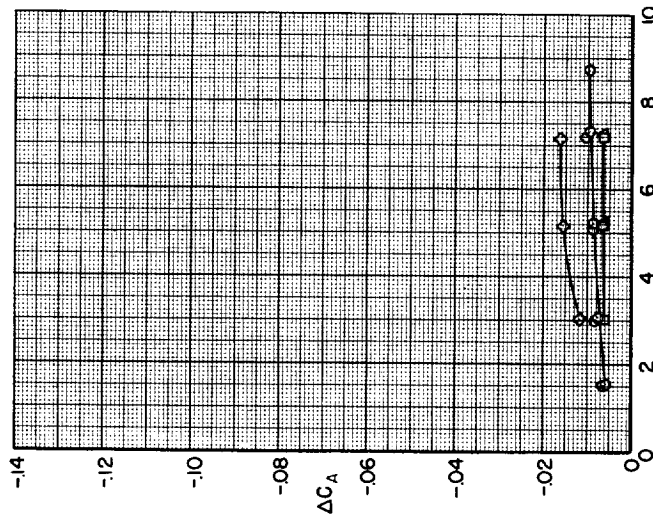
Figure 7.- Continued.



(i) Body H, $r/d = 0.5$, $x/d = 2.4$.

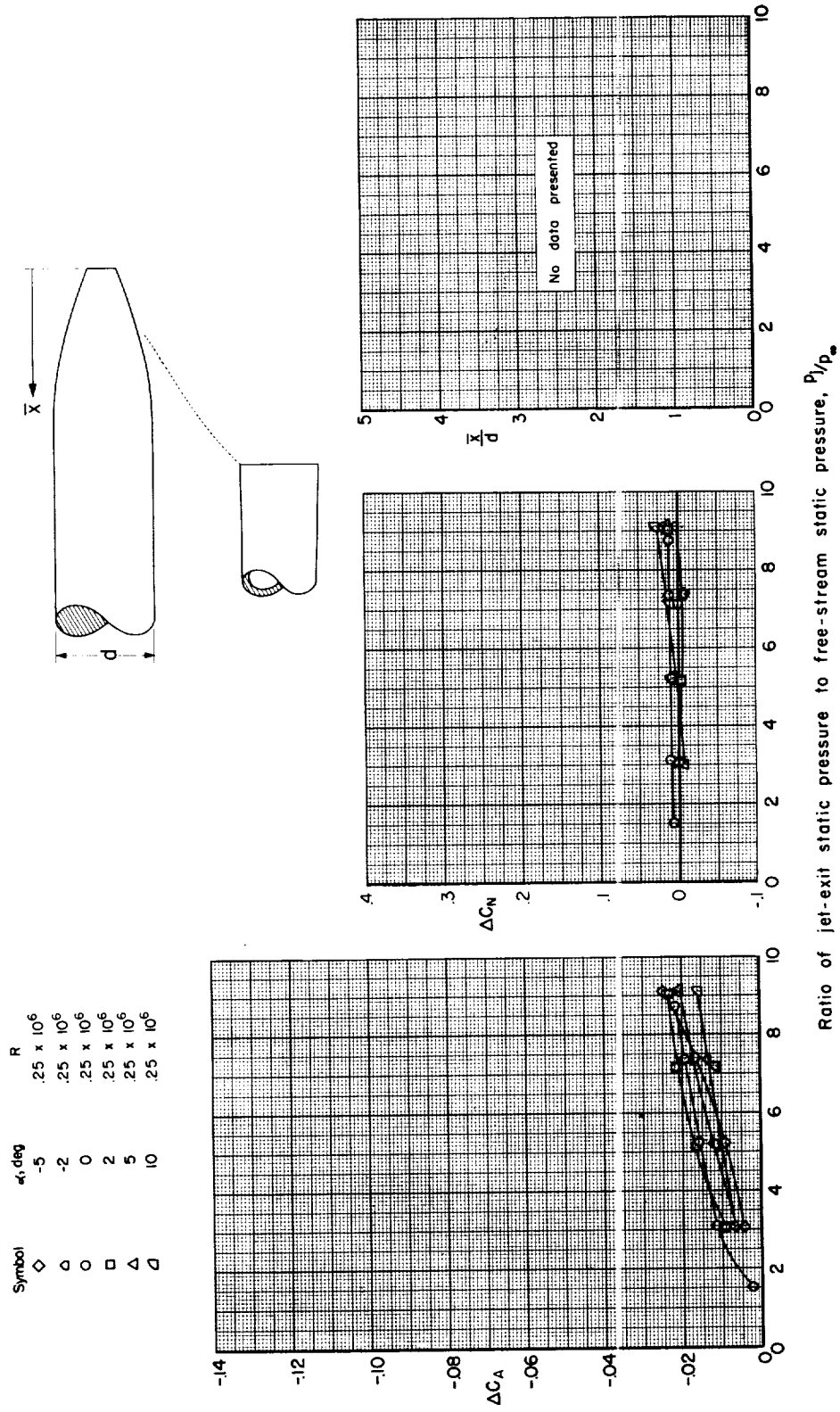
Figure 7.- Continued.

| Symbol | α , deg | R |
|-------------|----------------|-------------------|
| \diamond | -5 | $.25 \times 10^6$ |
| \triangle | -2 | $.25 \times 10^6$ |
| \circ | 0 | $.25 \times 10^6$ |
| \square | 2 | $.25 \times 10^6$ |
| \triangle | 5 | $.25 \times 10^6$ |
| ∇ | 10 | $.25 \times 10^6$ |



(j) Body H, $r/d = 0.5$, $x/d = 3.2$.

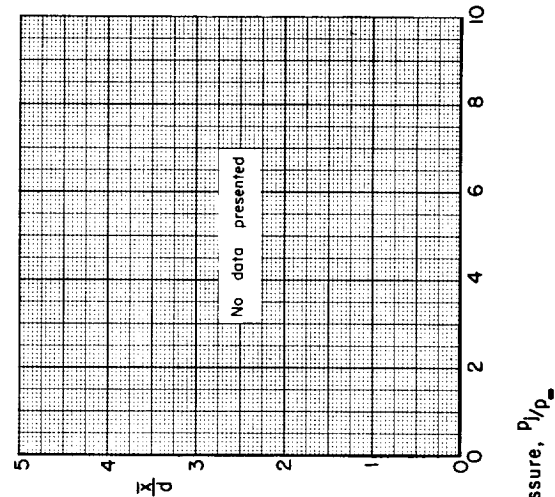
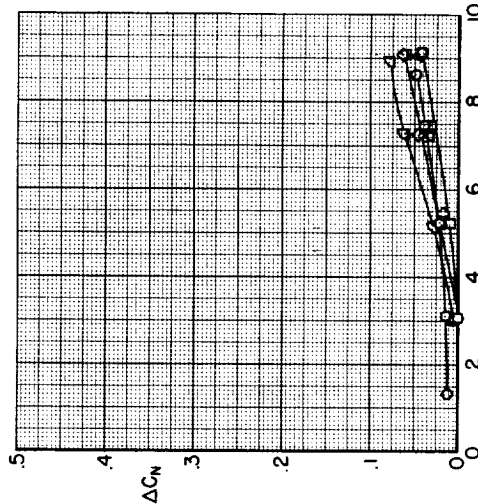
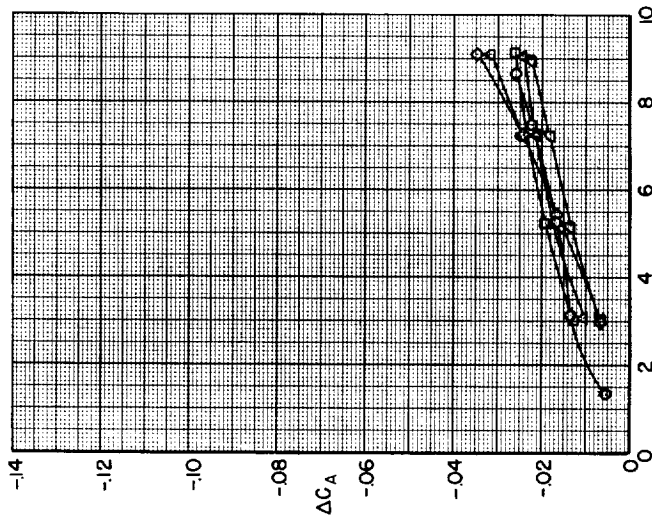
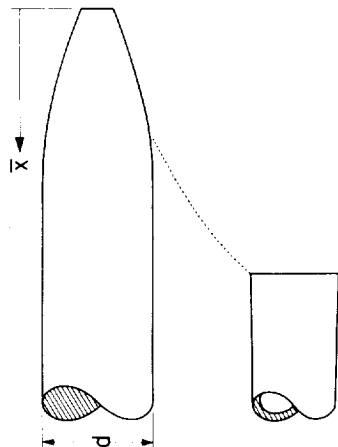
Figure 7.- Continued.



(k) Body H, $r/\bar{a} = 0.9$, $x/\bar{a} = 2.0$.

Figure 7.- Continued.

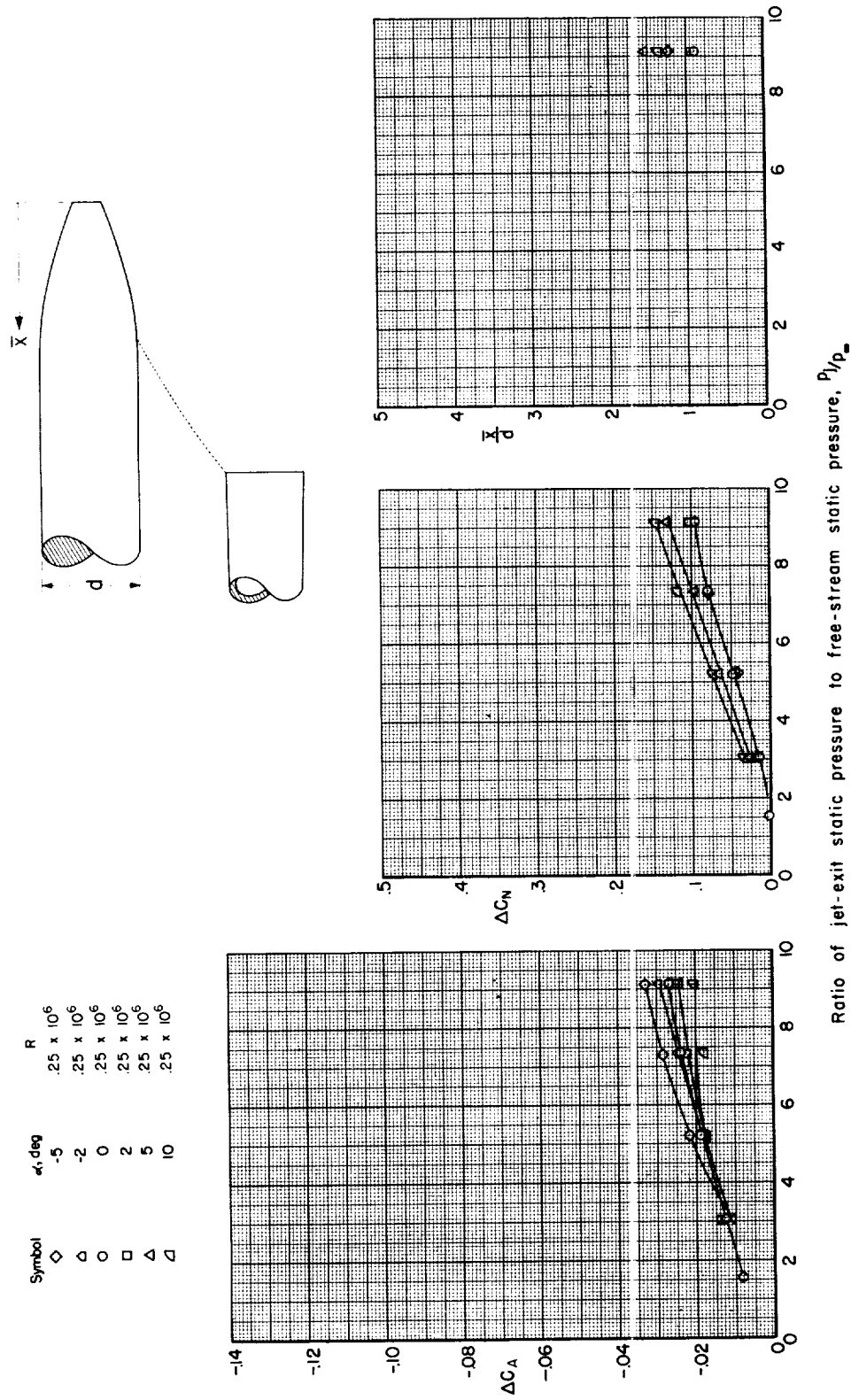
| Symbol | α , deg | R |
|-------------|----------------|-------------------|
| \diamond | -5 | $.25 \times 10^6$ |
| \triangle | -2 | $.25 \times 10^6$ |
| \circ | 0 | $.25 \times 10^6$ |
| \square | 2 | $.25 \times 10^6$ |
| \triangle | 5 | $.25 \times 10^6$ |
| ∇ | 10 | $.25 \times 10^6$ |



Ratio of jet-exit static pressure to free-stream static pressure, P/P_∞

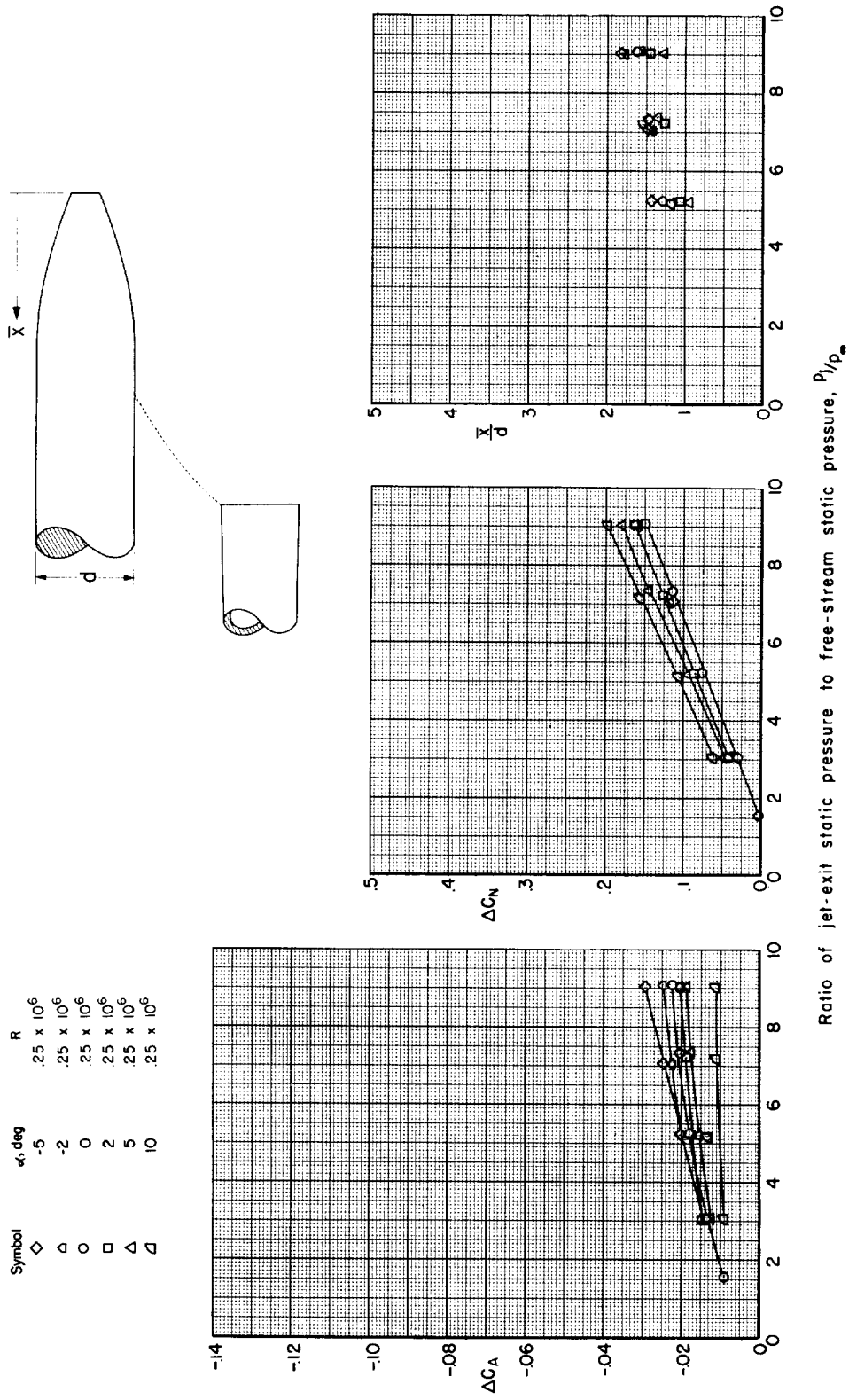
(7) Body H, $r/d = 0.9$, $x/d = 2.4$.

Figure 7.- Continued.



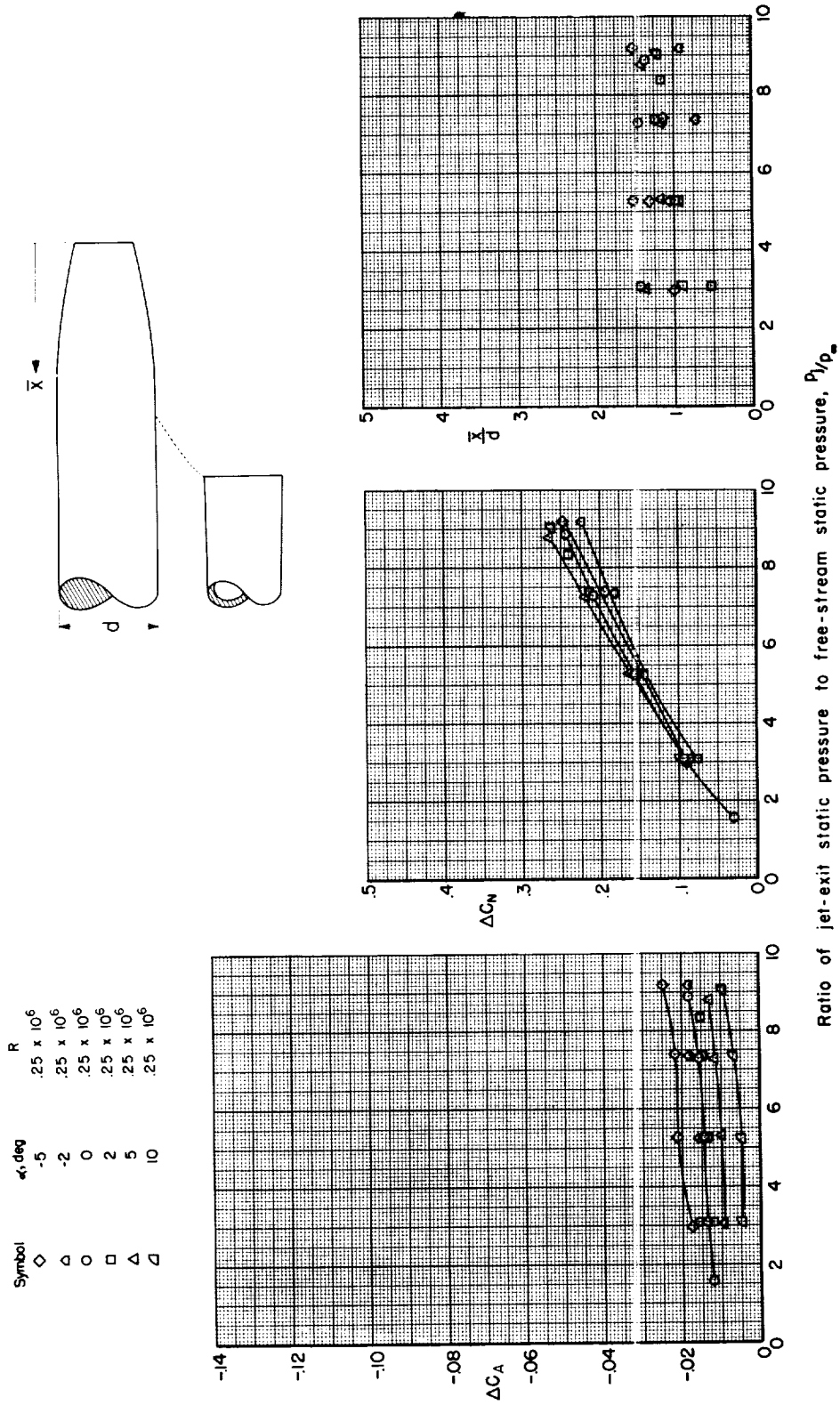
(m) Body H, $r/d = 0.9$, $x/d = 2.8$.

Figure 7.- Continued.



(n) Body H, $r/d = 0.9$, $x/d = 3.2$.

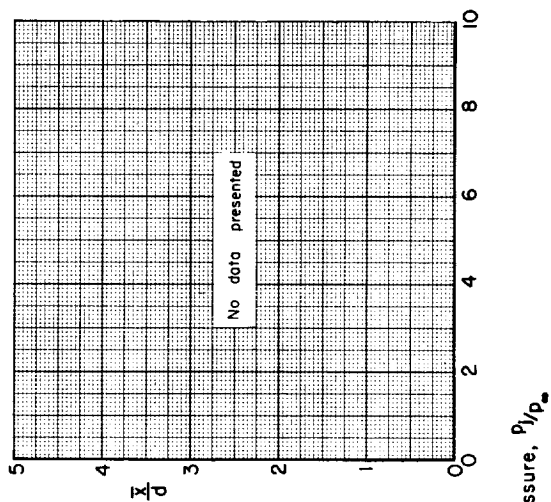
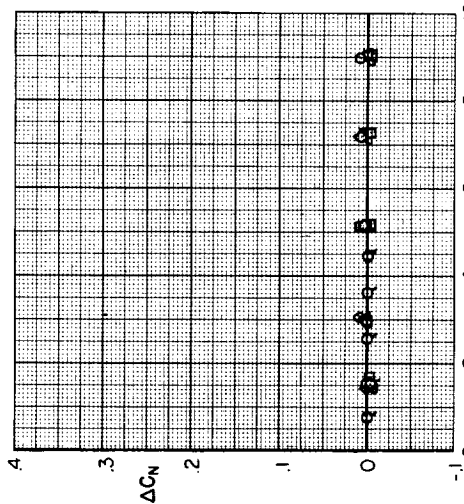
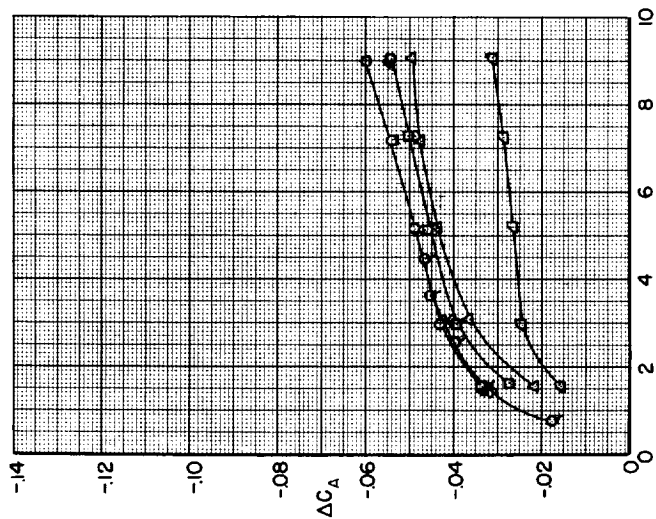
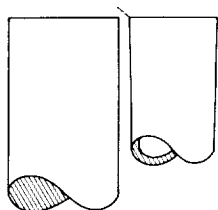
Figure 7.- Continued.



(o) Body I, $r/d = 0.5$, $x/d = 2.4$.

Figure 7.- Continued.

| Symbol | α_1 , deg | R |
|-------------|------------------|-------------------|
| \diamond | -5 | $.25 \times 10^6$ |
| \triangle | -2 | $.25 \times 10^6$ |
| \circ | 0 | $.25 \times 10^6$ |
| \square | 2 | $.25 \times 10^6$ |
| \triangle | 5 | $.25 \times 10^6$ |
| \square | 10 | $.25 \times 10^6$ |



(p) Body J, $r/d = 0.1$, $x/d = 0.8$.

Figure 7.- Concluded.

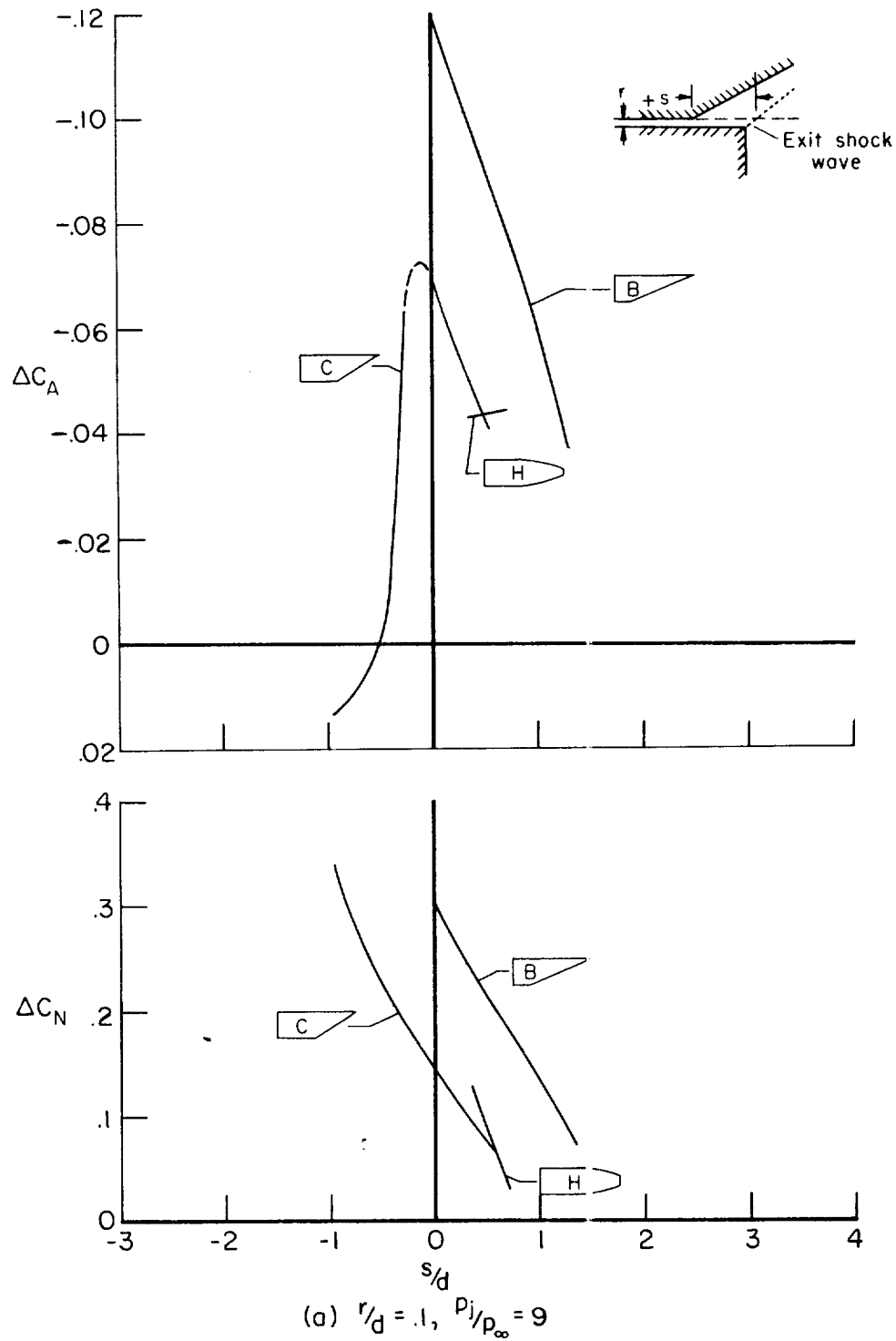


Figure 8.- Effect of axial position of exit shock wave on interference forces; $\alpha = 0$.

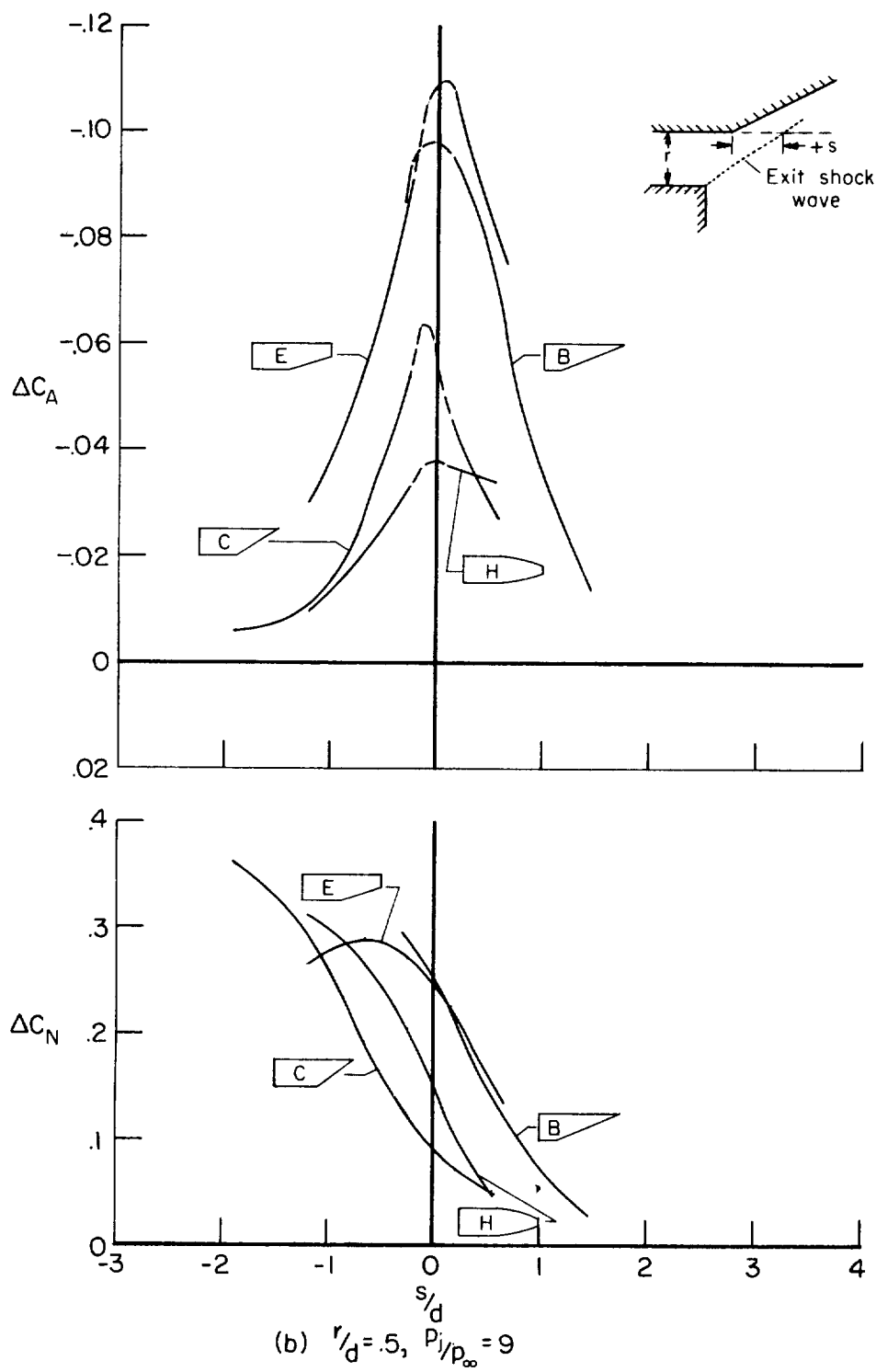


Figure 8.- Continued.

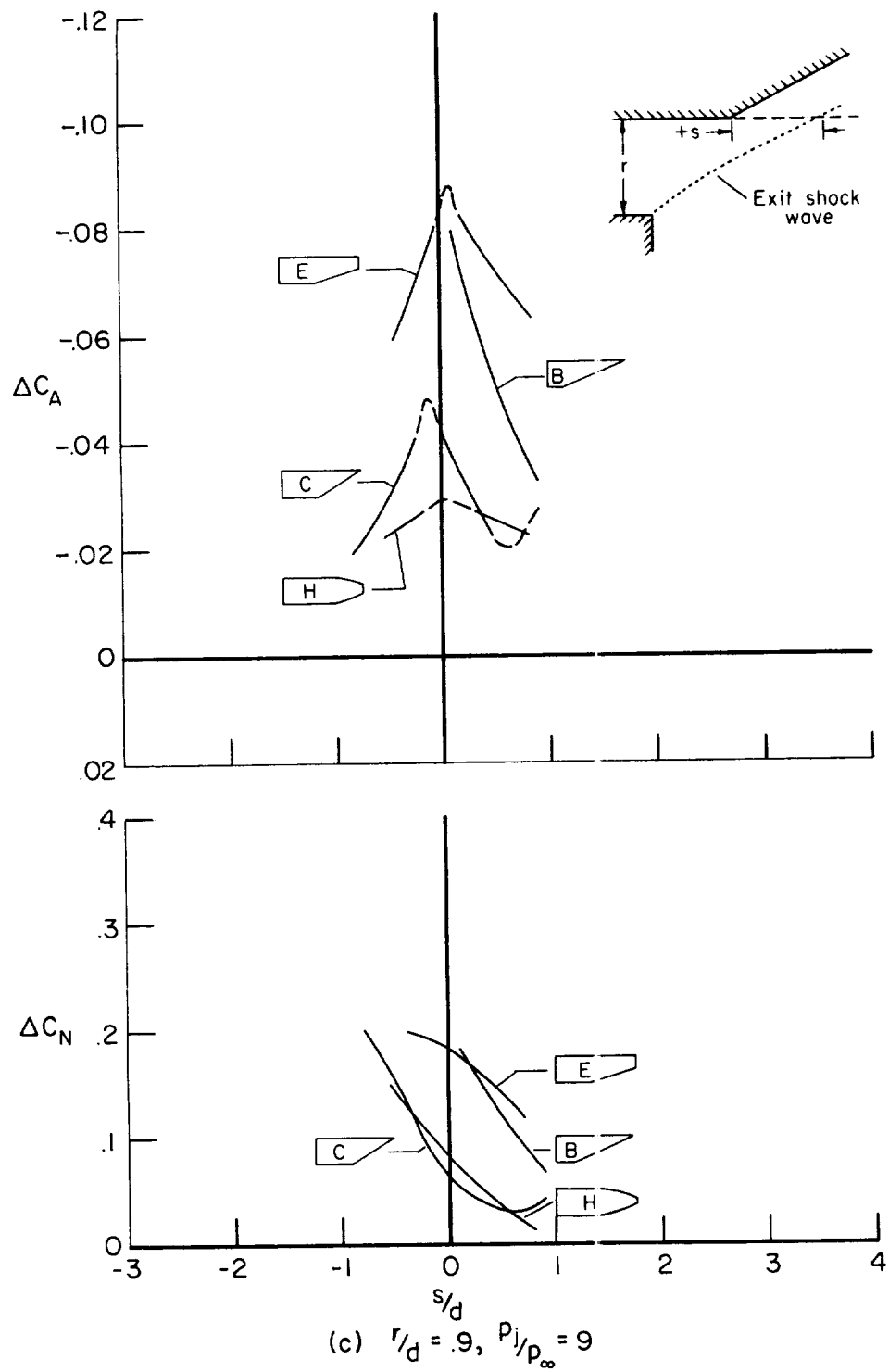


Figure 8.- Continued.

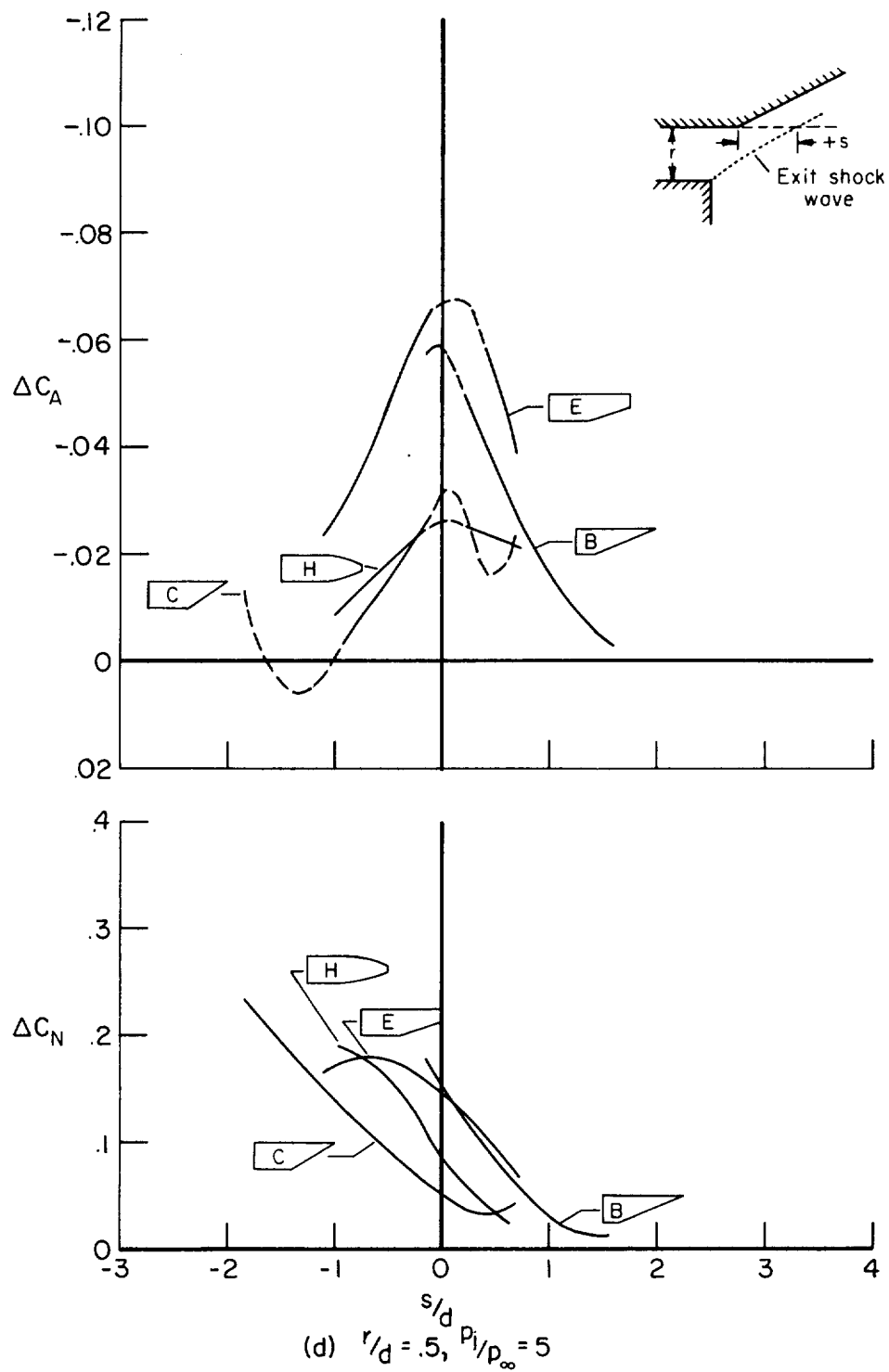


Figure 8.- Concluded.

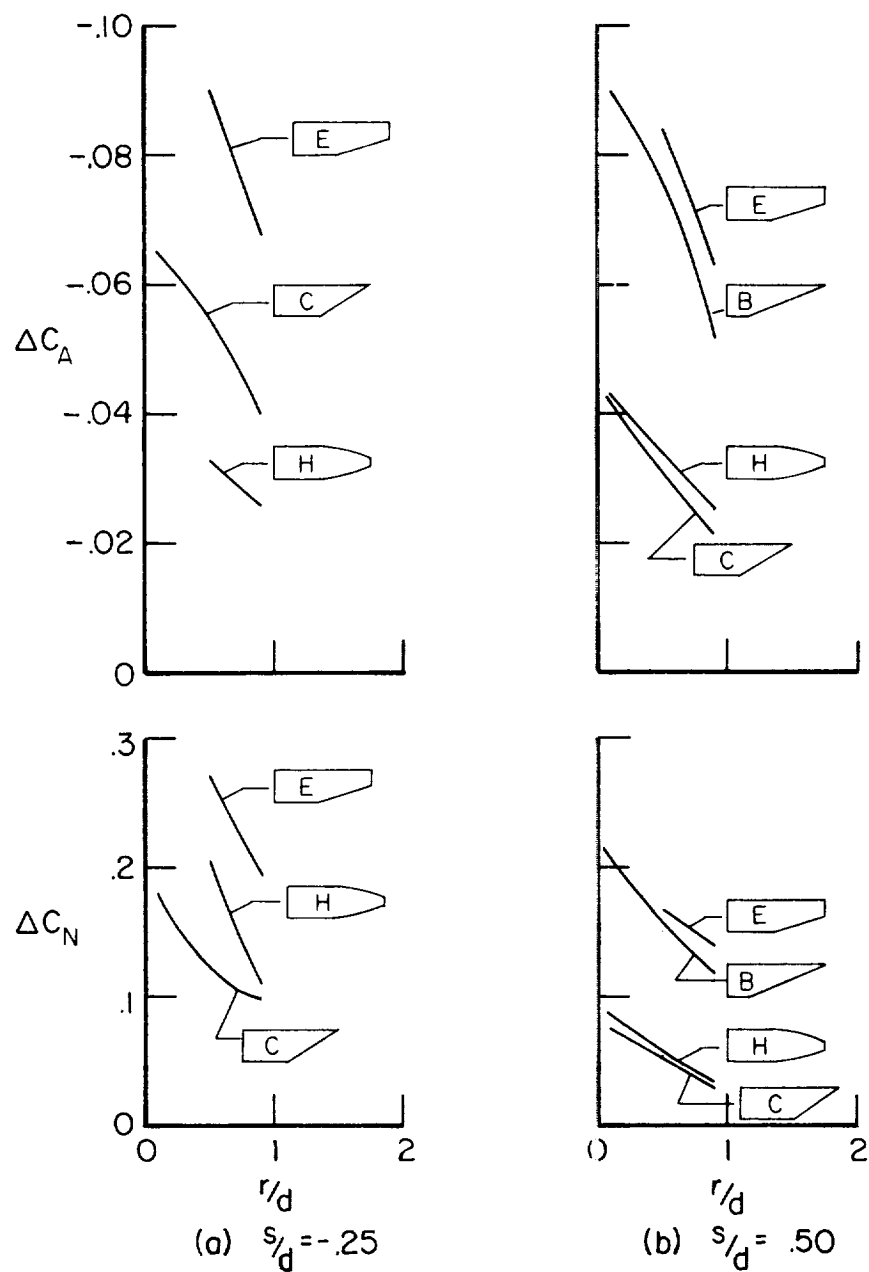
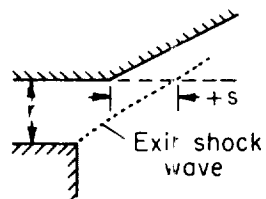
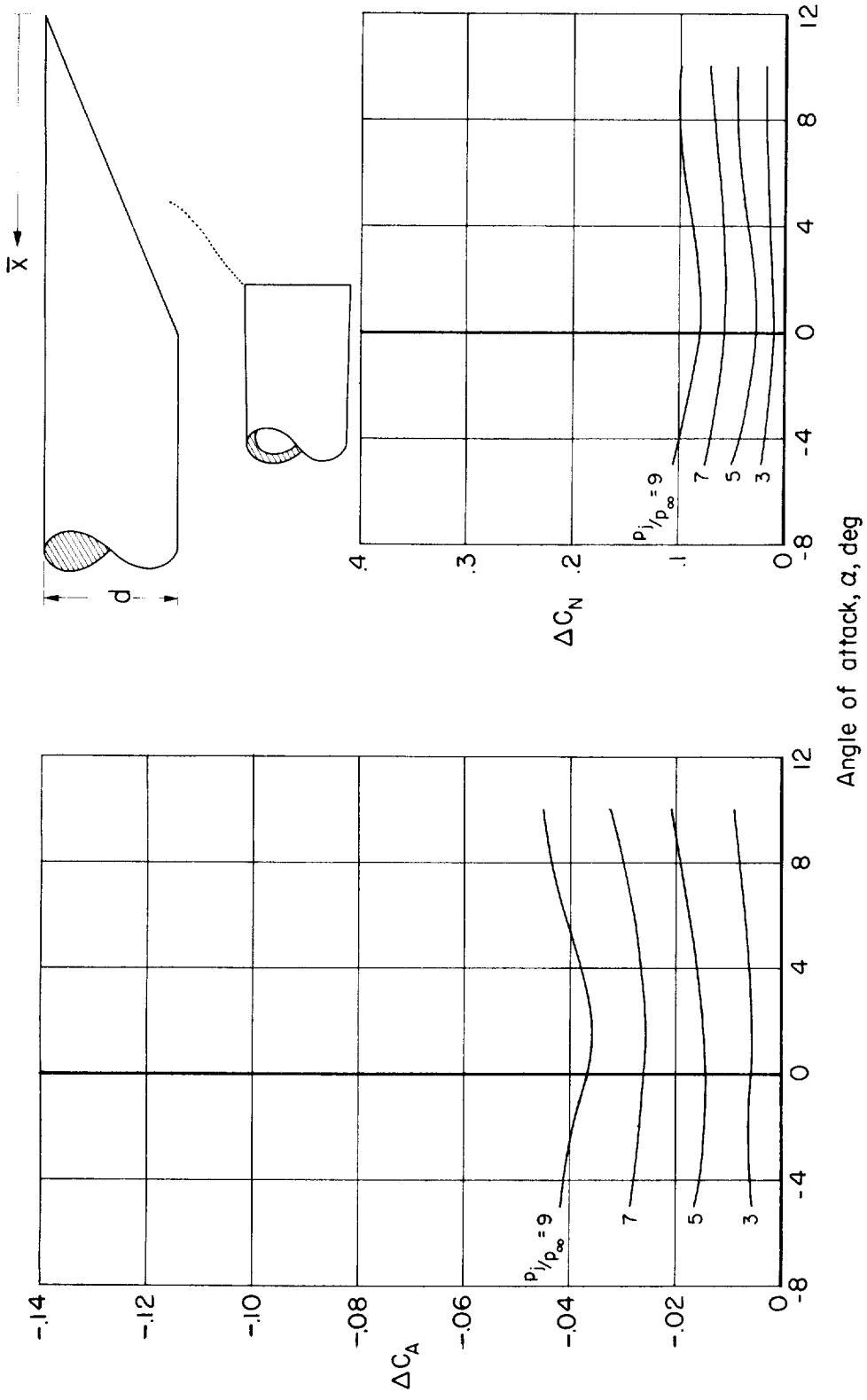
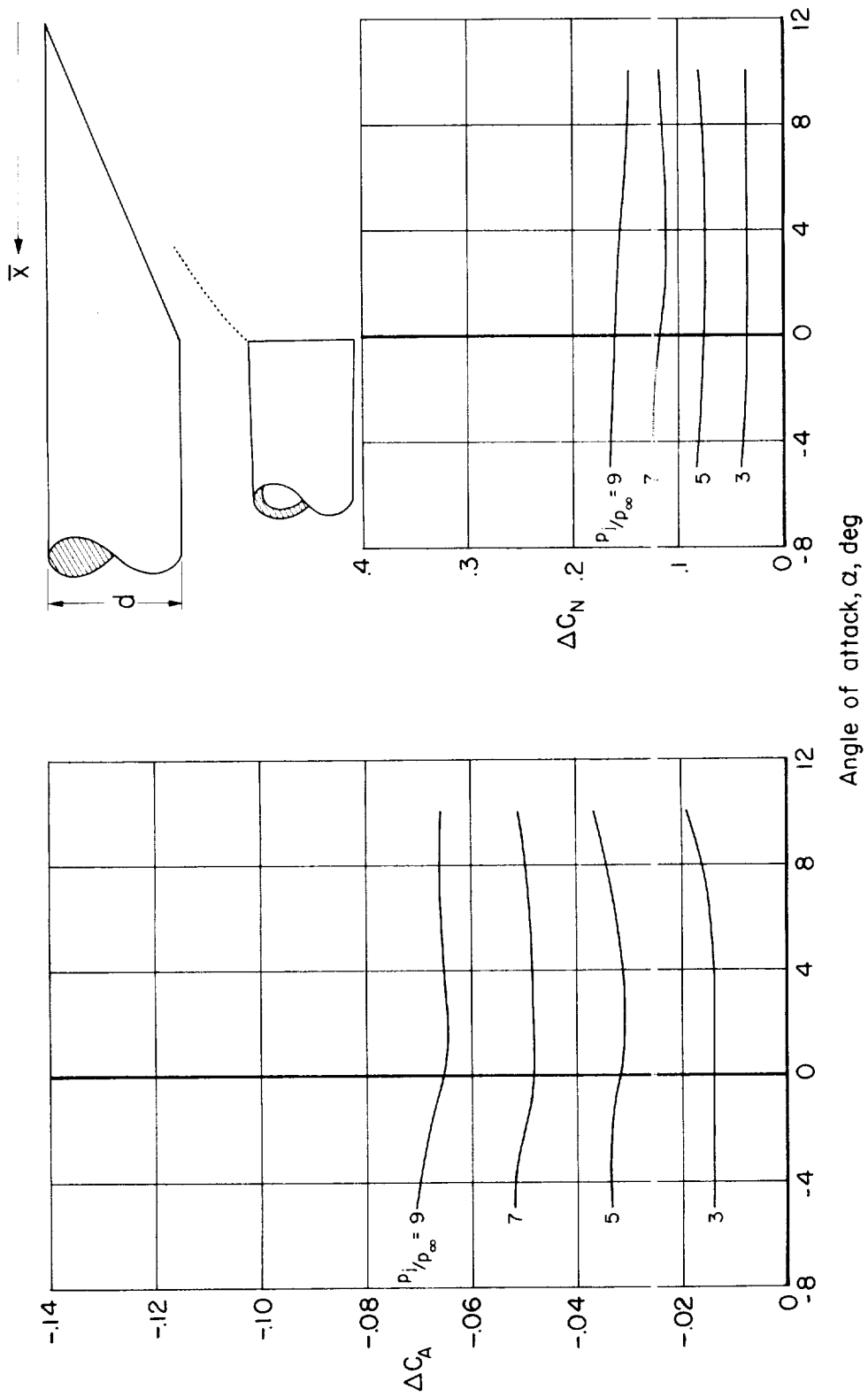


Figure 9.- Effect of radial position of nacelle on interference forces;
 $\alpha = 0$, $p_j/p_\infty = 9$.



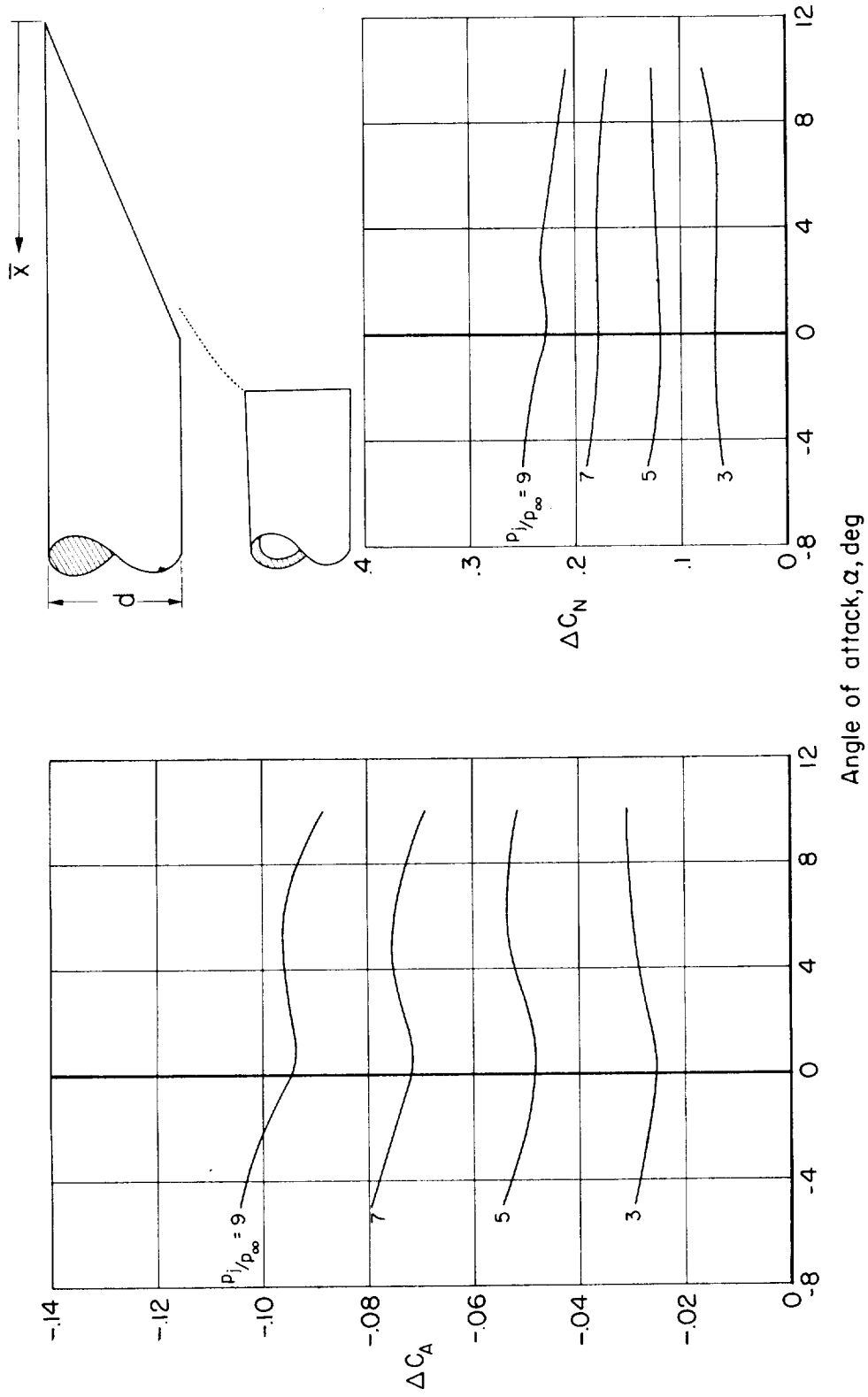
(a) Body B, $r'_d = .5$, $x'_d = 2.0$

Figure 10.- Effect of angle of attack on interference forces.



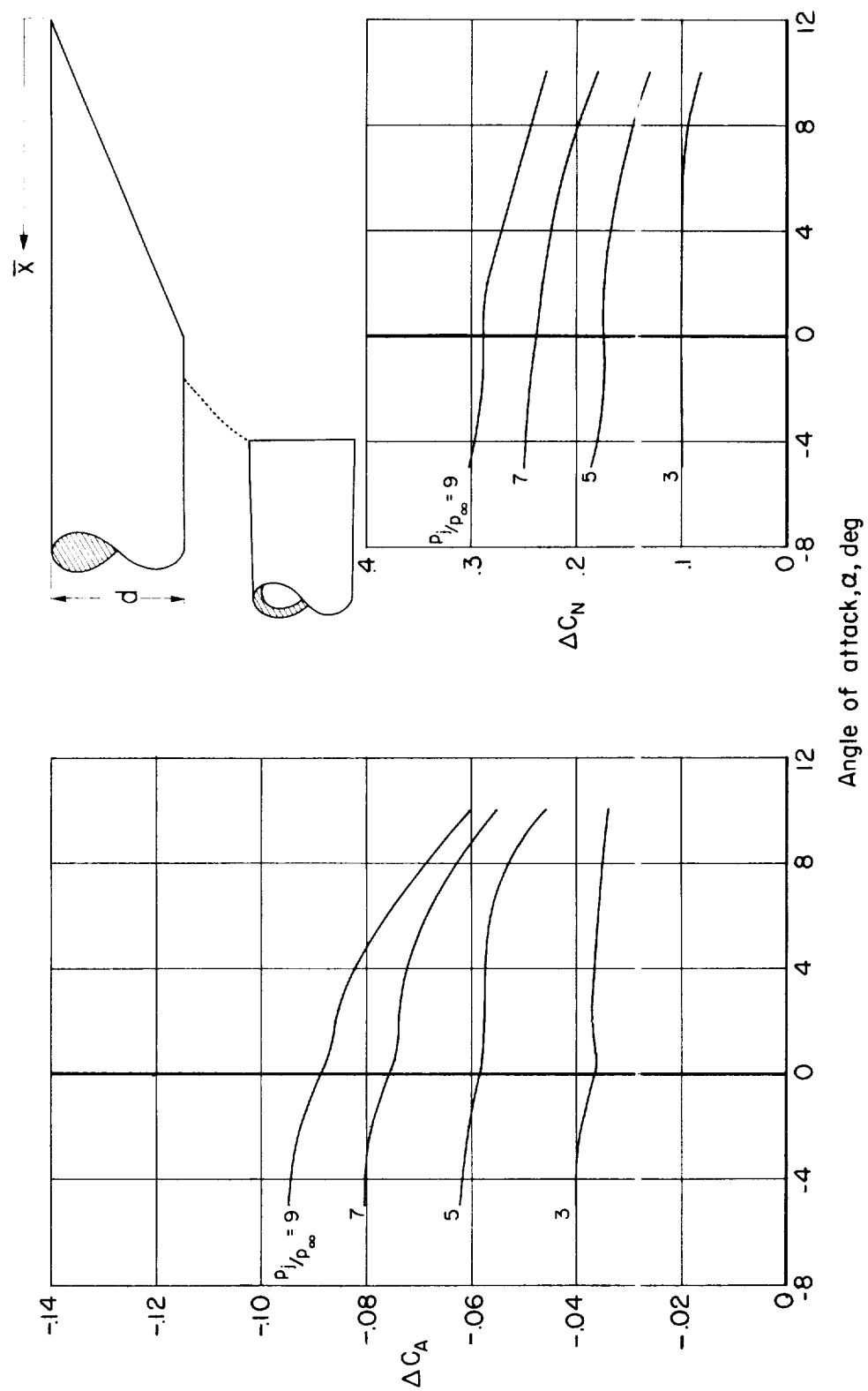
(b) Body B, $r_d = .5$, $x_d = 2.4$

Figure 10.- Continued.



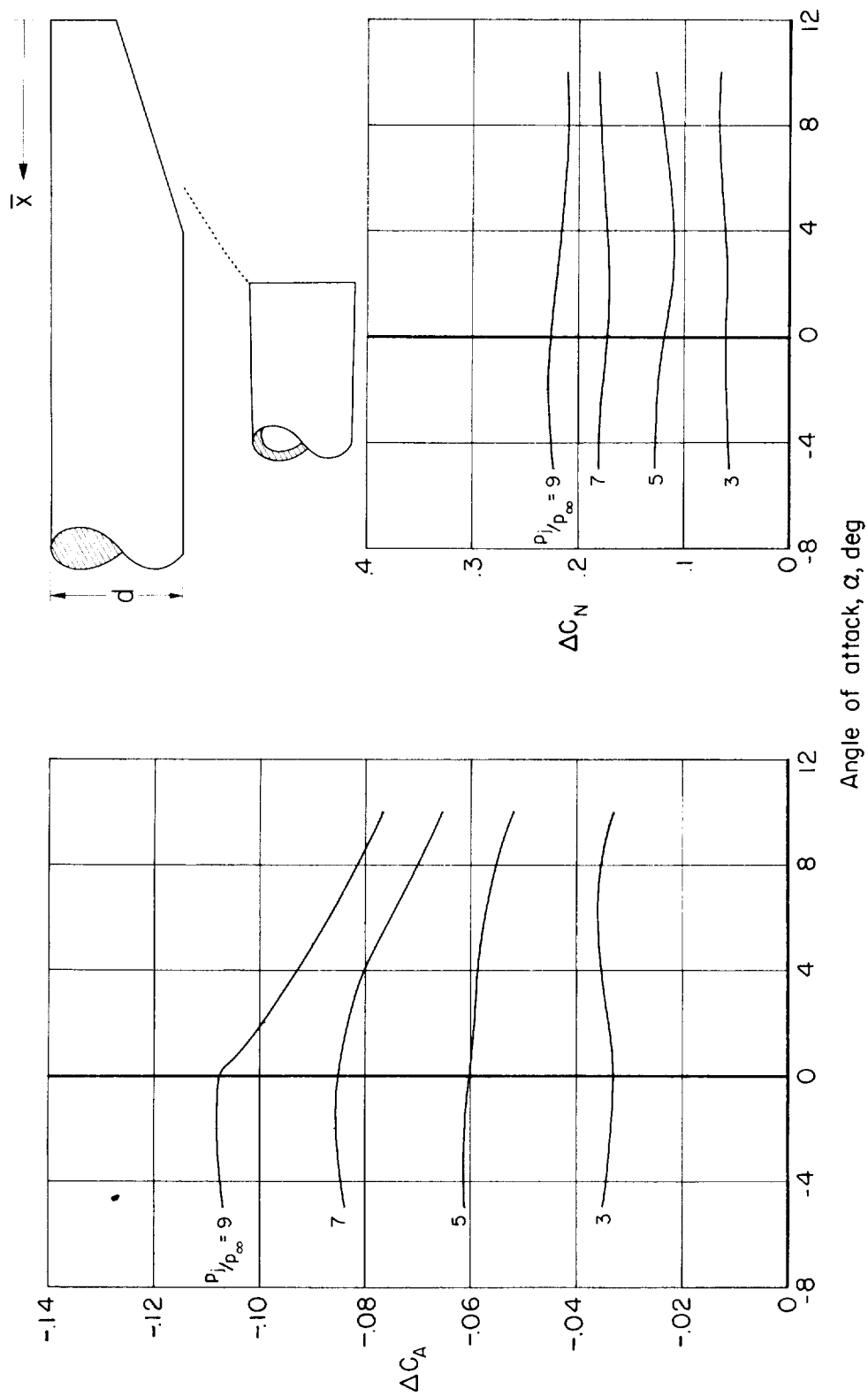
(c) Body B, $\gamma_d = .5$, $x_d = 2.8$

Figure 10.- Continued.



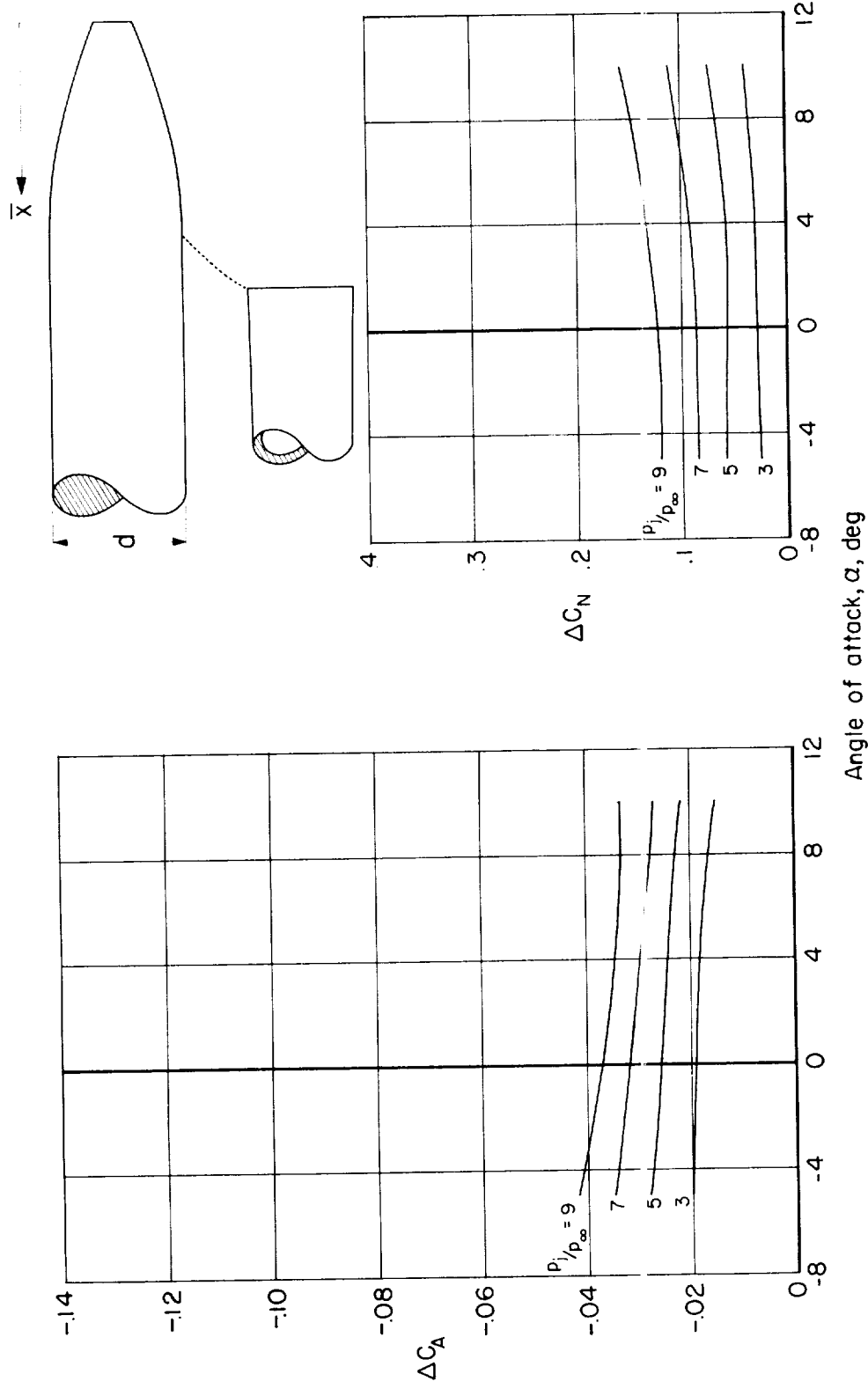
(d) Body B, $r_d = .5$, $x_d = 3.2$

Figure 10.- Continued.



(e) Body E, $l_d = .5$, $x_d = 2.0$

Figure 10.- Continued.



(f) Body $H/d = 0.5$, $x/d = 2.0$

Figure 10.- Concluded.

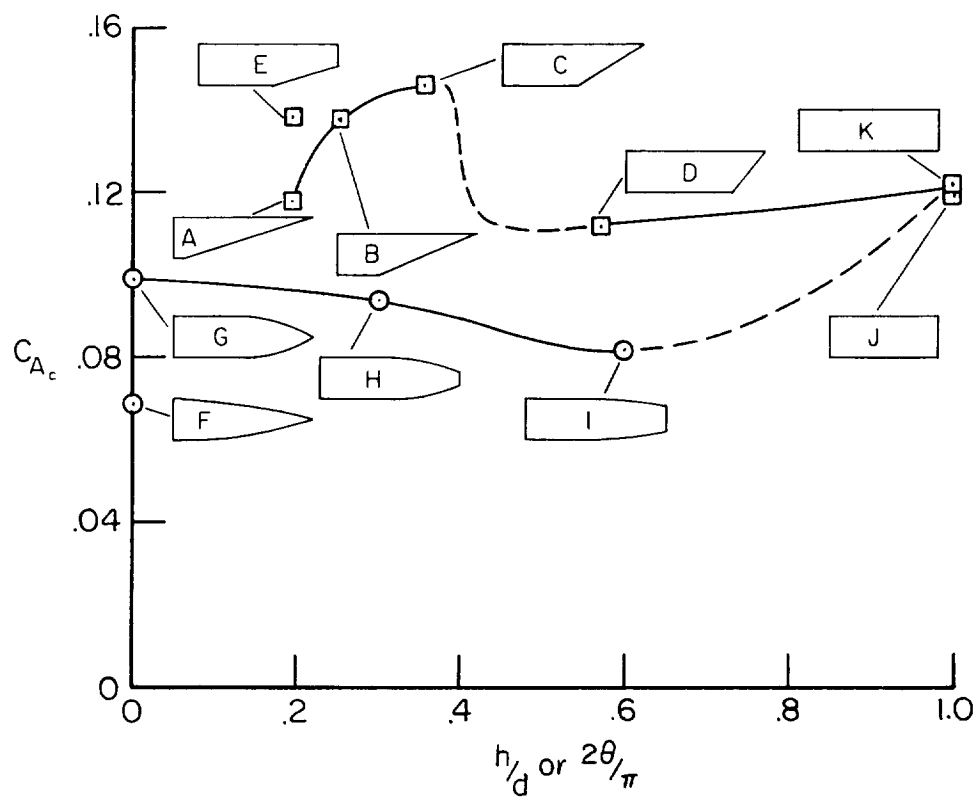
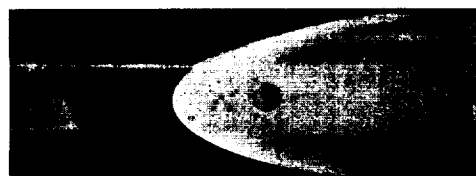


Figure 11.- Axial force on afterbodies with nacelle removed.



Afterbody E

(Same as forehalf of afterbody A)



Afterbody B



Afterbody C



Afterbody D

Figure 12.- Pictures of sublimation patterns that indicate location of vortices.

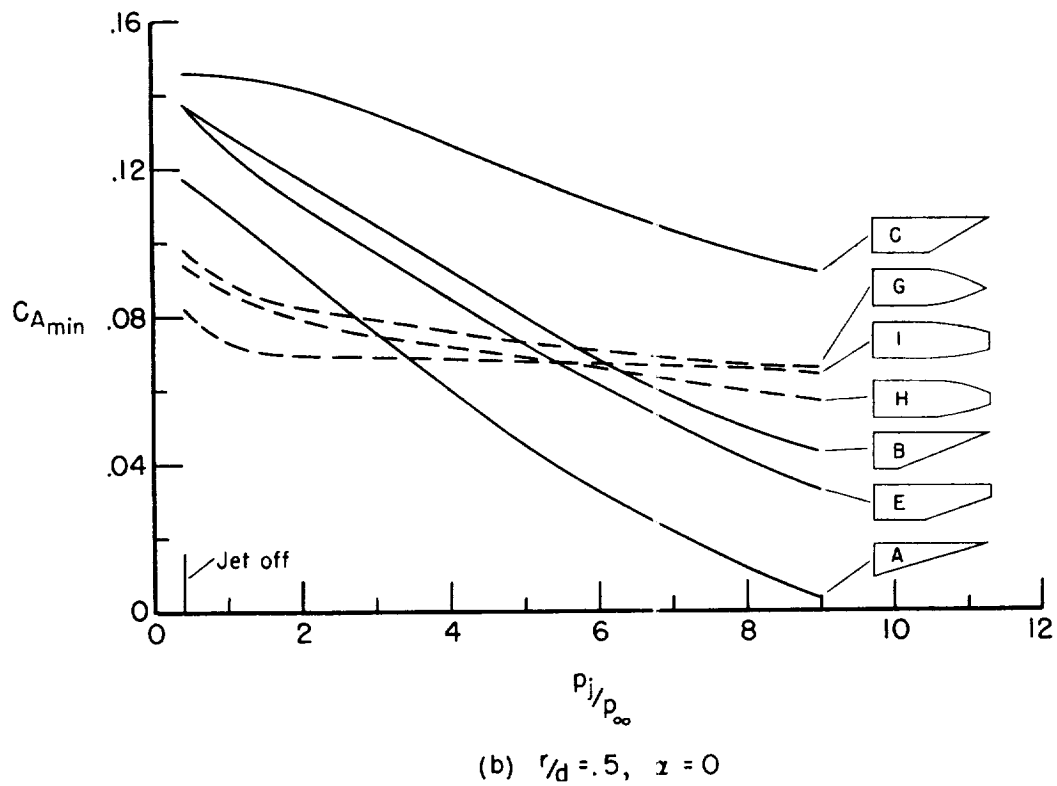
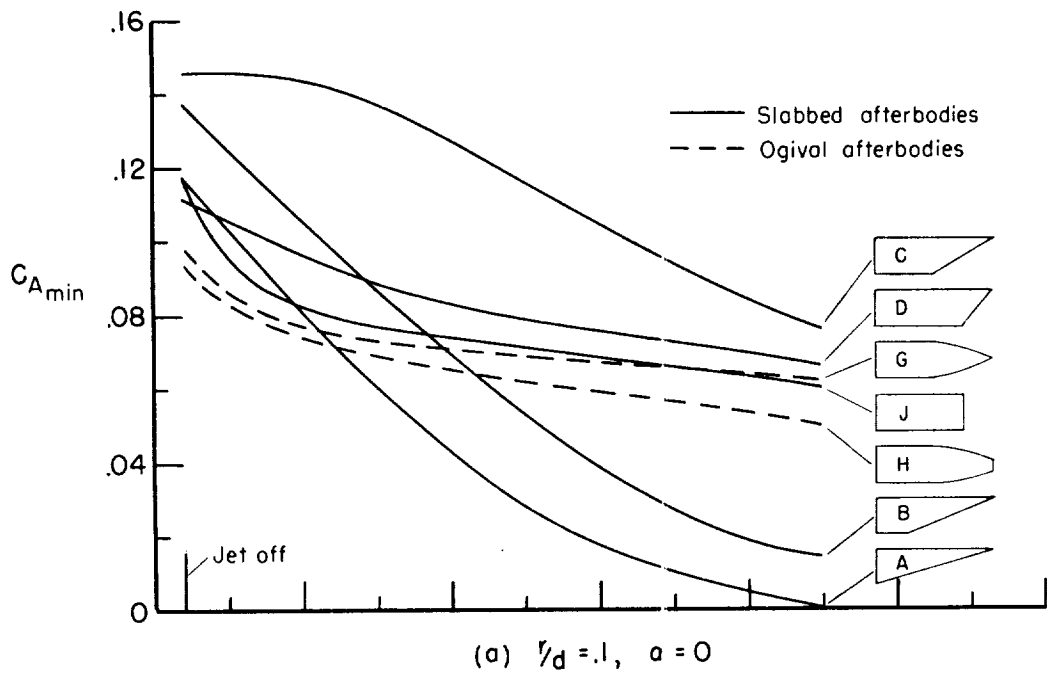
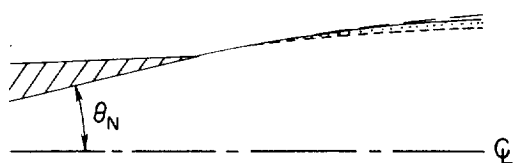
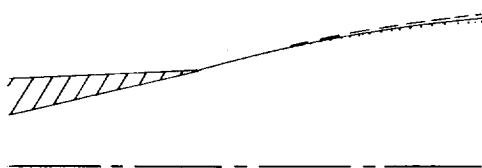


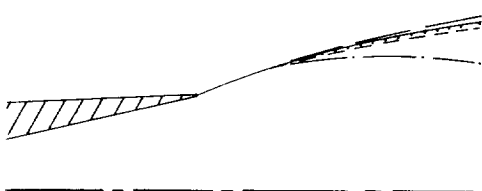
Figure 13.- Effect of afterbody shape on C_{Amin} .



| | M_∞ | M_j | θ_N | γ_j | P_j/P_∞ |
|----------------------|------------|-------|------------|------------|----------------|
| (Theory) <u> </u> | 0 | 2.5 | 10 | 1.4 | 1.33 |
| (Theory) <u> </u> | 0 | 3.0 | 10 | 1.2 | 1.35 |
| (Theory) <u> </u> | 0 | 3.0 | 5 | 1.4 | 1.90 |
| (Expt) <u> </u> | 2.94 | 2.7 | 11.6 | 1.4 | 3.0 |



| | M_∞ | M_j | θ_N | γ_j | P_j/P_∞ |
|----------------------|------------|-------|------------|------------|----------------|
| (Theory) <u> </u> | 0 | 2.5 | 10 | 1.4 | 1.77 |
| (Theory) <u> </u> | 0 | 3.0 | 10 | 1.4 | 1.96 |
| (Expt) <u> </u> | 2.94 | 2.7 | 11.6 | 1.4 | 5.0 |



| | M_∞ | M_j | θ_N | γ_j | P_j/P_∞ |
|----------------------|------------|-------|------------|------------|----------------|
| (Theory) <u> </u> | 0 | 2.5 | 10 | 1.4 | 2.48 |
| (Theory) <u> </u> | 0 | 3.0 | 10 | 1.4 | 2.91 |
| (Theory) <u> </u> | 0 | 3.0 | 10 | 1.2 | 2.42 |
| (Theory) <u> </u> | 0 | 2.5 | 20 | 1.4 | 1.15 |
| (Expt) <u> </u> | 2.94 | 2.7 | 11.6 | 1.4 | 9.0 |

Figure 14.- Comparison with experiment of the jet-boundary shapes estimated from charts of reference 6; $\alpha = 0$.

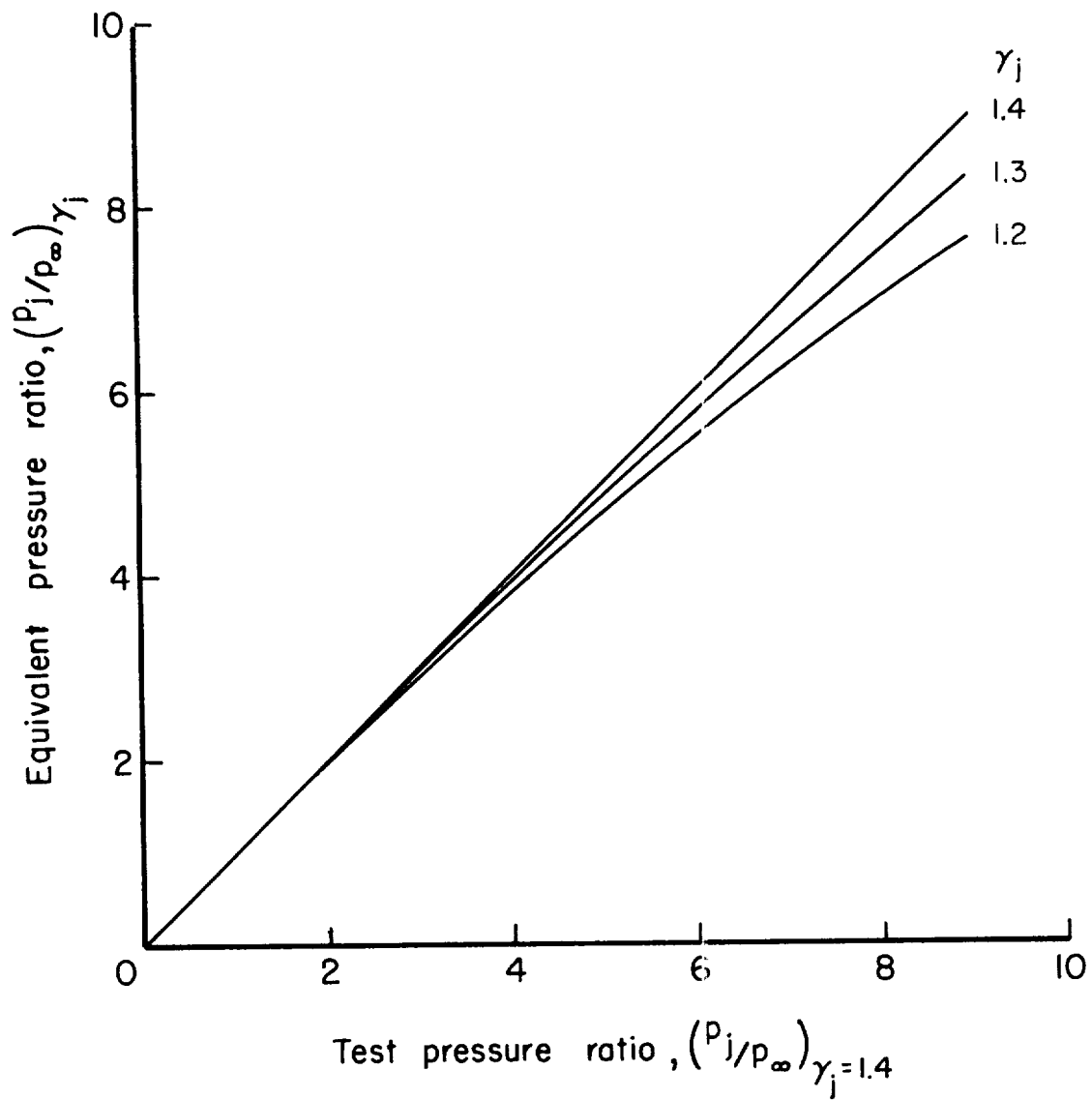


Figure 15.- Equivalent pressure ratios for air jet and hot-gas jet for nozzle of this investigation.

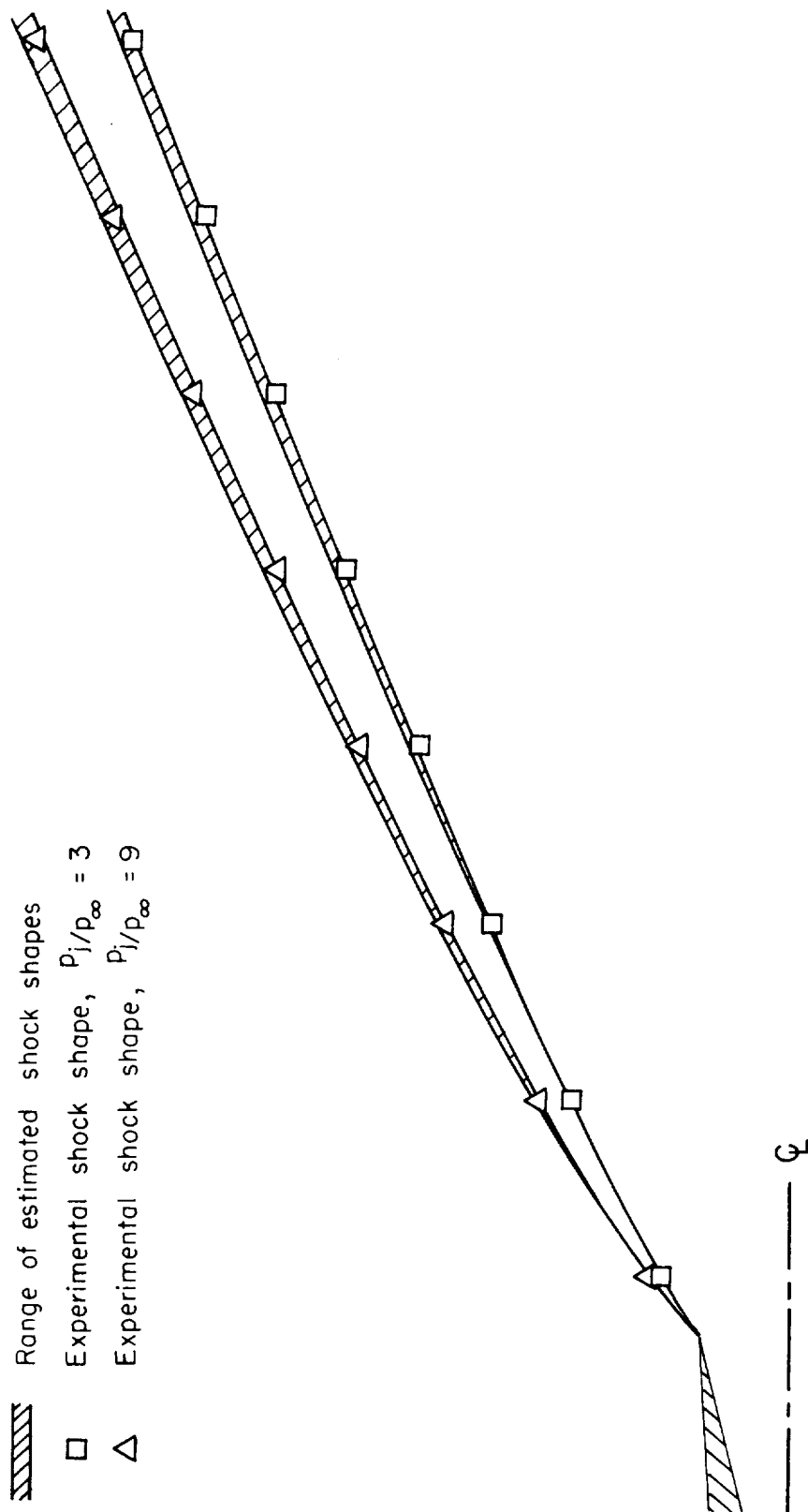


Figure 16.- Comparison with experiment of the exit shock wave shape estimated by the method of reference 9 for the jet-boundary shapes of figure 14, $\alpha = 0$.

| | |
|--|---|
| <p>NASA TN D-332 National Aeronautics and Space Administration. AXIAL-FORCE REDUCTION BY INTERFERENCE BETWEEN JET AND NEIGHBORING AFTERBODY. William C. Pitts and Lyle E. Wiggins. September 1960. 95p. OTS price, \$2.25. (NASA TECHNICAL NOTE D-332)</p> <p>Experimental results are presented for an exploratory investigation of the effectiveness of interference between jet and afterbody in reducing the axial force on an afterbody with a neighboring jet. Interference effects on normal force and center of pressure are also presented. The test Mach number was 2.94, the jet Mach number 2.71, and the Reynolds number 0.25×10^6 based on body diameter. The variables include static-pressure ratio of the jet (up to 9), nacelle position relative to the afterbody, angle of attack (-50 to 100), and afterbody shape. The interference axial forces are large and favorable. For several configurations the total afterbody axial force is reduced to zero by the interference.</p> <p>Copies obtainable from NASA, Washington (over)</p> | <p>I. Pitts, William C. II. Wiggins, Lyle E. III. NASA TN D-332</p> |
| <p>NASA TN D-332 National Aeronautics and Space Administration. AXIAL-FORCE REDUCTION BY INTERFERENCE BETWEEN JET AND NEIGHBORING AFTERBODY. William C. Pitts and Lyle E. Wiggins. September 1960. 95p. OTS price, \$2.25. (NASA TECHNICAL NOTE D-332)</p> <p>Experimental results are presented for an exploratory investigation of the effectiveness of interference between jet and afterbody in reducing the axial force on an afterbody with a neighboring jet. Interference effects on normal force and center of pressure are also presented. The test Mach number was 2.94, the jet Mach number 2.71, and the Reynolds number 0.25×10^6 based on body diameter. The variables include static-pressure ratio of the jet (up to 9), nacelle position relative to the afterbody, angle of attack (-50 to 100), and afterbody shape. The interference axial forces are large and favorable. For several configurations the total afterbody axial force is reduced to zero by the interference.</p> <p>Copies obtainable from NASA, Washington (over)</p> | <p>I. Pitts, William C. II. Wiggins, Lyle E. III. NASA TN D-332</p> |

| | | | |
|---|-------------|---|-------------|
| <p>NASA TN D-332 (Initial NASA distribution: 2, Aerodynamics, missiles and space vehicles.)</p> | <p>NASA</p> | <p>NASA TN D-332 (Initial NASA distribution: 2, Aerodynamics, missiles and space vehicles.)</p> | <p>NASA</p> |
| <p>NASA TN D-332 (Initial NASA distribution: 2, Aerodynamics, missiles and space vehicles.)</p> | <p>NASA</p> | <p>NASA TN D-332 (Initial NASA distribution: 2, Aerodynamics, missiles and space vehicles.)</p> | <p>NASA</p> |